Modelle und Simulationen granularer Materialien

(Models and Simulations of Granular Materials)

Inauguraldissertation
zur Erlangung des Doktorgrades
der Fakultät für Physik
der
Albert-Ludwigs-Universität Freiburg i. Br.

vorgelegt von
Stefan Luding
aus Selbitz
1994

present address: Dr. Stefan Luding (Assoc. Prof.)
Particle Technology
DelftChemTech,
TNW, TUDelft
Julianalaan 136
2628 BL Delft
The Netherlands

Tel.:   +31 15 278 3874
Fax: +31 15 278 4945

e-mail: lui@ica1.uni-stuttgart.de
                s.luding@tnw.tudelft.nl
WWW: http://www.ica1.uni-stuttgart.de/~lui
                http://www.dct.tudelft.nl/part/welcomePTG.html

MODELS AND SIMULATIONS OF GRANULAR MATERIALS

Stefan Luding, Theoretische Polymerphysik, Rheinstraße 12,
D-79104 Freiburg, Germany
e-mail: lui@tpoly1.physik.uni-freiburg.de

Abstract

We study models for granular materials using both event driven (ED) and molecular dynamics (MD) methods. In the MD simulations we implement linear as well as nonlinear interaction laws. For multiparticle interactions we detect that MD calculations lead to an anomalous energy loss. We elucidate this effect and the conditions under which it occurs.

As a toy-model for dissipative granular materials, we investigate a one-dimensional column of beads undergoing external vibrations and display the cross-over from a condensed to a fluidized state of the column. We find clustered states at high dissipation and for a large number of beads. Recent experimental data support the appearance of a fluidized regime at low dissipation and of a Feigenbaum-type bifurcation scenario at high dissipation.

Furthermore, we present a series of simulations on systems of smooth beads enclosed in 2D boxes. We focus on the fluidized regime, where the height of the center of mass of the system scales relative to the restitution coefficient ε, the number of beads N, and the typical velocity of the bottom plate. The comparison of MD and ED results leads to impressive agreement, whereas the functional dependence differs from the results in 1D-systems.

Using a MD algorithm we display the limitations of this numerical method. We show that previously reported convection patterns obtained through MD may be due to microscopic interactions. MD calculations often involve parameters which lead to large contact times between beads and to large density fluctuations. In turn, they enhance the occurrence of convection rolls, a numerical finding without experimental counterpart.

Contents

4

Symbols used in the text

D dimension of the system

g gravitational acceleration

N number of particles in the system

A_0 amplitude of the sinusoidal motion of the bottom plate

f frequency of the sinusoidal motion of the bottom plate

T period of the sinusoidal motion of the bottom plate: $T = 1/f$

ω angular frequency of the sinusoidal motion of the bottom plate: $\omega = 2\pi f$

α dimensionless acceleration of the bottom plate: $\alpha = A_0\omega^2/g$

ε restitution coefficient for the collision of two particles

ε_p restitution coefficient for the collision of one particle with the bottom plate

x positive penetration depth of two particles during collision

X effective dissipation parameter

m_{red} effective mass for the collision of two particles: $m_{\text{red}} = m_1 m_2/(m_1+m_2)$

K spring-constant of the elastic restoration

D_n dissipative constant in normal direction

D_t dissipative constant in tangential direction

β exponent of non-linearity of the elastic restoration force

γ exponent of non-linearity of the viscous dissipative force

ω_0 angular frequency for a linear interaction law: $\omega_0 = (K/m_{\text{red}})^{1/2}$

μ dissipative constant for bead-bead ($\mu = D_n$) or bead-wall interaction ($\mu = D_n/2$)

$\tilde{\omega}$ angular frequency of damped linear interaction: $\tilde{\omega} = (\omega_0^2 - \mu^2)^{1/2}$

t_{MD} molecular dynamics time-step

t_c contact time

E elasticity constant

η viscosity constant

λ dimensionless dilatation

τ_D dissipation time (typical time-scale, in which the average energy is dissipated)

h_{cm} height of the center of mass

h_{cm0} height of the center of mass at rest

r_{ij} distance vector from the center of particle i to the center of particle j, $r_{ij} = r_j - r_i$

v_{ij} relative velocity, $v_{ij} = \dot{r}_{ij}$

n_{ij} normal vector of contact, $n_{ij} = r_{ij} / |r_{ij}|$

t_{ij} tangential vector of contact, $t_{ij} = (-n_{ij}^y, n_{ij}^x)$

$\mathcal{E}$ total energy

E_{kin} kinetic energy

E_{rel} relative energy

l mean free path

t_{ev} average time between events

L width of the container

n_b number of beads per layer in a 2D system at rest

n_h number of layers of a 2D system at rest

1. Introduction and Background

In nature we find numerous examples of non-cohesive granular materials like sand and pebbles. In the industrial world powder processing is also of crucial interest. In recent years much effort has been invested to understand the behavior of granular media. Summaries on the present situation can be found, for example in [1-3].

Non-cohesive granular materials are characterized as assemblies of solid, nonuniform particles, which interact via contact forces and are kept together by gravity. If the contact between the particles is broken, their interaction ceases. Such systems, situated halfway between solids and liquids, exhibit surprising properties; these properties reveal that the granulates are being an intriguingly specific class of materials. The basic physics of these materials is still not well understood [2,3]. Some of the fascinating features are displayed in effects such as size-segregation [4-9], heap formation under vibration [10-13], and bulk dilatation [14,15]. Those properties which resemble a fluid include convection rolls [16-18], surface fluidization [19,20], and surface waves [18,20,21]. In granular media, we find surprising sound wave propagation properties [22,23], as well as density wave formation [24,25] or the so-called 'decompaction' [26] in dissipative granulates.

The a priori assessment of macroscopic parameters from the consideration of local contact and dissipative interactions represents a difficult problem because of the high level of disorder involved. Evidently, it is extremely difficult to probe into the dynamics of granulated particles on scales comparable to their dimensions. Nonetheless great advances have been made monitoring model systems on short scales [13,19]; model systems which, for example consist of rather large spheres instead of extremely asymmetric grains. Above all, such systems are by far more accessible than powders or sand, and they provide a means for investigating the basic features in the complex behavior of real granulates. The measurement of fundamental quantities such as the local densities and the energy transfer between grains also requires more attention.

Numerical simulations [27-36] are tools to study complex dynamics, tools which adequately complement the experimental findings [13,19,36-38], and the more analytical approaches [39-43], and thus it is crucial to develop reliable computer algorithms that

correctly reproduce the macroscopic phenomenology. Simulating granular media realistically for dimensions $D>1$ is an arduous task. Among the many methods used we address time-driven Monte-Carlo [34,44] and molecular dynamics (MD) simulations [45-48] as well as event-driven (ED) algorithms [30-33,36,49]. We also mention cellular automata methods [24,44] and random walk approaches [44,47].

At the moment the majority of simulations use molecular dynamic techniques [35] which involve ad hoc microscopic assumptions like linear spring/dashpot interaction laws [28,45,48], nonlinear interaction laws [52-57], hysteretic interactions [58-60], static as well as dynamic friction [53,55-57] and also nonspherical geometries [51]. We first mention the work by Cundall and Strack [28] who follow the motion of the particles via a molecular dynamics scheme. Moreau and Jean [29,61] solve the problem numerically, by using a time-discretization procedure to assess the systems' dynamics via a set of non-smooth equations.

Other procedures are event-driven, like the one described recently by Lubachevsky, who presented an algorithm to create a random packing of billiard balls [30], and the method of Bernu and Mazighi, who calculated the behavior of a horizontal array of beads colliding with a wall [31]. McNamara and Young investigated the same model [32] and discussed the "cooling" of one-dimensional granular media [33]. ED simulations, based on binary collisions, are hampered by the fact that at a certain threshold of energy loss, the frequency of collisions between the beads is bound to diverge and clusters will form. Thus a description has to be elaborated for the occurrence of connected clusters [36,62].

Different simulation methods (i.e. MD as well as ED methods) were used to investigate simple assemblies of interacting beads. The forces used in the MD simulations can be related to the momentum restitution coefficient; the last quantity is of utmost importance in calculations that focus on collisions of hard spheres (ED). A simple 1D toy model shows that the appearance of anomalous behavior in MD simulations depends on large fluctuations in the distances between beads, in their energy loss, and in the dilatancy threshold, i.e. the connection to collective motion. This behavior is due to the MD model forces acting on the beads and may subsist even at the limit of very 'hard' interactions. It was called the "detachment effect" [63] because under certain conditions the particles separate completely. This effect is different from the so-called decompaction evidenced in 2D dissipative granular systems [26]. Decompaction is due to the friction with the walls and not due to the elastic properties of the material. It is important to notice that in spite of the wealth of recently obtained computer results on complex systems, bench-mark experiments with straightforward simulation algorithms are still rare. Recent publications [58,59,63] discuss the specific contact laws which govern the dynamic constitutive behavior. Non-linear hysteretic interaction laws have been proposed [58,59] and the computational studies are compared with experiments of quasistatic arrangements. It seems that linear as well as

non-linear interaction laws together with velocity dependent damping are not a reasonable model for dry granular media [59]; therefore, we compare the MD method with an ED procedure and discuss their differences. In MD simulations the contact time of two particles is a parameter of preeminent importance, whereas in ED simulations the contact time is implicitly zero. The effects stemming from the contact time in MD calculations may vanish when we use ED simulations.

One may focus on the problem of fluidization [36,62,64], as opposed to problems characterizing convection [45,48,65]. Convection is connected to a flow of mass, whereas for fluidization the flow, averaged over time, may vanish. We note that the behavior of the fluidified state is complex, especially when large fluctuations and large density gradients occur. Fluidization may be readily observed by putting sand on a loudspeaker or on a vibrating table [10,11,16,19,66]. A vibrating medium conveys energy to the sand which is then dissipated through collisions among the grains. The density of the material is, even under strongly dissipative conditions, reduced, so that the system can behave like a fluid in many ways. Thus, under certain circumstances convection cells may appear or heaps may form spontaneously [10,11,16]. When, for example, particles of different sizes are put on the vibrating plate the larger ones tend to rise; this leads to a spatial segregation of the particles according to the size of the particles and the geometry of the system [3]. However, there are still open questions on the reasons for this effect; convection [67] as well as steric effects [9,44] may cause segregation.

A convenient way to achieve the separation of convection and fluidization is to take a basically one-dimensional model, i.e. a column consisting of N beads [36]. One-dimensional models mediate between the one-bead problem in 1D [68-70] and situations involving many beads in dimensions larger than one [13,22,28-30,34,46,64,71]. The one-bead problem was studied extensively both from the experimental [69] as well as from the analytical and simulational [68-70] points of view and many physical effects such as period doubling can be found. Another way of studying fluidization involves using a 2-dimensional model without shear forces and rotational motion [64], since these effects seem important for the occurrence of convection and heaping.

A one-dimensional [36,62] and a two-dimensional model system [64] both with more than one particle show the fluidization of vibrated granular materials, yet different kinds of dimension-dependent behavior are found. The aim of such simple models is to have both a transparent theoretical situation [49], as well as an experimentally viable arrangement [62]. Consequently we present 1D and 2D situations which we analyse using ED and MD simulations, the aim being to find the circumstances under which the results obtained through the two methods agree. As we proceed to show, we find that the mean height of the center of mass of the system, i.e. the potential energy, scales with respect to the

restitution coefficient, to the number of beads and to the velocity of the bottom plate.

Recently, experimental evidence of spontaneous convection rolls was reported on 3D granular materials [12,18] as well as on 2D model media [13]. Based on MD simulations two independent groups of authors [45,48] presented spontaneous convection in vibrating granular materials; their calculations were related to effects found experimentally in hard-sphere systems. MD simulations often use parameters which lead to contact times larger than experimentally obtained and thus to large density fluctuations. The question arises as to what extent MD methods accurately reproduce hard-sphere collisions, especially in situations in which the systems consist of many particles. For a specific example, i.e. a simple linear "spring-dashpot" microscopic interaction, the magnitude of the observed convection depends drastically on the parameters of the MD simulation [64]. Convection almost disappears when the contact time approaches its physical value. We interpret this effect in terms of the anomalous energy dissipation and the large density fluctuations, called "detachment effect" [63].

In Sec.2 we discuss the basic physical conservation laws and introduce the numerical procedures used in this study. Using simple toy-models, the connection between both methods is discussed in Sec.3. We devote Sec.4 to the investigation of a 1D vibrated model system. In Sec.5 we concentrate on 2D systems where fluidization as well as convection appears. Finally, we summarize and discuss our findings in Sec.6.

2. Simulation Aspects

In this section the primary physical equations are discussed. Furthermore, different simulation methods, i.e. event-driven (ED) and molecular dynamics (MD), are introduced. Since problems with the computing time may occur in ED simulations if the collision frequency is large we elaborate a method to account for the appearance of clusters [36,62].

2.1. Physical framework

A classical textbook in the field of the collisions of particles is Goldsmiths' *IMPACT* [74]. Goldsmith follows the ideas of 'stereomechanics' to describe the collision of two particles in terms of momentum and energy and to determine the final state of the system. The linear and angular momentum laws for one particle are expressed by the vector equations for the changes

$$\Delta p = \Delta m v = m v - m v_0 = \int_0^{t_c} F_{cm} dt \tag{1a}$$

$$\Delta I \omega = I \omega - I \omega_0 = \int_0^{t_c} r \times F \, dt \quad . \tag{1b}$$

m is the mass and I is the moment of inertia about the axis of rotation of the body. v and ω are the linear and the angular velocities; r is the moment arm, F is a force, F_{cm} is the component acting on the center of mass, and t is time. To satisfy Eq.(1a) let us assume a time-dependent force, $F_{cm}(t)$, acting on the particle during contact. The force changes the momentum by Δp. Thus, one arrives at the condition for a constant Δp: the shorter the contact time t_c, the larger F_{cm}. Since the experimentally observed times of contact are usually small one may neglect, in first order, small static loads such as weights.

We give the momentum conservation law as a vector

$$\sum_i m_i v_i \equiv \sum_i p_i = m_{\text{tot}} v_{\text{cm}} = \text{const.} \,,\tag{2}$$

where the sum goes over the i rigid bodies of the system. m_{tot} is the total mass and $v_{\text{cm}} = (1/m_{\text{tot}}) \sum_i m_i v_i$ is the velocity of the center of mass (cm). The conservation of linear momentum, Eq.(2), requires the forces acting during the collisions of objects to not affect the motion of the center of mass of the system. Hence, the collisions of particles only lead to a momentum exchange among the components of the system, but due to dissipative effects, i.e. solid friction or plastic deformation, energy may be lost.

The elementary units of which granular materials are composed are mesoscopic grains, whose surface is rough on the microscopic scale. Solid friction is the immediate consequence: When two touching grains are at rest with respect to each other a finite force F_s is needed to trigger relative motion (*static friction*), while when the grains move against each other a finite force F_d is needed to maintain the motion (*dynamic friction*). As a rule F_d is less than F_s; furthermore, both F_d and F_s depend only on the normal force and are independent of the relative velocity and of the area of contact (*Coulomb law*). The crucial consequence of solid friction is that on the level of the elementary units, namely of the grains, the system does *not* conserve energy. A further source of energy dissipation is the plastic deformation of the grains due to the normal forces during collisions.

In order to account for the energy loss during collisions, it is convenient to introduce the so-called restitution coefficient ε, where $\varepsilon = 1$, and $\varepsilon = 0$ correspond to perfect elasticity and to complete plasticity respectively. In general the restitution coefficient is material and velocity dependent. To describe the frictional properties of the contact surfaces one may introduce the dynamic coefficient of friction ϕ. $\phi = 0$ and $\phi = \infty$ describe the change in the tangential relative velocity of bodies with perfectly smooth and completely rough surfaces respectively. In this study we assume mostly small ϕ-values and thus neglect the rotation of the particles.

We now turn to a discussion of the central collision of two spherical bodies with masses m_1 and m_2. The momenta $P^{(i)}$ just before and $P^{(f)}$ just after the collision in the center of mass reference frame are given by:

$$P^{(i)} = m_1(v_1 - v_{\text{cm}}) = -m_2(v_2 - v_{\text{cm}}) = m_{\text{red}}(v_1 - v_2)\tag{3a}$$

$$P^{(f)} = m_1(u_1 - v_{\text{cm}}) = -m_2(u_2 - v_{\text{cm}}) = m_{\text{red}}(u_1 - u_2) \;;\tag{3b}$$

$m_{\text{red}} = m_1 m_2/(m_1 + m_2)$ is the reduced mass and v and u are the velocities just before and

just after the collision. Using Eqs.(3a) and (3b) together with the definition of the momentum restitution coefficient

$$\varepsilon = -P^{(f)}/P^{(i)} = -(u_1 - u_2)/(v_1 - v_2) \tag{4}$$

we find the velocity of particle j after the collision

$$u_j = v_{cm}(1 + \varepsilon) - \varepsilon v_j \quad . \tag{5}$$

The change in kinetic energy ΔE_{kin} for the central collision of two particles, expressed in terms of the restitution coefficient and of the initial relative velocity $v_1 - v_2$ can be calculated as:

$$\Delta E_{kin} = E_{kin}^{(f)} - E_{kin}^{(i)} \tag{6}$$

$$= \frac{1}{2} \sum_{j=1}^{2} m_j \left[\left(u_j \right)^2 - \left(v_j \right)^2 \right]$$

$$= -\frac{1}{2} m_{red} \left(1 - \varepsilon^2 \right) \left(v_1 - v_2 \right)^2 .$$

Obviously ΔE_{kin} vanishes for $\varepsilon = 1$ (the elastic case).

One usually has to follow Eqs.(2) and (6) for the simulation of granular media. A convenient way to do this is to neglect the time particles are in contact. Following Eq.(5) this leads to a macroscopic, ED procedure. Another possible way is to introduce contact forces and thus to integrate Eq.(1a). This technique is commonly applied in molecular dynamics simulations of different physical systems.

2.2. An event-driven procedure in 1D

For the sake of simplicity we first discuss the ED procedure in the one-dimensional case. In Fig.1 we give an example for the one-dimensional model system. The bottom plate is driven by a sinusoidal motion with amplitude A_0 and frequency f (angular frequency $\omega = 2\pi f$); hence its position at time t is:

$$z_0(t) = A_0 \sin(\omega t) \quad . \tag{7}$$

$z_3(t)$

$z_2(t)$

$z_1(t)$

$z_0(t) = A_0 \sin(\omega t)$

Fig.1

Model system with a vibrating bottom plate; here three beads are shown.

An important dimensionless parameter is α, the maximal acceleration of the bottom plate divided by the acceleration of gravity g:

$$\alpha = \frac{A_0 \omega^2}{g} \quad . \tag{8}$$

In the ED simulation one monitors a sequence of events. Between events Newton's equation of motion for each object is solved analytically. An object is an individual bead, the vibrating bottom plate, or a cluster of beads such as a collection of beads in physical contact and moving with the same velocity. An event is defined for an object either by a sudden change in momentum, i.e. a collision, or by the taking off from the bottom plate when the upward acceleration is greater than the gravity denoted by g. In 1D, the N beads are numbered from the bottom starting with $i = 1$; for the bottom plate we set $i = 0$. Each object i follows its own trajectory between events because we assume dissipation to occur only upon collision. Due to the one-dimensional nature of the model, the order of the beads never changes and we can even dispense with accounting for the diameter d of the beads. This fact permits the simplification of the notation in the 1D-simulations; we use diameter-independent coordinates $z_i(t)$ connected to the diameter dependent coordinates $h_i(t)$ through

$$z_i(t) = h_i(t) - (i-1)d - d/2 \quad . \tag{9}$$

With Δt denoting the elapsed time since the time t_0, the position of particle i at time $t_0 + \Delta t$ is:

$$z_i(\Delta t) = z_{i,0} + v_{i,0}\Delta t - \tfrac{1}{2}g(\Delta t)^2 \quad , \tag{10}$$

where $z_{i,0}$ and $v_{i,0}$ are the coordinates and velocities of particle i at time t_0.

We now compute the time after the next event happens between object i and i-1. Events occur whenever $z_i(\Delta t)=z_{i-1}(\Delta t)$ and lead to a time step:

$$\Delta t_i = -\frac{z_{i,0} - z_{i-1,0}}{v_{i,0} - v_{i-1,0}}, \text{ for } i > 1 . \tag{11}$$

The problem with the calculation of Δt_1, i.e. finding the root of $z_1(\Delta t)=z_0(\Delta t)$, is solved using a numerical root finding procedure that is based on both Newton's rule and Brent's method [75].

Formally the event times Δt_i are stored in an event-time array **T**. If $\Delta t_i < 0$ the objects move away from each other. If $\Delta t_i = 0$ the particles are in contact, a case which will be discussed later in this subsection. The positive Δt_i are now of interest the smallest of which $\Delta t_{\min}$ determines the occurrence of the next event. Once the next event is identified we compute the positions and velocities of all objects at this time $t_0+\Delta t_{\min}$, carry out the transformation corresponding to the event, and update the event-time array; then we look for the following event.

The simulations take care of the energy loss in collisions through the restitution coefficients ε and ε_p, for particle-particle- and particle-bottom plate collisions respectively; furthermore, this is the only way we account for energy losses in ED simulations. In the reference frame of the center of mass of a colliding pair with equal mass, the incoming velocities are $+V$ and $-V$ and the outgoing velocities are $-\varepsilon V$ and $+\varepsilon V$. Using a matrix formalism [31-33, 36], we find:

$$\begin{pmatrix} u_{i-1} \\ u_i \end{pmatrix} = C_{i-1,i} \begin{pmatrix} v_{i-1} \\ v_i \end{pmatrix} = \begin{pmatrix} \frac{1-\varepsilon}{2} & \frac{1+\varepsilon}{2} \\ \frac{1+\varepsilon}{2} & \frac{1-\varepsilon}{2} \end{pmatrix} \begin{pmatrix} v_{i-1} \\ v_i \end{pmatrix} \quad (i = 2,...,N) , \tag{12}$$

where v_i and u_i are the velocities of bead i just before and after the collision in the system's frame of reference. Calculating u_i leads to Eq.(5) directly with $i = 2$. A similar form also holds for collisions with the moving bottom plate which is assumed to have infinite mass. Bead 1 in the reference frame of the plate has a velocity V just before the collision and the velocity $-\varepsilon_p V$ after the collision. In the collision matrix scheme [31] it follows that

$$\begin{pmatrix} u_0 \\ u_1 \end{pmatrix} = C_{0,1} \begin{pmatrix} v_0 \\ v_1 \end{pmatrix} = \begin{pmatrix} 1 & 0 \\ 1+\varepsilon_p & -\varepsilon_p \end{pmatrix} \begin{pmatrix} v_0 \\ v_1 \end{pmatrix} \tag{13}$$

in the system's frame of reference.

We proceed by noting that in some regions of the parameter space, i. e. for high dissipation, which corresponds to low ε, or at times when the acceleration of the bottom plate is small, the time intervals between the events may become very short. If a series of such small time intervals occurs, the computing time, which is proportional to the number of events, may become very large. In the following we show how to deal with this problem. We focus on simulations for this with low restitution coefficients. We start with a column of $N = 10$ beads. As initial conditions we take an equidistant separation between beads of here 1 mm and a random distribution of velocities of -1 ms^{-1} $< v_i < 1$ ms^{-1}. For the restitution coefficients we let $\varepsilon = 0.6$ and $\varepsilon_p = 1$, which is typical for aluminum beads and a bottom plate made of glass. The trajectories of the beads are recorded as a function of time as well as the times $\Delta t^{(m,m-1)}$ between events. The events are numbered sequentially: $m = 1,2,3,...$. This situation is depicted in Fig.2. In the upper part of the picture we plot the actual positions of the beads. The diameter of the beads is as noted before disregarded; the dotted
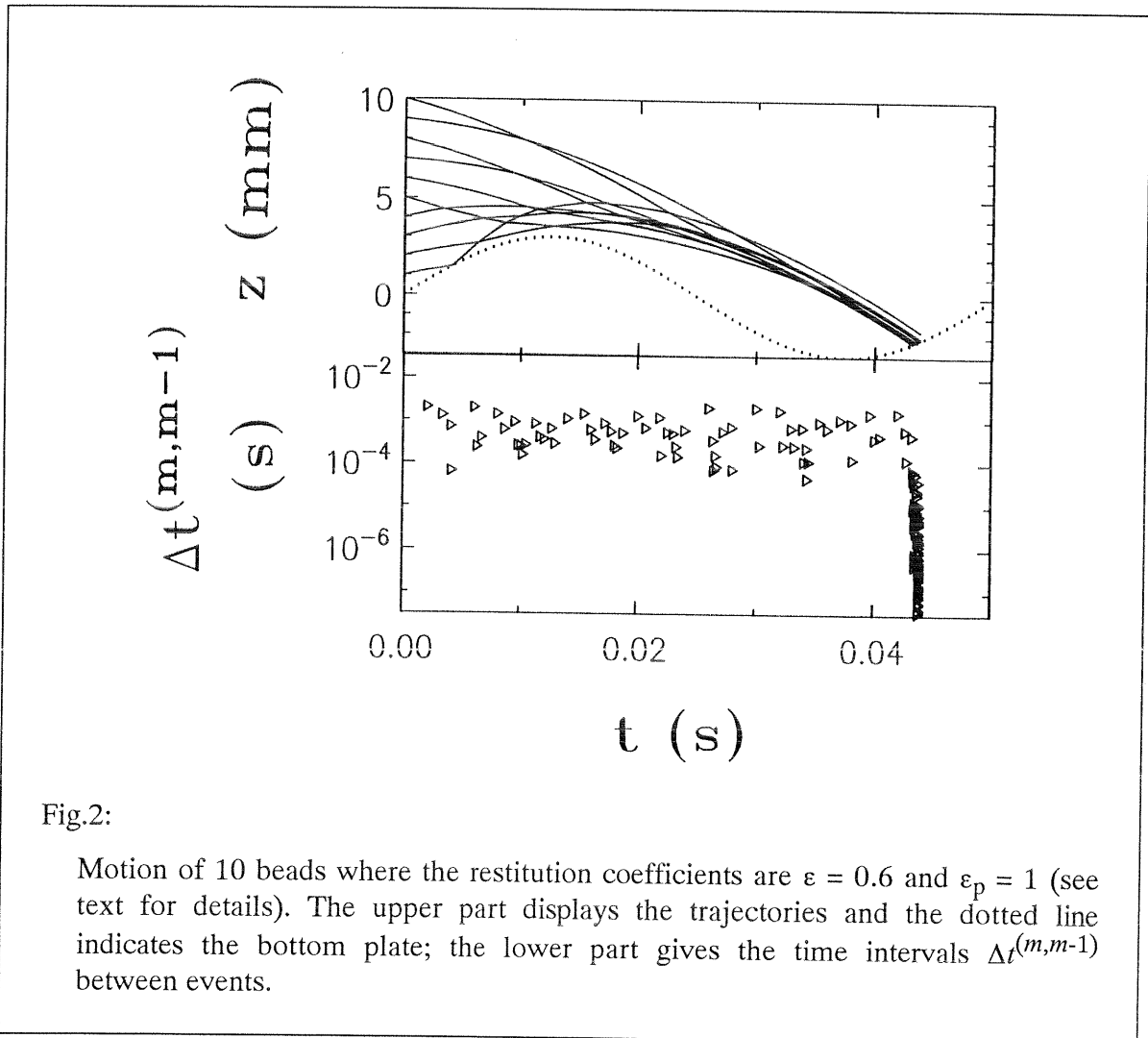

Fig.2:

Motion of 10 beads where the restitution coefficients are $\varepsilon = 0.6$ and $\varepsilon_p = 1$ (see text for details). The upper part displays the trajectories and the dotted line indicates the bottom plate; the lower part gives the time intervals $\Delta t^{(m,m-1)}$ between events.

line represents the position of the bottom plate. Since the order of particles does not change, the trajectory of one particle does not cross the trajectory of another, but the slopes, i.e. the velocities, change abruptly at the time of a collision. The time intervals $\Delta t^{(m,m-1)}$ between events are given on a logarithmic scale in the lower part of the picture and are represented by triangles. One should notice that a sudden decrease in the time intervals between events is apparent in Fig.2 for $t \cong 0.044$ s. Moreover, at this moment both the distances between the beads involved in the events, $\Delta z_i = z_i\text{-}z_{i-1}$, as well as their relative velocities, $\Delta v_i = v_{i-1}\text{-}v_i$, become very small with $\Delta v_i > 0$ before and $\Delta v_i < 0$ after a collision. The event-driven algorithm obviously runs into a situation which is computationally very time-consuming. Furthermore, it is of little physical interest to follow the procedure on such short time and length scales, because when the times between events become very small, our macroscopic description of the dissipation via ε and ε_p becomes questionable.

A means of avoiding such problems is to introduce a cut-off-velocity v_c. The idea is to merge objects which after the event have a relative velocity $|\Delta u_i| < v_c$ into a cluster, while at the same time one conserves the momentum of the center of mass. The description therefore leads from independent objects before the event to a new object, a cluster, in which the objects have zero relative distance between them and of course have the same velocity after the event. We are justified in proceeding in this way by the results of Refs.[31-33], in which it was found that in the case of high dissipation clusterization occurs; this implies that there is a complete loss of relative momentum.

We choose v_c to be orders of magnitude smaller than the typical velocity $A_0\omega$ of the system with typical values of $A_0 = 10^{-3}$ m and $f = 20$ s^{-1}, which lead to $A_0\omega = 0.125$ ms^{-1}; we usually take v_c around 10^{-7} ms^{-1} so that $v_c \ll A_0\omega$. By varying v_c we ascertained that the specific choice of v_c does not change the results of the simulation, as long as v_c and $A_0\omega$ differ by orders of magnitude.

The shift in our point of view, consisting of replacing individual beads by clusters, must be now supplemented by a procedure which determines how collisions of such clusters with the bottom plate, with another individual bead, or with another cluster have to be dealt with. For beads in contact or almost in contact with each other a collision with an external bead leads to a cascade of events involving other inner beads. The basic idea is to take a relative velocity scheme and assume that the next event in the cascade is the one for which the relative velocity $\Delta v_i = v_{i-1}\text{-}v_i$ is maximal. This procedure is based on the fact that, as described above, we run into problems when using time differences to establish the order in which the collisions happen. The algorithm that follow express this idea is described in Appendix A.

2.3. Event driven procedures for D>1

In this subsection we introduce an event-driven simulation method for dimensions larger than one. For $D>1$ we are interested in systems where the times between events are rather large; therefore, we do not discuss cluster-dynamics here.

In ED simulations the components of the system under analysis, the beads, evolve independently unless an event takes place. An event is understood as a collision between two particles or the collision of one particle with a wall: both situations are characterized by a sudden change in particles' momentum.

In the previous subsection a simple ED algorithm was described which updates the whole system after each event. Because of the small number of particles involved, the procedure works quite well in 1D. The situation changes in higher dimensions, since one then has to account for larger numbers of particles. A way to deal with the matter was put forth in Ref.[30]. The ED algorithm implemented there does not update the state of the system after each event. This requires a double-buffering data-structure where the 'old' status, i.e. time, position, velocity, and partner, as well as the 'new' status, i.e. new time, position, velocity, and partner, of each particle is recorded. If an event happens the 'new' status becomes the 'old' one and the subsequent 'new' status has to be computed. This computation is performed only for the particles involved in the collision, because only their velocities changed. In the computation of the 'new' status, the first step is to find the presumable, new colliding partner and to calculate the 'new' event time; the second step is to compute the positions and velocities after this 'new' event. A 'new' status might be preempted several times due to collisions of the partners with other components in the system. To make the algorithm more efficient it is possible to apply the so called 'delayed update' method; this means postponing examination and update of the position and the velocity of a particle until its next event; one can also store the event-times in an ordered heap-tree which simplifies finding the next event. For a detailed description of the algorithm see Ref.[30].

We implemented this algorithm with a few changes. First, we included for our purposes the forces of gravity and the vibrating bottom plate since the calculations in Ref.[30] were used to compute close-packed arrangements of spheres in the absence of external force fields. Furthermore, we implemented the dissipation through the restitution coefficient for collisions as we discuss in the following. We also found it expedient to work with fixed sphere diameters and dispensed with the idea of dividing the container into several sectors.

18

In our ED simulations, all events which consist of collisions between two particles occur at times which can be calculated analytically. The same holds true for collisions of the particles with the lateral walls, whereas the event times for particle collisions with the moving bottom plate have to be computed numerically. We use a root-finding procedure as in our 1D ED simulations [36,62] for this calculation.

We assume dissipation to occur only due to collisions in the following; furthermore, the dissipation in our ED simulations is only assumed to be be due to the normal component of the relative velocity. This is the limiting case of perfectly smooth particles. The restitution coefficient ε thus determines the normal relative velocity after collision in the reference frame of the center of mass: $u_{ij}^{(n)} = -\varepsilon v_{ij}^{(n)}$. v_{ij} and u_{ij} denote the relative velocities before and after the collision and the normal component is $v_{ij}^{(n)} = n_{ij}v_{ij}$ with $v_{ij} = v_i - v_j$, and n_{ij} is the normal direction of contact. For the restitution coefficient ε_w for collisions of particle i with a wall one has in similar fashion: $u_i^{(n)} = -\varepsilon_w v_i^{(n)}$.

2.4. The molecular dynamics method

Contrary to the ED simulations, where one defines the momentum restitution coefficient and then applies Eq.(5), we introduce elastic and dissipative forces and then solve Eq.(1a). Note that the force acting on the selected particle in Eq.(1a), in general depends on all other particles in the system and leads to a coupled integral-equation system. In the so-called molecular dynamics calculations we use a fifth order predictor-corrector algorithm [35] for integration (see Appendix B).

In the MD simulations we follow the dynamics of a system of N spherical particles with diameters d_i ($i = 1, ..., N$). d_i equals d for simulations with equal radii, or d_i is chosen randomly from a homogeneous distribution of width w around d. In the 1D-simulations the particles are placed on a vertical line Thus only the lowest particle interacts with the bottom plate. In the 2D-simulations the particles are put into a container of width L and infinite height. One may use either periodic boundary conditions or horizontally fixed walls. The bottom plate in 1D or the container in 2D may carry out a sinusoidal motion according to Eq.(7). Two particles (a particle and a wall) interact when their relative distance r_{ij}, is smaller than the sum of their radii (the radius of the particle). $r_{ij} = |r_{ij}|$ and r_{ij} points from the center of i to the center of j. Three forces are active in this regime, $d_i + d_j > 2r_{ij}$. First, an elastic restoration force:

$$f_{\text{el}}^{(i)} = -K\left[\tfrac{1}{2}(d_i + d_j) - r_{ij}\right]n_{ij} \ , \tag{14}$$

where $n_{ij} = r_{ij}/r_{ij}$ is the normal direction of contact and K is the spring constant. Second, a frictional force in the normal direction:

$$f_n^{(i)} = -D_n m_n\left[v_{ij} \cdot n_{ij}\right]n_{ij} \ , \tag{15}$$

where v_{ij} is the relative velocity of particles i and j, D_n is the normal dissipation parameter and the normalized mass is $m_n = 2m_{\text{red}}$. Third, a frictional force in the tangential direction:

$$f_t^{(i)} = -D_t m_n\left[v_{ij} \cdot t_{ij}\right]t_{ij} \tag{16}$$

where $t_{ij} = (-n_{ij}^y, n_{ij}^x)$ is the vector n_{ij} rotated by 90^0 and D_t is the tangential dissipation parameter. In our linear-model simulations we include the forces Eqs.(14) and (15) in 1D and Eqs.(14), (15) and (16) in 2D; however, we neglect the rotation of the particles as well as static friction.

We introduce non-linear interaction forces for a more general and accurate description of collisions. The nonlinear elastic restoration force is expressed as an extension of Eq.(14):

$$f_{\text{el}}^{(i)} = -K\left[\tfrac{1}{2}(d_i + d_j) - r_{ij}\right]^{1+\beta}n_{ij} \tag{17}$$

and the nonlinear dissipative force is expressed as an extension of Eq.(15):

$$f_n^{(i)} = -D_n m_n\left[v_{ij} \cdot n_{ij}\right]\left[\tfrac{1}{2}(d_i + d_j) - r_{ij}\right]^{\gamma}n_{ij} \tag{18}$$

where, again $d_i + d_j > 2r_{ij}$.

We find that the basic difference between the ED and the MD methods is the way contacts are modelled. In ED simulations the time in which colliding particles are in contact is ideally zero. This is quite different from MD simulations where the duration of a collision, i.e. the time the beads are in contact, does not vanish and in fact turns out to be quite significant.

3. Collisions

In this section we describe the behavior of colliding particles in the absence of gravitation. We compare the simulation methods introduced in the previous section and then discuss the conditions under which both methods lead to comparable results.

3.1. Two particle collisions

We examine the collision of two identical spheres with radius $d_i = d_j = d$ and mass $m_i = m_j = m$. The corresponding equations for a collision with a wall can be found by setting $d_j = 0$, and $m_j = \infty$. The vector of contact r_{ij} is then replaced by the normal vector to the wall r_{iw} that connects the center of bead i with the contact point.

3.1.1 Collisions with linear interaction models

We consider the collision of two particles in 1D. The situation is modelled, in the simplest case, by a linear spring and a linear dashpot (LSD), so that setting $\ddot{x} = f^{(i)}/m_i - f^{(j)}/m_j$ with $f^{(i)} = f_{el}^{(i)} + f_n^{(i)}$, according to Eqs.(14) and (15); the differential equation holds for the (positive) penetration depth $x = (1/2)\,(d_i + d_j) - r_{ij}$:

$$\ddot{x} + 2\mu\dot{x} + \omega_0^2 x = 0 \quad .$$

(19)

In Eq.(19), for the collision of two particles i and j, one has $\mu = D_n$ and $\omega_0 = \sqrt{K/m_{red}}$ with $m_{red} = m_i m_j / (m_i + m_j)$ being the reduced mass. The solution of Eq.(19) is:

$$x(t) = (v_0/\tilde{\omega})\exp(-\mu t)\sin(\tilde{\omega}t)$$

(20)

with the corresponding velocity:

$$\dot{x}(t) = (v_0/\tilde{\omega})\exp(-\mu t)\left[-\mu\sin(\tilde{\omega}t) + \tilde{\omega}\cos(\tilde{\omega}t)\right] \quad .$$

(21)

In Eqs.(20) and (21) $v_0 = \dot{x}(0)$ is the relative velocity before collision and $\tilde{\omega} = \sqrt{\omega_0^2 - \mu^2}$ a damped frequency. The contact time is given by

$$t_c = \pi / \tilde{\omega} \quad , \tag{22}$$

because the interaction ends when $x(t) < 0$. The coefficient of restitution ε is defined by $\varepsilon = -\dot{x}(t_c) / \dot{x}(0)$, see Eq.(4), so that

$$\varepsilon = \exp(-\pi\mu / \tilde{\omega}) \quad . \tag{23}$$

From Eqs.(20) and (21) the maximal penetration depth x_{max} can also be derived; it fulfills the condition $\dot{x}(t_{max}) = 0$, so that $\tilde{\omega} t_{max} = \arctan(\tilde{\omega}/\mu) = \arcsin(\tilde{\omega}/\omega_0)$ and

$$
\begin{aligned}
x_{max} &= (v_0/\tilde{\omega})\exp(-\mu t_{max})\sin(\tilde{\omega} t_{max}) \\
&= (v_0/\omega_0)\exp[(-\mu/\tilde{\omega})\arcsin(\tilde{\omega}/\omega_0)] \quad .
\end{aligned}
\tag{24}
$$

For the case of low dissipation, i.e. $\omega_0 >> \mu$, this leads to $t_{max} = t_c/2$ and to

$$x_{max} = v_0 / \omega_0 \quad . \tag{25}$$

The maximal penetration depth x_{max} in the case of, say, steel particles is much smaller than the particle diameter. In our linear model x_{max} is proportional to v_0, see Eq.(25). In the case of high velocities (which occur for small dissipation and strong agitation) one obtains for fixed ω_0, i.e. fixed K, rather large x_{max}-values; this is a problem in the linear model underlying Eq.(25). K is a function of the Young modulus and the Poisson ratio, which are inherent in the material and thus establish t_c for the linear model and for a given material.

3.1.2. Collisions with nonlinear interaction models

Linear interactions are not accurate descriptions for rigid bodies, since the surface of contact generally depends on the compression. Thus we consider, again, the collision of two particles in 1D and use a nonlinear spring and a nonlinear dashpot. Setting $\ddot{x} = f^{(i)}/m_i - f^{(j)}/m_j$ with $f^{(i)} = f_{el}^{(i)} + f_n^{(i)}$ according to the (non-linear) Eqs.(17) and (18) the differential equation holds for the (positive) penetration depth x:

$$\ddot{x} + 2\mu\dot{x}x^\gamma + \omega_0^2 x^{1+\beta} = 0 \quad . \tag{26}$$

On phenomenological grounds, i.e. to obtain constants in units of the Young modulus $[\text{kg m}^{-1}\text{s}^{-2} = \text{N m}^{-2}]$ and of the viscosity $[\text{kg m}^{-1}\text{s}^{-1} = \text{N s m}^{-2}]$ we set $K = Ed^{1-\beta}$ and $\mu = D_n = \eta d^{1-\gamma}/(2m_{red})$ and thus the following general compression-dissipation equation

results:

$$m_{\text{red}}\ddot{x} + \eta d\left(\frac{x}{d}\right)^{\gamma}\dot{x} + Ed\left(\frac{x}{d}\right)^{\beta}x = 0 \quad . \tag{27}$$

Here E and η are dependent on both material and shape; E depends on the Young modulus and the Poisson ratio, while η depends on both the compression and, in general, also on the shearing viscosities. Note that the channel of energy loss in Eq.(27) is only viscoelastic; thus neither a plastic, permanent deformation nor a loss due to residual vibrations stored in the spheres after collision are included. Furthermore, the nonlinear terms are formulated as functions of (x/d), where d is the diameter of the beads, in order to keep the structure of the equation close to that of Eq.(19). As we proceed to show several models used in the literature are special cases of Eqs.(26) and (27). The simplest form ($\beta = \gamma = 0$) connects Eq.(26) with Eq.(19). For two spheres Hertz calculated the elastic interaction parameter E due to a symmetrical deformation; in fact he found $\beta = 1/2$ [73]. Various recent studies used this interaction law [50,53,84] together with a linear loss coefficient ($\gamma = 0$). Kuwabara and Kono [83] generalized the Hertz argument to deal with viscoelastic compression dependent loss; they obtain $\gamma = 1/2$. Taguchi [81] extended the expression by including a nonlinear dependence of the dissipation on the velocity. In Appendix C we present scaling arguments which permit estimations from Eq.(27), at the limit of low dissipation, the dependence of the momentum restitution coefficient ε on the initial velocity v_0.

Eq.(C2) of Appendix C, with $\beta = 1/2$ and $\gamma = 0$ reproduces Hertz' equation. One has $E = Y/(3(1 - \tilde{\sigma}^2))$ where Y is the Young-modulus and $\tilde{\sigma}$ is the Poisson-ratio. We calculate the order of magnitude of t_c for steel beads of diameter $d = 1.5$ mm. We use $Y = 2.06 \times 10^{11}$Nm^{-2}, $\tilde{\sigma} = 0.28$ and $m = 1.38 \times 10^{-5}$kg for steel and obtain a contact time of $t_c \approx 4.6 \times 10^{-6}$s, for an initial velocity of 1ms^{-1} when dissipation is ignored; for aluminum, for which one has $Y = 0.71 \times 10^{11}$Nm^{-2}, $\tilde{\sigma} = 0.34$ and $m = 0.479 \times 10^{-5}$kg one again obtains a contact time t_c of around 4.6×10^{-6}s. This estimate is less precise because of the large dissipation of aluminum beads. We note that Hertz' expression, valid for low dissipation, shows a weak dependence of t_c on the velocity, i.e. $t_c \propto v_0^{-1/5}$.

Furthermore, we stress the fact that once a reasonable t_c value is chosen, one can model the dynamics using even simple LSD interactions. This is the idea behind a significant number of works on the problem. In the following, we shall mainly use the simple LSD interaction laws.

Choosing a pair of values appropriate to the material for ε and t_c fixes the parameters μ and ω_0 in Eq.(19) unambiguously. Thus for spheres made of steel $\varepsilon = 0.9$; for spheres with diameter $d = 1.5$ mm we use $t_c = 4.6 \times 10^{-6}$s which leads to $\omega_0 \approx 6.8 \times 10^5$s^{-1}

and to $\mu \approx 2.3 \times 10^4 \mathrm{s}^{-1}$. For aluminum $\varepsilon = 0.6$ so that using $t_c \approx 4.6 \times 10^{-6}\mathrm{s}$ one roughly has $\omega_0 \approx 6.8 \times 10^5 \mathrm{s}^{-1}$ and $\mu \approx 1.1 \times 10^5 \mathrm{s}^{-1}$. These values for ω_0 and μ are much larger than what has been commonly used in earlier simulation approaches and lead, for an initial velocity $v_0 = 1\mathrm{ms}^{-1}$, to a penetration depth of $x_{max} \approx 1.5 \times 10^{-6}\mathrm{m}$, which means 0.1 percent of the diameter. Other simulations [45,48], both with a different size and time scaling, use ω_0- and μ-values which lead to a penetration depth of a few percent of the particle's diameter for particle velocities in the order of magnitude of the maximum velocity of the vibrating box $v_0 \cong A_0\omega$. Note that taking a very low value for t_c requires involved computing power. The problem is knowing whether it is of much importance to use such low contact times. We address this question in the following.

3.2. Many particle collisions (the 'Detachment Effect')

We are now interested in probing into the collective behavior of arrays of beads in simple one-dimensional toy-models. In this subsection we neglect gravitational effects and discuss the collision of an array of beads with a static boundary or with other beads. This situation is interesting since it allows us to compare MD results with those obtained using the ED algorithms [31,32,36,49,62].

In Figs.3(a), 3(b) and 3(c) we plot the results of MD simulations for $N = 10$, $\varepsilon = 0.9$, $v_0 = -0.2\mathrm{ms}^{-1}$ and $t_c = 7 \times 10^{-6}\mathrm{s}$. The y-axis representss the reduced height, see Eq.(9). Given ε and t_c, the values μ and ω_0 are obtained using Eqs.(22) and (23); μ and ω fix via $K = m_{red}\omega_0^2$ and $D_n = \mu$, the parameters to be used for binary collisions. In Fig.3(a) we start from an initial separation between neigboring particles of $s_0 = 0$ m; in Fig.3(b) we use $s_0 = 10^{-6}\mathrm{m}$ and in Fig.3(c) we use $s_0 = 10^{-5}\mathrm{m}$. In Figs.3(d), 3(e) and 3(f) we plot the results of ED simulations with $N = 10$, $\varepsilon = 0.9$ and $v_0 = -0.2\mathrm{ms}^{-1}$; we again use $s_0 = 0$ m [Fig.3(d)], $s_0 = 10^{-6}\mathrm{m}$ [Fig.3(e)] and $s_0 = 10^{-5}\mathrm{m}$ [Fig.3(f)]. For ED simulations the contact time t_c is zero. Comparing Figs.3(a) and 3(b) with 3(d) and 3(e) respectively shows that the outcome of MD simulations differs from the one for ED in the case of very small initial separations; the final velocity of the particles' center of mass (cm) turns out to be larger in MD simulations; further on the interparticle separations after the collisions are relatively ordered for ED and quite disordered for MD simulations. Evidently this finding may be a means to check the computational methods experimentally. On the other hand, for sufficiently large initial separations [see Figs.3(c) and 3(f)] MD and ED simulations lead to qualitatively similar results. We also note that the ED procedures lead to similar results both for $s_0 > 0$ and $s_0 = 0$ whereas the situation is different for MD.
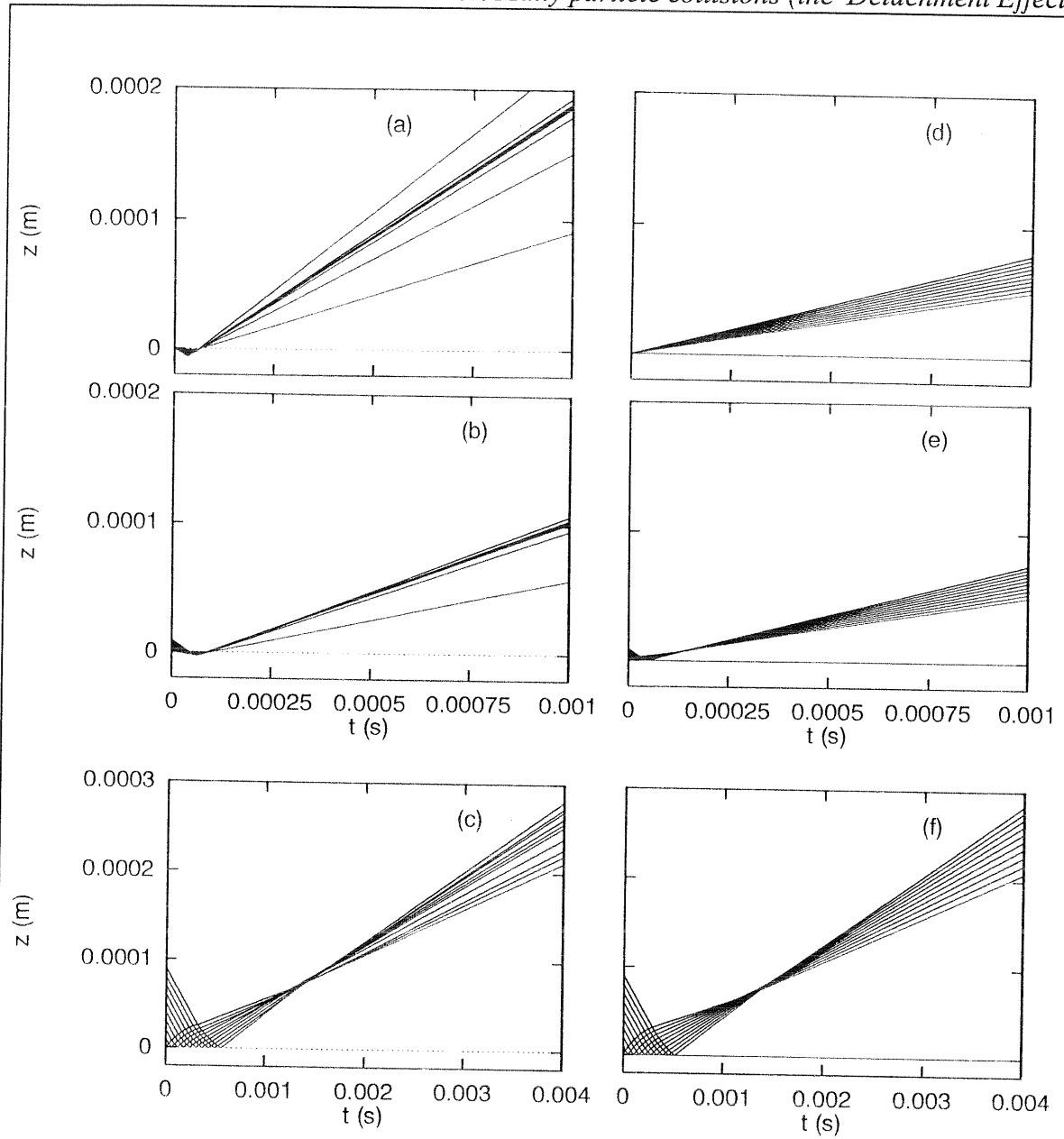
Fig.3:

(a) MD trajectories of the centers of $N = 10$ particles which collide with a fixed boundary. Here $\varepsilon = 0.9$, $t_c = 0.7\times10^{-5}$s, $v_0 = -0.2$ ms^{-1}, and $s_0 = 0$ m. The positions are in reduced units, Eq.(9).

(b) The same as in Fig.3(a) but with $s_0 = 10^{-6}$m.

(c) The same as in Fig.3(a) but with $s_0 = 10^{-5}$m. Note the different axes.

(d) ED trajectories of the centers of $N = 10$ particles; the parameters are as in Fig.3(a); especially $s_0 = 0$ m.

(e) The same as in Fig.3(d) but with $s_0 = 10^{-6}$m.

(f) The same as in Fig.3(d) but with $s_0 = 10^{-5}$m. Note the different axes.
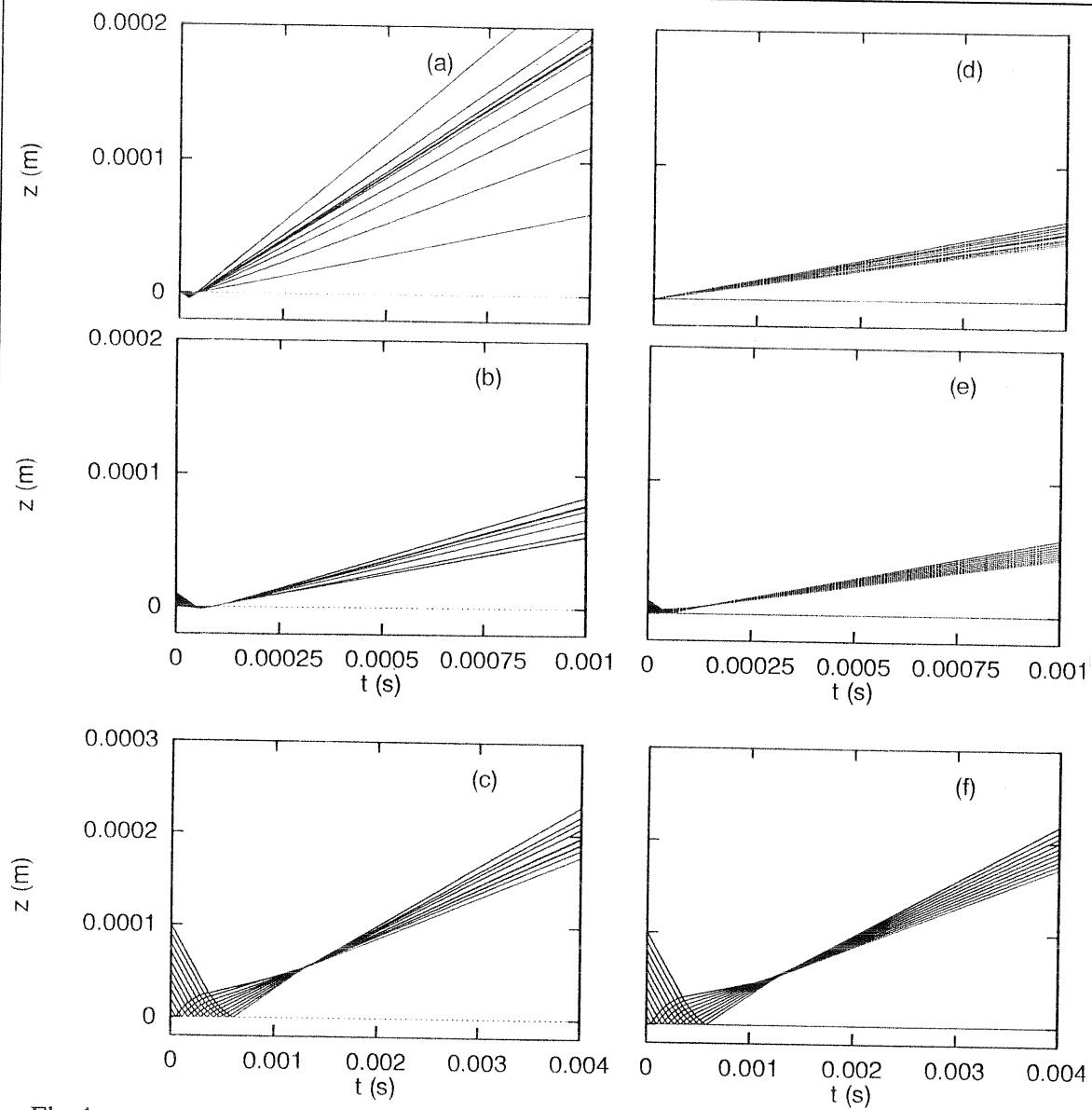
Fig.4:

(a) MD trajectories of the centers of $N = 10$ particles which collide with a fixed boundary. Here $\beta = 1/2$ and $\gamma = 0$ in Eq.(27) such that $\varepsilon = 0.86$ and $t_c = 6 \times 10^{-6}$s for one binary collision with a relative velocity of 0.2 ms^{-1}. All particles have the same initial velocity $v_0 = -0.2$ ms^{-1} and $s_0 = 0$ m. The positions are in reduced units, Eq.(9).

(b) The same as in Fig.4(a) but with $s_0 = 10^{-6}$m.

(c) The same as in Fig.4(a) but with $s_0 = 10^{-5}$m. Note the different axes.

(d) ED trajectories of the centers of $N = 10$ particles with $\varepsilon = \varepsilon(u) = 1 - 0.1 \, u^{-0.2}$ (with $u = v$, measured in units of 1 ms^{-1}); the parameters correspond to Fig.4(a); especially $s_0 = 0$ m.

(e) The same as in Fig.4(d) but with $s_0 = 10^{-6}$m.

(f) The same as in Fig.4(d) but with $s_0 = 10^{-5}$m. Note the different axes.

In Figs.4(a-f) we show the same set of simulations, but here we use a non-linear interaction law (see Figure caption for details). Comparing Figs.4(a) and 4(b) with 4(d) and 4(e) respectively we find that the outcome of MD simulations differs from the one for ED in the case of very small initial separations; the final velocity of the particles' cm, as above, turns out to be larger in MD simulations and the interparticle separations after the collisions are relatively ordered for ED and quite disordered for MD simulations. For sufficiently large initial separations [see Figs.4(c) and 4(f)] MD and ED simulations lead to qualitatively similar results.

In Figs.5 and Figs.6 we present a distinct situation where no wall is involved, i.e. we let four beads, with an initial velocity of $v_0 = -0.2$ ms^{-1} and an initial separation s_0, coming from the top collide with one other bead, with an initial velocity of $v_0 = 0.2$ ms^{-1}, coming from the bottom. As above, the labels (a), (b) and (c) correspond to MD , the labels (d), (e) and (f) correspond to ED results (see figure captions for details). In Figs.5(a-c) we use a linear interaction model, [Eq.(19)], whereas for the simulations of Figs.6(a-c) we use a non-linear interaction model [Eq.(26)]. In Figs.5(d-f) the restitution coefficient is taken to be constant whereas in Figs.6(d-f) we use a velocity dependent restitution coefficient. The parameters for MD simulations are chosen so that both, ED and MD methods lead to the same restitution coefficient for pair collisions, i.e. $\varepsilon = 0.9$ in Fig.5 and $\varepsilon = 1 - 0.1\ v_0^{-1/5}$ in Fig.6. Comparing Figs.5(a)-(c) with 5(d)-(f) respectively, and comparing Figs.6(a)-(c) with 6(d)-(f) respectively we find that the outcome of MD (a)-(c) differs from that of ED simulations (d)-(f) only in the case of very small initial separations. As above the interparticle separations after the collisions are ordered for ED and quite disordered for MD simulations. For sufficiently large initial separations [see Figs.5(c) or 6(c), and 5(f) or 6(f)] MD and ED simulations lead to qualitatively similar results independent of the interaction laws used. Comparing Figs.5(a) and 6(a), note that the reduced trajectories of the four upper particles initially coincide since here $s_0 = 0$, we find a difference between linear and non-linear interaction laws. The beads are less separated after the collision in the case of non-linear interactions, i.e. the second bead, counted from the top, is less separated from the cluster.

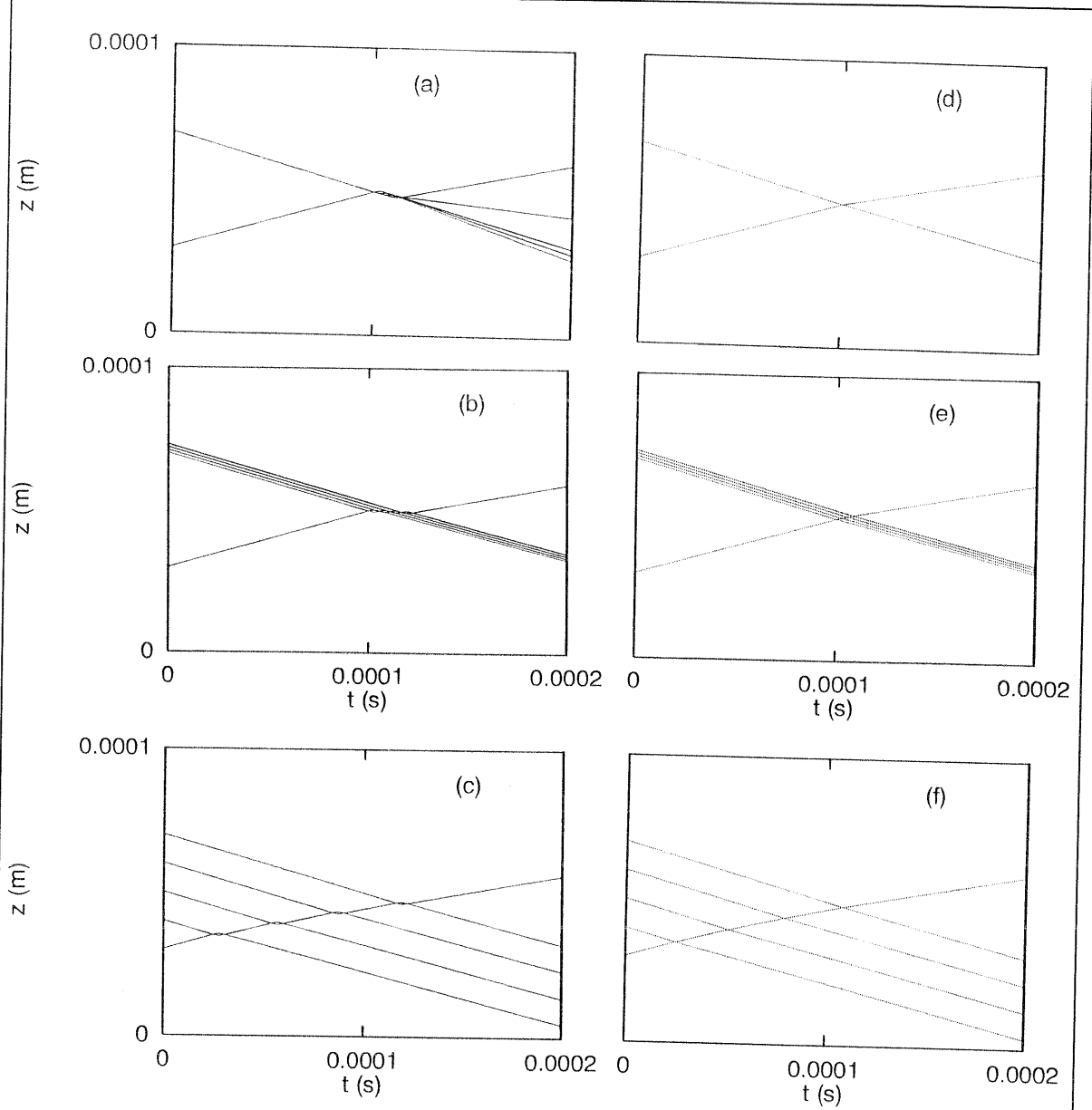## 3.2. Many particle collisions (the 'Detachment Effect')

(a)

(d)

(b)

(e)

(c)

(f)

z (m), t (s)

Fig.5:

(a) MD trajectories of the centers of $N = 5$ particles, four of which are moving downwards with $v_0 = -0.2\,\text{ms}^{-1}$, which collide with one particle, moving upwards with $v_0 = 0.2\,\text{ms}^{-1}$. Here $\varepsilon = 0.9$, $t_c = 0.7\times10^{-5}\text{s}$ and the separation of the upper four particles is $s_0 = 0$ m. The positions are in reduced units, Eq.(9).

(b) The same as in Fig.5(a) but with $s_0 = 10^{-6}\text{m}$.

(c) The same as in Fig.5(a) but with $s_0 = 10^{-5}\text{m}$.

(d) ED trajectories of the centers of $N = 5$ particles; the parameters correspond to Fig.5(a); especially $s_0 = 0$ m.

(e) The same as in Fig.5(d) but with $s_0 = 10^{-6}\text{m}$.

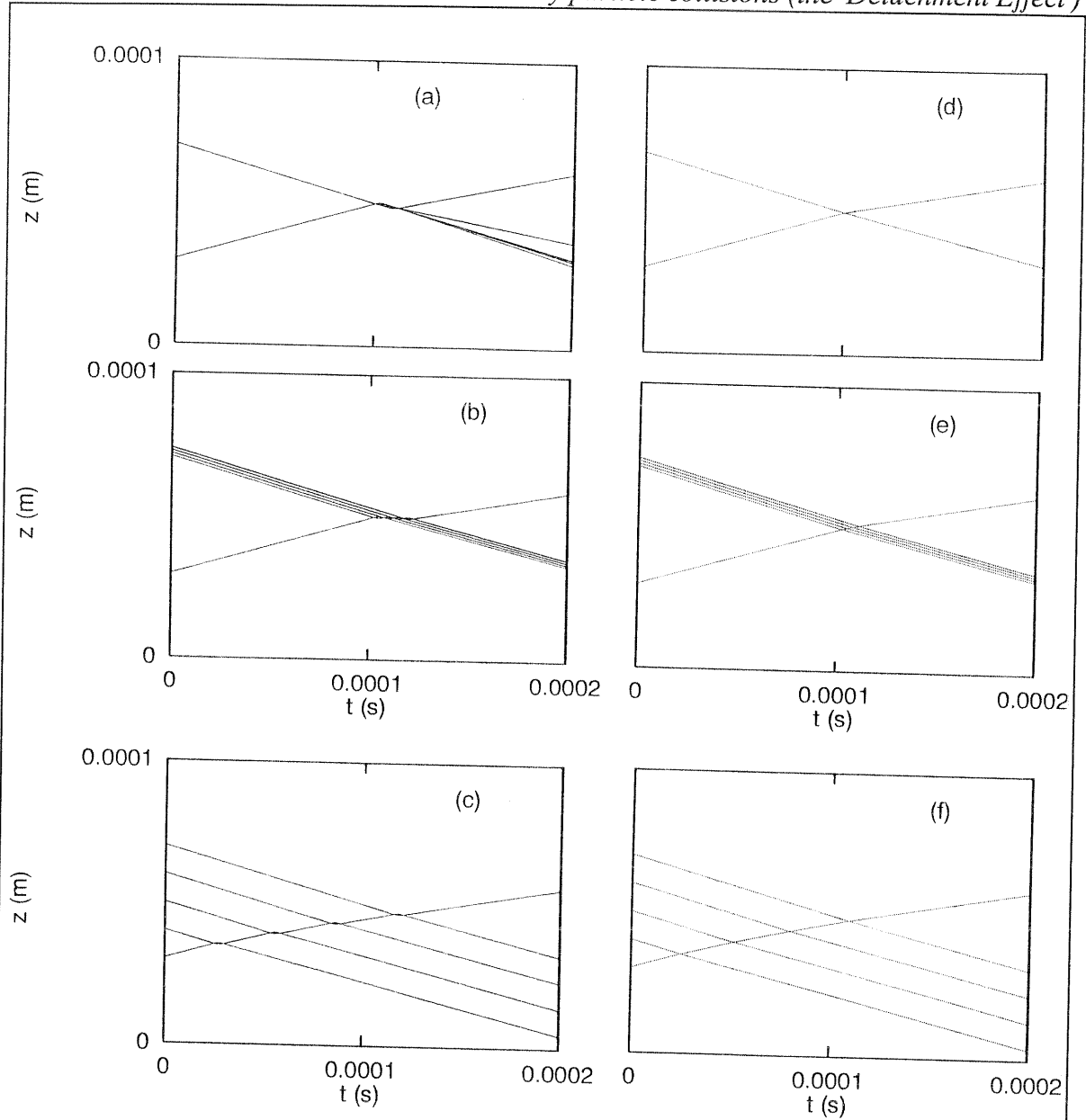(f) The same as in Fig.5(d) but with $s_0 = 10^{-5}\text{m}$.

28

Fig.6:

(a) MD trajectories of the centers of $N = 5$ particles, four moving downwards with $v_0 = -0.2\,\mathrm{ms}^{-1}$, which collide with one particle, moving upwards with $v_0 = 0.2\,\mathrm{ms}^{-1}$. Here $\beta = 1/2$ and $\gamma = 0$ in Eq.(27) such that $\varepsilon = 0.86$ and $t_c = 6\times 10^{-6}\mathrm{s}$ for one binary collision with a relative velocity of $0.2\,\mathrm{ms}^{-1}$. The separation of the upper four particles is $s_0 = 0$ m. The positions are in reduced units, Eq.(9).

(b) The same as in Fig.6(a) but with $s_0 = 10^{-6}\mathrm{m}$.

(c) The same as in Fig.6(a) but with $s_0 = 10^{-5}\mathrm{m}$.

(d) ED trajectories of the centers of $N = 5$ particles; the parameters are as in Fig.6(a); especially $s_0 = 0$ m.

(e) The same as in Fig.6(d) but with $s_0 = 10^{-6}\mathrm{m}$.

(f) The same as in Fig.6(d) but with $s_0 = 10^{-5}\mathrm{m}$.

3.2.1. The energy loss during collisions

To be more quantitative we introduce the effective restitution coefficient for many particle collisions through $\varepsilon_{\text{eff}} = \sqrt{E_f/E_0}$, where E_0 and E_f denote the initial and final energies. Furthermore, we define the *relative* kinetic energy, also called 'granular temperature' [42], through $E_{\text{rel}} = \frac{1}{2}\sum_{i=1}^{N} m_i (v_i - v_{\text{cm}})^2$; E_{rel} is also a measure of the typical separation of the beads after rebound.

In Fig.7(a) we plot ε_{eff} obtained from MD simulations [similar to those presented in

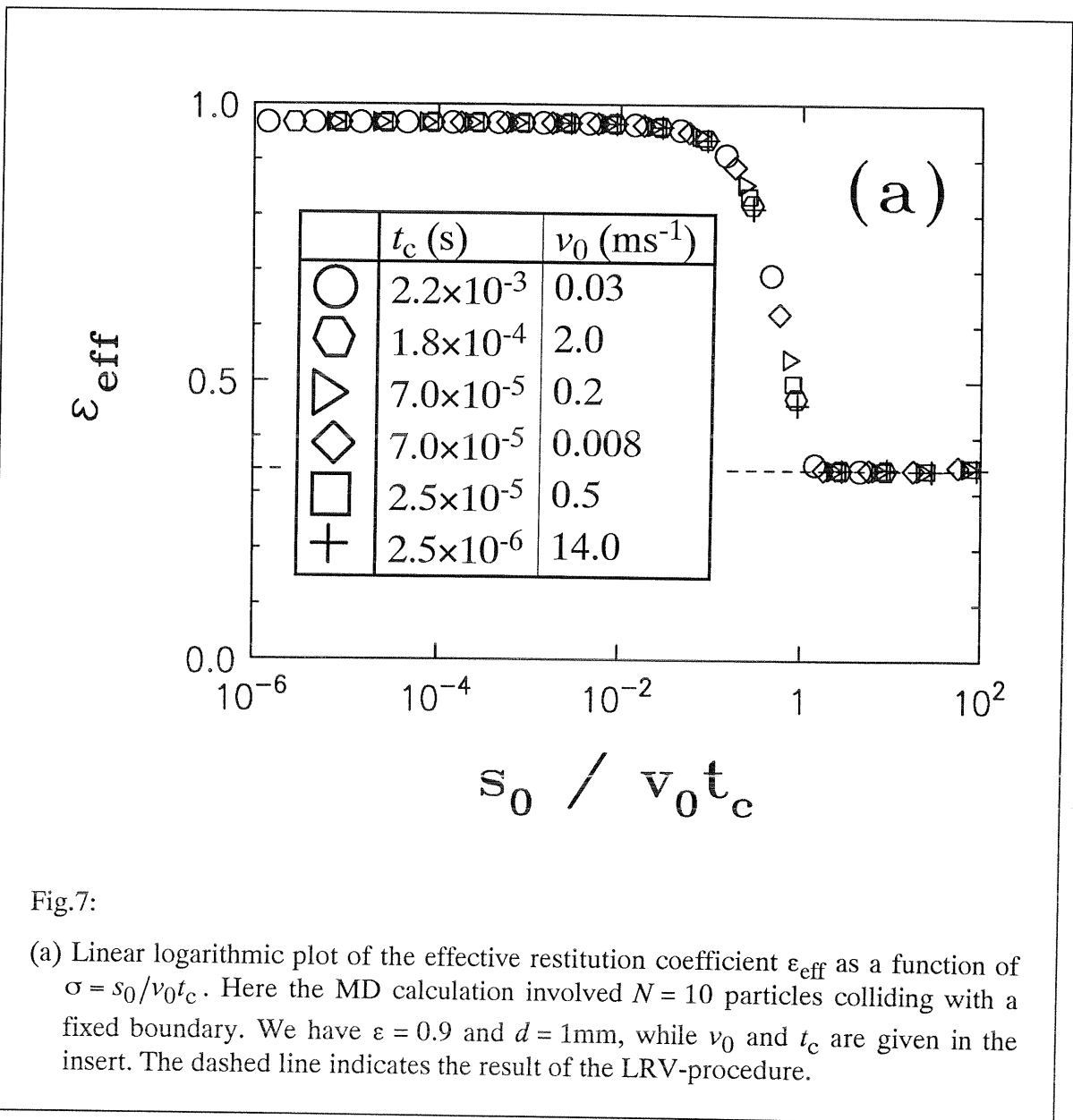|	t_c (s)	v_0 (ms^{-1})
◯	2.2×10^{-3}	0.03
⬡	1.8×10^{-4}	2.0
▷	7.0×10^{-5}	0.2
◇	7.0×10^{-5}	0.008
☐	2.5×10^{-5}	0.5
+	2.5×10^{-6}	14.0

Fig.7:

(a) Linear logarithmic plot of the effective restitution coefficient ε_{eff} as a function of $\sigma = s_0/v_0 t_c$. Here the MD calculation involved $N = 10$ particles colliding with a fixed boundary. We have $\varepsilon = 0.9$ and $d = 1$mm, while v_0 and t_c are given in the insert. The dashed line indicates the result of the LRV-procedure.

Figs.3(a-c)] as a function of the parameters: initial separation s_0, initial velocity v_0 and contact time t_c; we rescale the axes so that the ratio of the external time beween events s_0/v_0 to the internal contact time t_c shows up, i.e. we set $\sigma = s_0/(v_0 t_c)$. In Fig.7 we have $N = 10$, $d = 1$ mm and $\varepsilon = 0.9$. The initial velocity v_0 is varied between $14 \, \text{ms}^{-1}$ and $0.008 \, \text{ms}^{-1}$; t_c is varied between 2.2×10^{-3} s and 2.5×10^{-6} s. For each pair (v_0, t_c), s_0 is varied between 10^{-9} m and 10^{-3} m. In Fig.7(a) we plot ε_{eff} as a function of σ. We find that all results scale; they lie on a universal curve which only depends on σ. We also mention that a simulation with random initial separation, i.e. each particle i at position $z_i = i s_0$ is shifted by a random value taken from the interval between $-s_0/2$ and $s_0/2$, also falls on the same curve. Two features are proeminent: first, when $\sigma \ll 1$ [compare to Fig.3(a)] the energy loss is very small. This leads to large interparticle distances after the collision with the plate, a phenomenon which we call detachment effect. Second, for $\sigma \gg 1$ [compare to Fig.3(c)] the MD solution gets close to the ED result [compare to Fig.3(f)] and the energy loss turns out to be only slowly dependent on σ [right side of Fig.7(a)]. The ED procedure leads to $\varepsilon_{eff} \cong 0.341 \pm 0.002$ [the dashed line in Fig.7(a)] for various s_0 values ($s_0 = 0$, 10^{-7}, 10^{-6}, 10^{-5}, 10^{-4}, 10^{-3}, and 10^{-2} m), $N = 10$ and $\varepsilon = 0.9$. We varied v_0 between $20 \, \text{ms}^{-1}$ and $0.01 \, \text{ms}^{-1}$. As a general remark, we note that the ED procedure [36,62] leads to practically s_0 and v_0 independent ε_{eff}, and we find that ε_{eff} is considerably smaller than ε. Contrary, MD simulations lead to an ε_{eff} larger then ε for $\sigma \gg 1$.

Using MD methods we now analyse the case of a column with zero initial separation (cluster) colliding with a wall and look into the energy loss as a function of both internal (ε, t_c) and external (N) parameters. In Fig.7(b) and 7(c) we set $s_0 = 0$ m, $v_0 = 0.2 \, \text{ms}^{-1}$ and $t_c = 0.2 \times 10^{-4}$ s and vary N and ε. In Fig.7(b) we plot the effective dissipation $1 - \varepsilon_{eff}$ on double-logarithmic scales as a function of N for different ε; we find that $1 - \varepsilon_{eff}$ depends nonlinearly on the number of particles and that the energy loss *decreases* with increasing N. This is a rather surprising feature. In Fig.7(c) we plot the E_{rel}/E_f where E_{rel} is the relative energy and E_f is the kinetic energy after collision. The simulations are the same as in Fig.7(b). For $N = 10$ and $\varepsilon = 0.6$ we find, as an example, E_{rel}/E_f to be 0.056. This means that after the collision the particles separate; one has detachment.
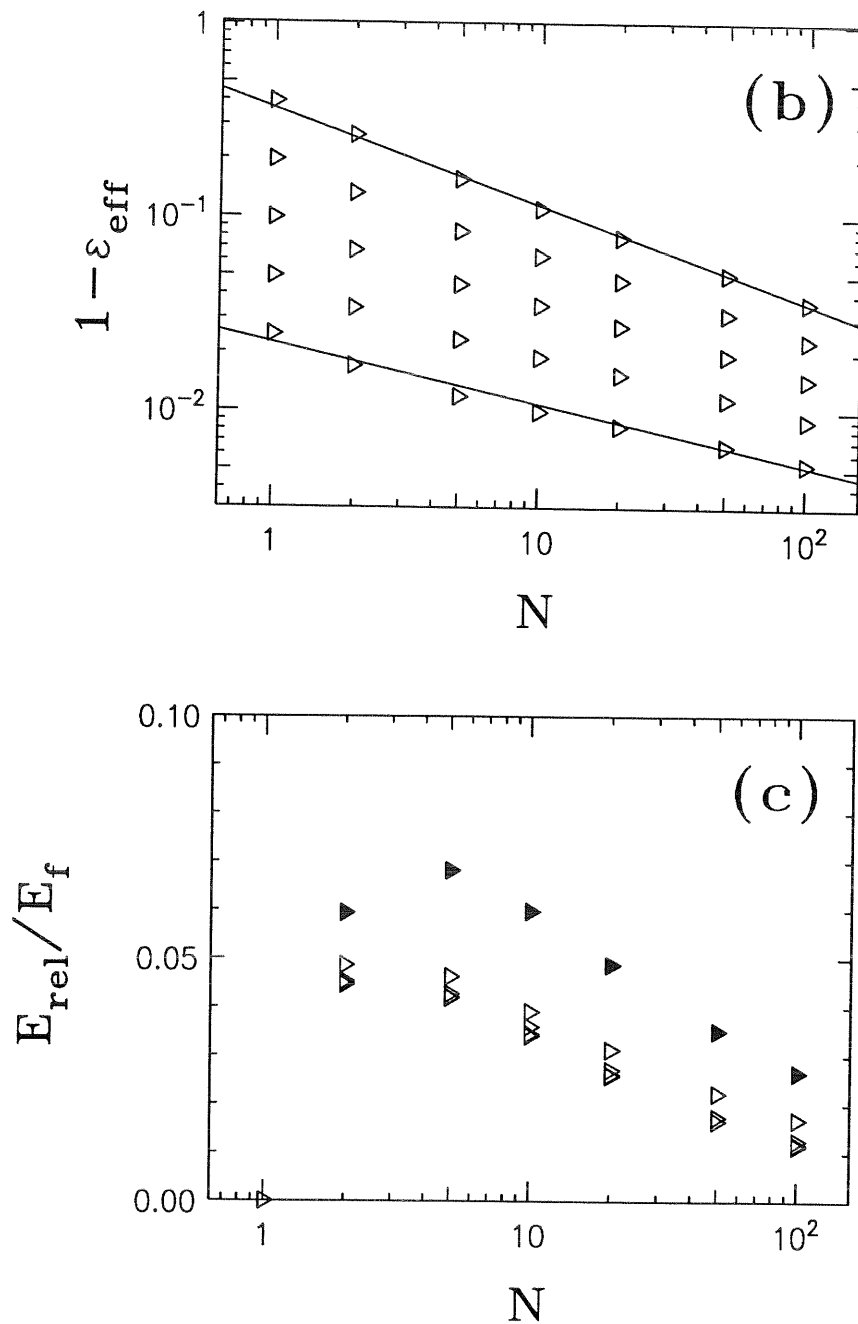
Fig.7:

(b) Log-log plot of $1 - \varepsilon_{eff}$ as a function of N for $s_0 = 0$, $v_0 = 0.05$ ms^{-1} and $t_c = 0.2 \times$ 10^{-4}s. N varies from 1, 2, 5, 10, 20, 50 to 100, and ε varies from 0.6, 0.8, 0.9, 0.95 to 0.975 from top to bottom for each N value. The dashed lines indicate the slopes -0.5 (top) and -0.315 (bottom).

(c) Plot of E_{rel}/E_f as a function of N. E_{rel} is the relative energy after the collision and E_f is the kinetic energy after collision. The parameters are as in Fig.7(b). The solid triangles correspond to $\varepsilon = 0.6$.

We also determined the interaction time, t_k, for the whole column with the wall from simulations with $s_0 = 0$ m. We find that t_k is *proportional* to the number of beads and to the contact time; hence $t_k \approx N t_c$. This is consistent with viewing the cluster as a series of elastic springs. Furthermore, we find that $E_{rel} \propto v_0^2$; by varying ε at the limit of low dissipation, $\varepsilon > 0.9$, we find that $\varepsilon_{eff} \propto \varepsilon$. Thus the detachment effect is the result of model-dependent dissipation properties. Inside the column the energy is dissipated in interactions involving particles with high relative velocities. Since during the collision with the wall the column of beads is compressed, the energy is dissipated preferentially between beads at the boundary of the compressed and the relaxed regions. Maintaining the other parameters, the size of the boundary area depends very little on N and leads to the nonlinear dependence on N. Even in the case of very high dissipation, i.e. $N = 10$ and $\varepsilon = 0.6$, detachment occurs, while ED simulations (Sec.2.2 and Appendix A) lead to an ε_{eff} which virtually vanishes, i.e. to a clustered column after collision.
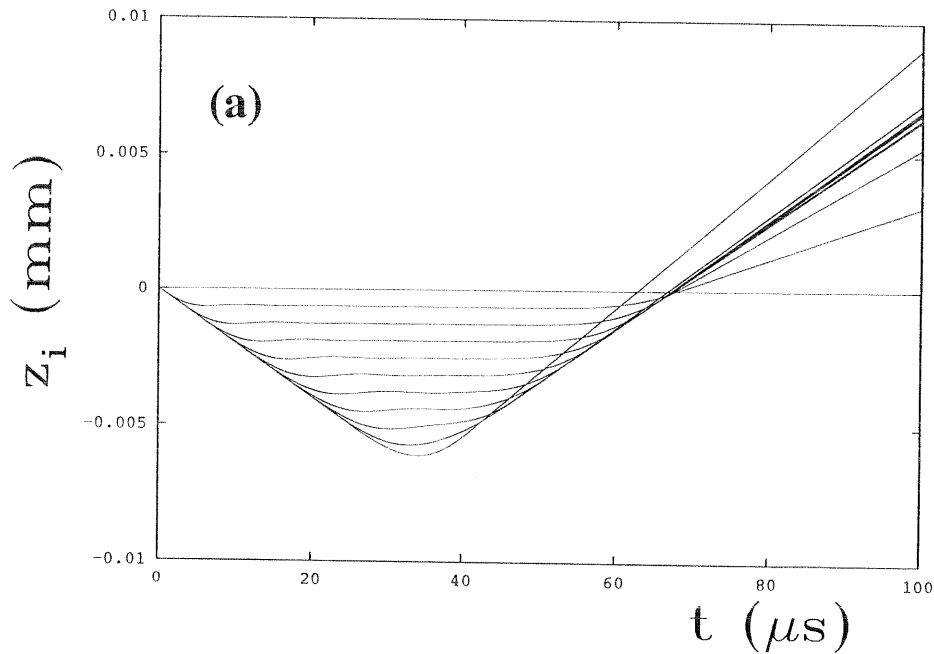

Fig.8:

(a) MD trajectories of the centers of $N = 10$ particles which collide with a fixed boundary. Here $\varepsilon = 0.9$, $t_c = 0.7 \times 10^{-5}$s, $v_0 = -0.2$ms^{-1} and $s_0 = 0$m. The positions are in reduced units, Eq.(9).
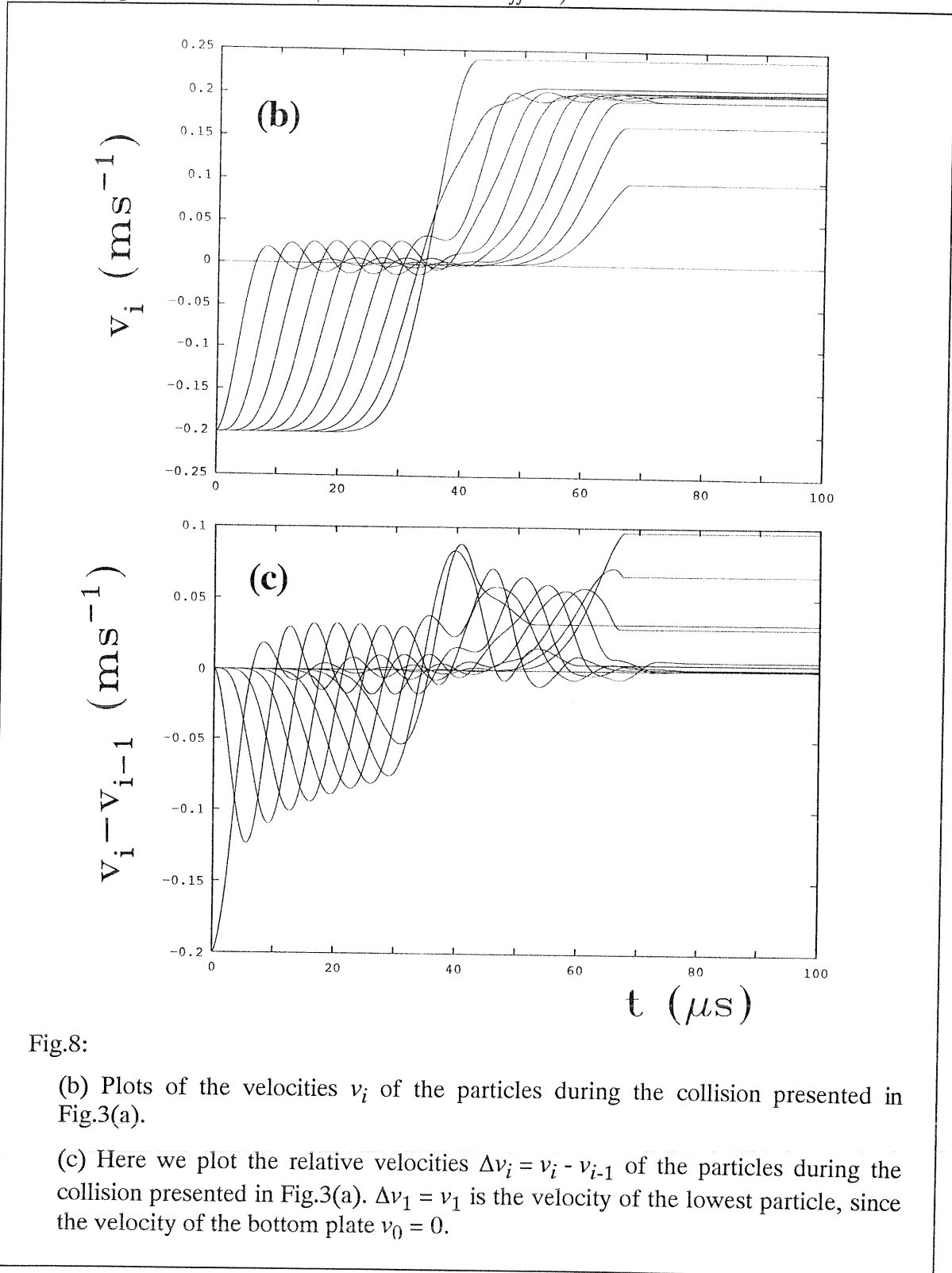
Fig.8:

(b) Plots of the velocities v_i of the particles during the collision presented in Fig.3(a).

(c) Here we plot the relative velocities $\Delta v_i = v_i - v_{i-1}$ of the particles during the collision presented in Fig.3(a). $\Delta v_1 = v_1$ is the velocity of the lowest particle, since the velocity of the bottom plate $v_0 = 0$.

To illustrate this, we plot a short time interval of the MD simulation already presented in Fig.3(a). In Fig.8(a) we plot the reduced coordinates. The reduced height becomes negative since the column is compressed; however, in Fig.8(b) we plot the

velocities of the particles. Note that due to the velocity dependent dissipation term for MD calculations the amount of dissipated energy depends on the relative velocities. Therefore, we plot in Fig.8(c) the relative velocities between neighboring particles. We observe complex particle behavior inside the column; the compression extends from bottom to top when the cluster hits the bottom plate. After the cluster is compressed the particles separate from each other during the subsequent decompression. The particles separate sequentially and lead to overall separation in the column.

3.2.2. The dependence of the detachment effect on the interaction law.

We carried out a series of simulations in 1D for different interaction laws and different numbers N of particles which hit the wall. In Fig.9 we plot the effective restitution coefficient as a function of N for $s_0 = 0$, $v_0 = 0.05 \text{ ms}^{-1}$, $d = 1 \text{ mm}$ and for different

Fig.9:

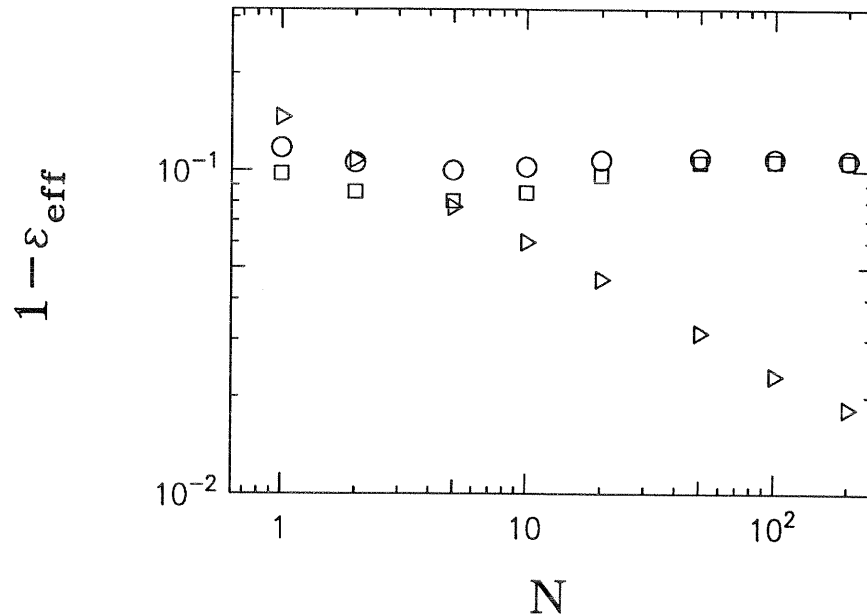The effective dissipation, i.e. $1 - \varepsilon_{\text{eff}}$, plotted as a function of N for $s_0 = 0$ and $v_0 = 0.05 \text{ms}^{-1}$. Here N varies from 1, 2, 5, 10, 20, 50, 100 to 200. We used the Hooke-interaction ($\beta = \gamma = 0$, triangles), the Hertz-interaction ($\beta = 1/2$, $\gamma = 0$, squares) and the Hertz-Kuwabara-interaction ($\beta = \gamma = 1/2$, circles). See text for details.

interaction laws. Using the linear interaction law with $\beta = \gamma = 0$, $K/m_{red} = 2\times10^9$ s^{-2}, and $D_n = 3.17\times10^3$ s^{-1} we find that ε_{eff} increases with N. Using the Hertz-type interaction, i.e. $\beta = 1/2$, $\gamma = 0$, with $K/m_{red} = 2\times10^{12}$ s^{-2}m$^{-1/2}$ and $D_n = 2\times10^3$ s^{-1} or a more general interaction, i.e. $\beta = \gamma = 1/2$, with $K/m_{red} = 2\times10^{12}$ s^{-2} m$^{-1/2}$, and $D_n = 10^5$ s^{-1} m$^{-1/2}$ we find that ε_{eff} varies little as a function of N. The net result is that the detachment effect is weaker for non-linear interactions; nonetheless there is still a fundamental difference from ED algorithms, for which ε_{eff} is close to zero for $N(1 - \varepsilon)$ large [62].

3.2.3. The detachment effect in 2D

Paralleling the 1D MD simulations we performed 2D calculations on a system of
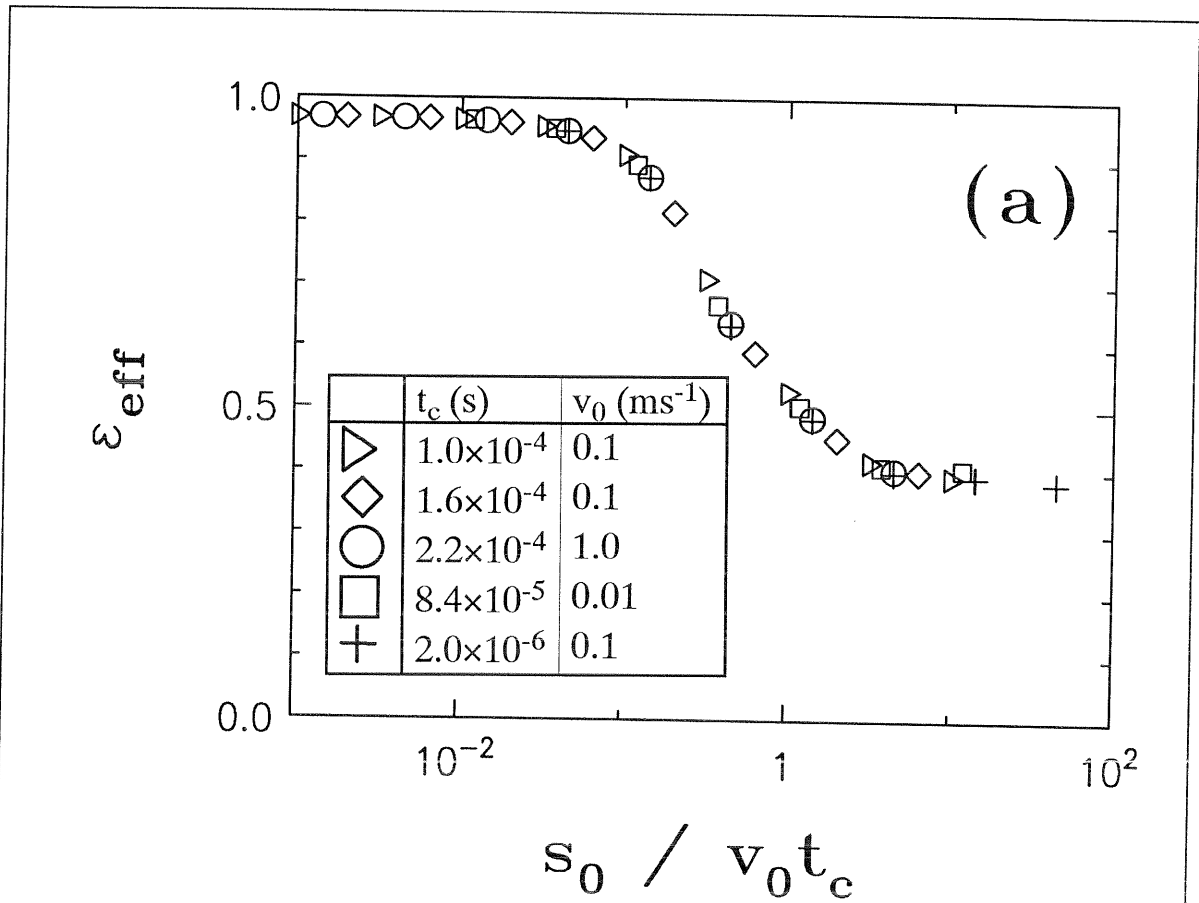

Fig.10:

(a) Linear logarithmic plot of the effective restitution coefficient ε_{eff} in two dimensions, as a function of $\sigma = s_0/(v_0 t_c)$. The parameters are $\varepsilon = 0.9$, $N = 130$ and $d = 1$ mm; v_0 and t_c are given in the insert.

particles which hit a wall. The initial velocity v_0 is taken to be the same for all particles. At the start we put all particles on a periodic, triangular lattice with a lattice-constant of $a = d + s_0$, width of $n_b = 13$ and height of $n_h = N/13$ lattice-points. Then we introduce randomness by shifting each particle horizontally and vertically by a random amount between $-s_0/2$ and $s_0/2$. We ensured that no overlap exists in the initial configuration. We let this system hit the wall and determine ε_{eff} after the collision. The process is considered to be over, when in a time interval of $2\,N\,s_0/v_0$ no collision occurs, i.e. no contact exists.

In Fig.10(a) we plot the effective restitution coefficient ε_{eff} as a function of $\sigma = s_0/(v_0 t_c)$ for $N = 130$ particles with $d = 1$ mm which collide with a wall. Here $\varepsilon = 0.9$ and s_0 varies between 10^{-7}m and 10^{-3}m, v_0 varies between 1 ms^{-1} and 0.01 ms^{-1} and t_c varies between 0.22×10^{-3}s and 0.2×10^{-5}s. The transition from the dissipative regime
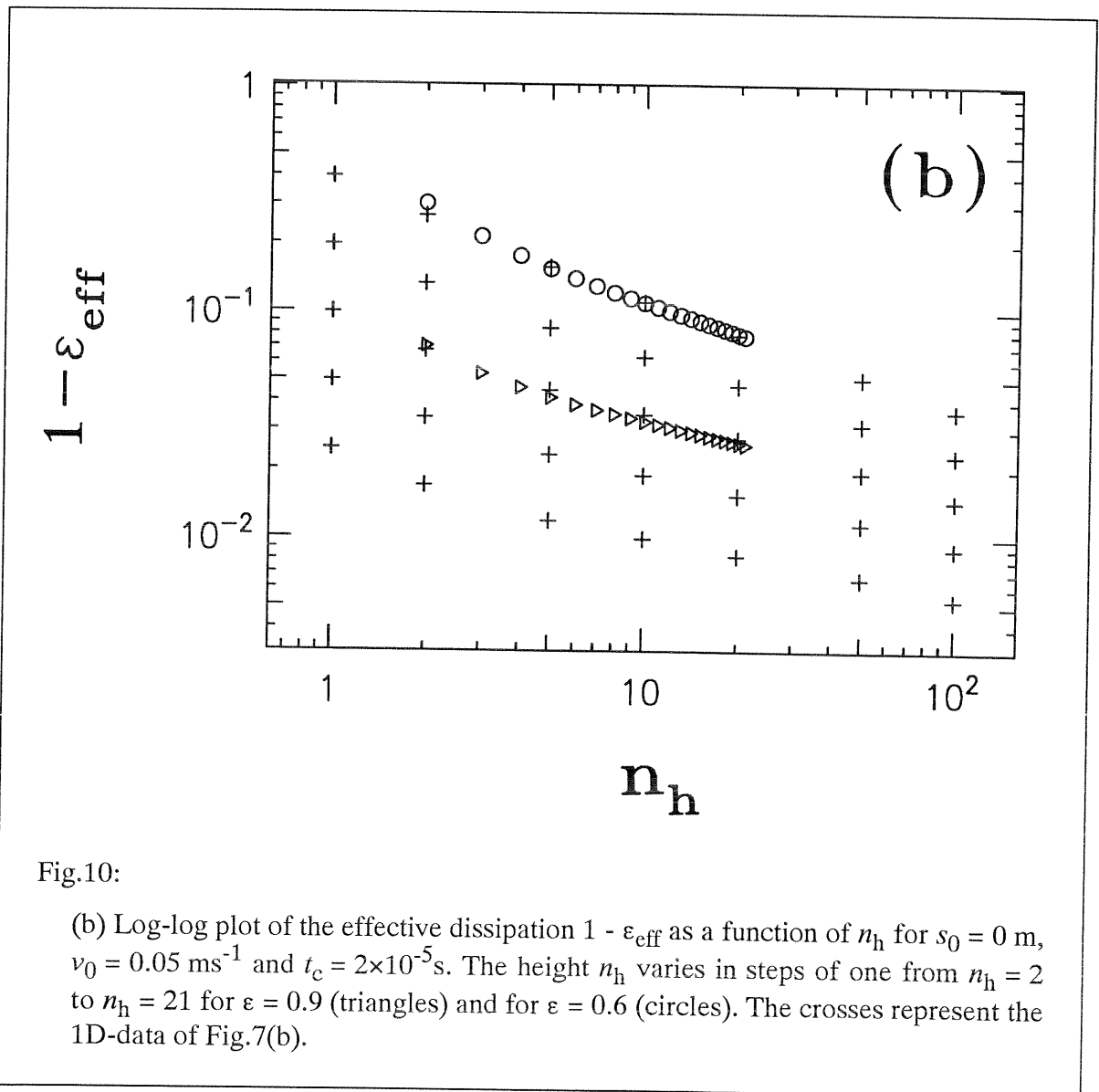

Fig.10:

(b) Log-log plot of the effective dissipation $1 - \varepsilon_{eff}$ as a function of n_h for $s_0 = 0$ m, $v_0 = 0.05$ ms^{-1} and $t_c = 2 \times 10^{-5}$s. The height n_h varies in steps of one from $n_h = 2$ to $n_h = 21$ for $\varepsilon = 0.9$ (triangles) and for $\varepsilon = 0.6$ (circles). The crosses represent the 1D-data of Fig.7(b).

(large σ) to the detachment regime (small σ) is less sharp in 2D, in which the transition takes place in the interval $0.1 < \sigma < 10$, than in 1D, in which the transition takes place in the interval $0.1 < \sigma < 1$. Note that at both limits (small or large σ) ε_{eff} does not depend on the dimensionality, but only on the height $n_h = N/n_b$ (in 1D $n_b = 1$) and on ε. This is also obvious from Fig.10(b), where we plot the effective dissipation $1 - \varepsilon_{eff}$ as a function of n_h for vanishing initial separation s_0. We use $\varepsilon = 0.6$ (circles) and $\varepsilon = 0.9$ (triangles) and compare the 2D data with the 1D results (crosses), already displayed in Fig.7(b). From this Figure we infer that arrays of particles with equal height behave similarly in 1D and in 2D, as long as the particle separation is small.

3.2.4. Consequences of the detachment effect

The problem with numerical simulations is the computer time required. A basic feature of the mechanical model considered by us for MD simulations is the contact time t_c between two colliding beads, estimated in the above case to be around 4 μs [Sec.3.1.2]. MD simulations update the system at fixed time intervals $t_{MD} \ll t_c$, so that in theory one should have some 10^6 to 10^7 updates to simulate one second. MD calculations commonly circumvent the problem by making updates at much longer time intervals than neccessary for t_c and try to compensate by reducing elasticity and dissipation. But if t_c is increased, the ratio σ may be decreased into a regime where detachment occurs. This is the reason, why one has to choose the parameters for the MD simulations carefully.

Even though no detachment connected with small energy loss occurs ED simulations update (i) only when an event (collision) happens, and (ii) mostly only the colliding pair; thus ED methods demand less time for systems with rather longer times between the events. We note that in situations in which the particles contact each other very often, the computing time needed for ED algorithms becomes very large.

We demonstrated in this section that ED and MD simulations of simple toy-models may lead to different results. The open question is now under which circumstances ED and MD calculations of vibrated systems agree and, more importantly, under which circumstances numerical simulations will reproduce experimental results.

4. Results of Simulations in 1D

We now turn to a discussion of systems in 1D including gravitation and a sinusoidally moving bottom plate. The parameters involved are the number of beads N, the restitution coefficients ε_p and ε, as well as the amplitude A_0, and the angular frequency $\omega = 2\pi f$. Some numerically established data are experimentally accessible and are compared with the measurements.

4.1. The model system in 1D

We use a system of N beads in the numerical simulations in order to draw parallels to recent experiments [36,62]. In the experiment the beads have a well-defined diameter of d=2.99 mm and are enclosed in a cell, which is a vertical groove with width and depth of both 3 mm, cut in a rectangular block of brass with a height of 85 mm; a glass window in the front permits the visualization. A CCD-camera hooked up to an image processing device was used to monitor the experiments. The horizontal bottom of the groove consists of a glass plate, and the sound created by the collisions of the beads was recorded, through a microphone which was connected to a memory oscilloscope. A schematic drawing of this system was given in Fig.1.

Because of the geometry, the beads are aligned so that each bead interacts only with its upper and lower neighbours or, for the lowest bead, with the vibrating bottom plate. In the simulations we neglect the contacts the beads have with the walls of the groove and assume that the kinetic energy is only lost due to the inelasticity of the collisions. The fundamental parameter which describes this dissipation is the restitution coefficient ε of the momentum for a collision between beads. In the simulations we account both for collisions between two individual beads (binary collisions) as well as for collisions which involve several beads in contact (clusters). The general numerical approach was introduced in subsection 2.2. and some details of the procedure are described in Appendix A.

The restitution coefficient ε is material dependent; collisions of the lowest bead with

the bottom plate may also have a different restitution coefficient, which we denote by ε_p. In order to examine the two limiting cases of high and of low dissipation, we experimented with beads made of aluminum and made of stainless steel, respectively. We measured ε in a rough manner by the rebound method and obtained $\varepsilon=0.60\pm0.05$ for aluminum on aluminum and $\varepsilon=0.90\pm0.05$ for stainless steel on stainless steel.

4.2. The behavior of 1 bead on a vibrating plate

We assume one particle on a vibrating bottom plate [Eq.(7)] in the gravitational field. In the case of a collision of the particle with the bottom plate we follow Eq.(13) to calculate the velocity of the particle after the collision. The one-bead problem has been studied extensively in the past [68-70,79]. The situation of one particle with vanishing restitution coefficient is interesting for the case of many particles with a non-zero restitution coefficient because energy is dissipated due to frictional contacts and a large number of collisions. If there are many particles a large amount of energy is dissipated. A cluster of many particles with $\varepsilon \neq 0$, thus may be substituted by one particle with $\varepsilon = 0$.

In general, the behavior of one particle on a vibrating plate, is characterized by the phase φ_i, at which the particle leaves the bottom plate and the phase φ_{i+1} of the next contact with the bottom plate. Here we give an iterative scheme for the phases, when a particle touches the bottom plate. At phase $\varphi_{i+1} = \omega t_{i+1}$, we set the position of the bottom plate [Eq.(7)] equal to the position of the particle with initial position $A_0 \sin(\varphi_i)$ and initial velocity v_i in the gravitational field:

$$A_0 \sin(\varphi_{i+1}) = A_0 \sin(\varphi_i) + v_i \frac{\varphi_{i+1}-\varphi_i}{\omega} - \frac{g}{2}\left(\frac{\varphi_{i+1}-\varphi_i}{\omega}\right)^2 .$$

(28)

$(\varphi_{i+1} - \varphi_i)/\omega$ is the time elapsed since $t_i = \varphi_i/\omega$. Together with the phase φ_{i+1} and the new velocity v_{i+1} just after contact with the bottom plate, we are able to calculate the phase of the next contact φ_{i+2}, by simply iterating Eq.(28).

For the completely inelastic case ($\varepsilon = 0$) the velocity after contact with the bottom plate always equals the velocity of the bottom plate $v_i = A_0\omega \cos(\varphi_i)$ if the acceleration of the bottom plate is greater than the gravitational acceleration g, i.e. $\sin(\varphi_i) \geq 1/\alpha$. Using Eq.(28), inserting v_i and dividing the whole equation by A_0 we obtain

$$\sin(\varphi_{i+1}) = \sin(\varphi_i) + \cos(\varphi_i)(\varphi_{i+1} - \varphi_i) - \frac{1}{2\alpha}(\varphi_{i+1} - \varphi_i)^2 .$$

(29)

Otherwise, if the acceleration at the moment of contact is less than g, the particle moves

together with the bottom plate until it lifts off tangentially at phase $\varphi_1 = \arcsin(1/\alpha)$. Replacing φ_i by φ_1 and φ_{i+1} by φ_2 in Eq.(29) we obtain

$$\sin \varphi_2 = (1 + \sqrt{\alpha^2 - 1} \, (\varphi_2 - \varphi_1) - 1/2(\varphi_2 - \varphi_1)^2)/\alpha \qquad (30)$$

for all φ_i with $\sin(\varphi_i) < 1/\alpha$. Note that the phases in Eqs.(29) and (30) depend on the acceleration α and not explicitly on A_0 or ω. In Fig.11 we plot the scaled height of the bottom plate $\sin(\varphi_2)$ and the motion of one particle as a function of the scaled phase $p = \varphi/2\pi$ for $\alpha = 2$. p_1 and p_2 give the scaled phases φ_1 and φ_2 respectively. The numerically computed values of φ_2 as a function of α are plotted in Fig.12(a). We compare
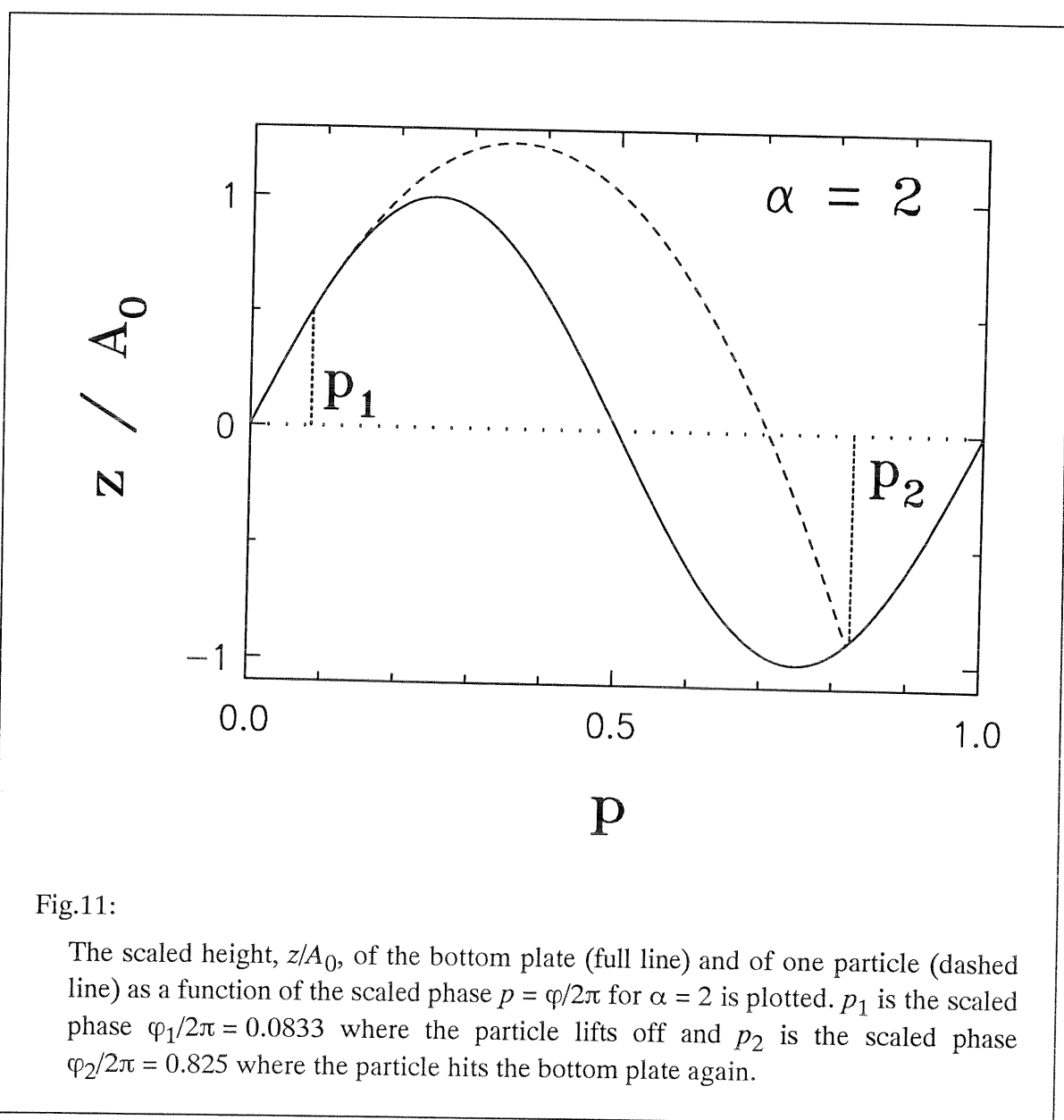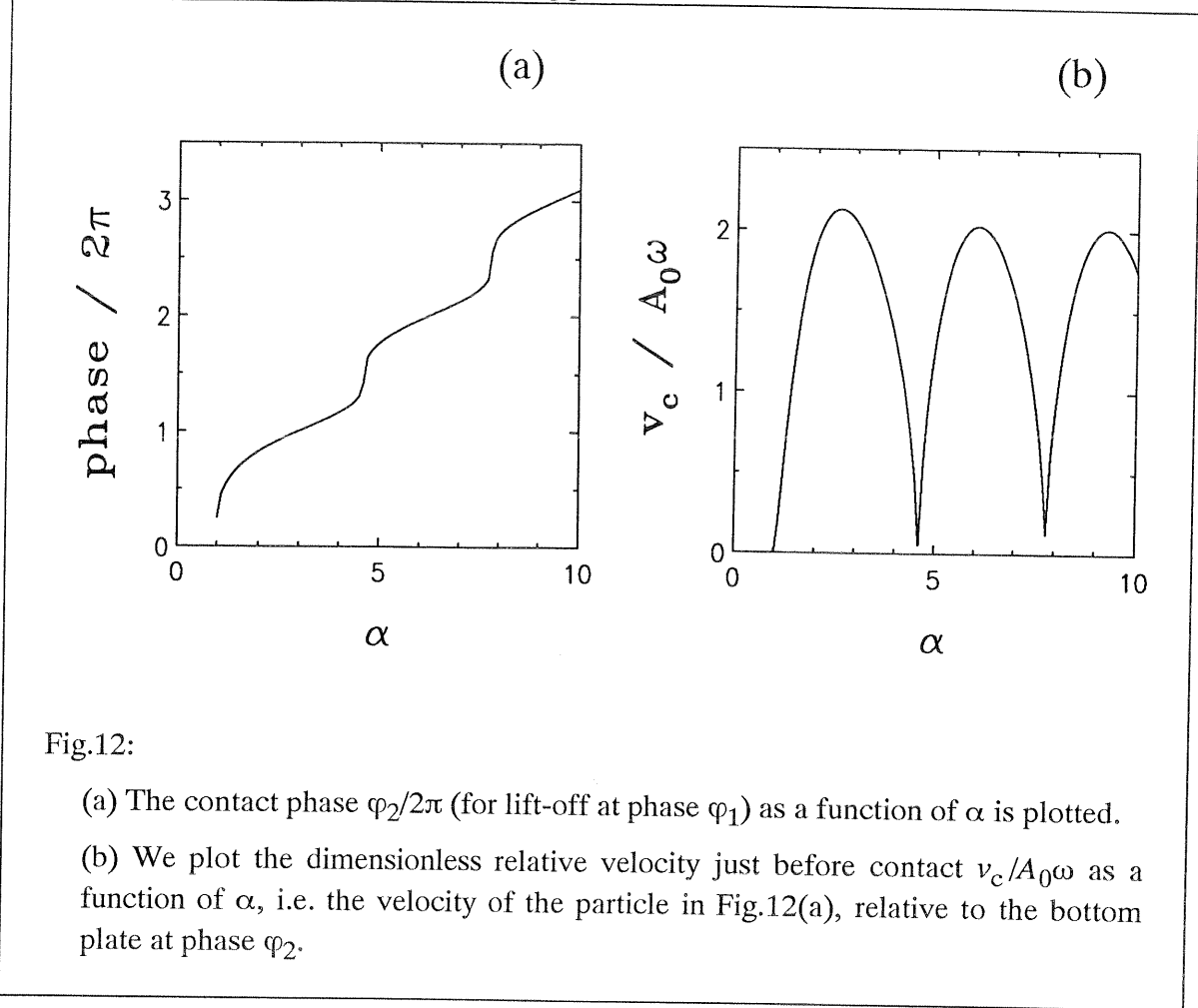

Fig.11:

The scaled height, z/A_0, of the bottom plate (full line) and of one particle (dashed line) as a function of the scaled phase $p = \varphi/2\pi$ for $\alpha = 2$ is plotted. p_1 is the scaled phase $\varphi_1/2\pi = 0.0833$ where the particle lifts off and p_2 is the scaled phase $\varphi_2/2\pi = 0.825$ where the particle hits the bottom plate again.

(a)

(b)

Fig.12:

(a) The contact phase $\varphi_2/2\pi$ (for lift-off at phase φ_1) as a function of α is plotted.

(b) We plot the dimensionless relative velocity just before contact $v_c/A_0\omega$ as a function of α, i.e. the velocity of the particle in Fig.12(a), relative to the bottom plate at phase φ_2.

results, obtained through ED simulations (circles) with a numerical solution of Eq.(30) (full line). From φ_2, we compute the relative velocity v_c before contact at phase φ_2. v_c is the difference between the velocity of the bottom plate $[v_p = A_0\omega\cos(\varphi_2)]$ and the velocity of the particle $[v_2 = v_1 - \frac{g}{2}\left(\frac{\varphi_2 - \varphi_1}{\omega}\right)]$ at phase φ_2:

$$v_c = A_0\omega(\cos\varphi_2 - \cos\varphi_1 + (\varphi_2 - \varphi_1)/\alpha) \ . \tag{31}$$

v_c scaled by the typical velocity $A_0\omega$ as a function of α is plotted in Fig.12(b). The relative velocity before collision has large values, when the particle hits the bottom plate at a phase when the bottom plate moves upwards. Low v_c values correspond to phases when the bottom plate moves downwards. The motion of one particle on a vibrating bottom plate is characterized by the dimensionless acceleration α. The motion of a cluster with an effective restitution $\varepsilon_{eff} = 0$, should therefore lead to similar behavior. We now turn to the discussion of N particles with $\varepsilon_{eff} > 0$ on a vibrating bottom plate.

4.3.   The transition from a fluidized to a condensed regime

For restitution coefficients close to one and at high accelerations of the bottom plate the individual motion of the beads looks erratic. This is what we call *fluidization*. If the input energy is decreased, the motion becomes more and more regular and the column of beads eventually gets locked onto the excitation period. This is what we call *condensation*. In Figs.13 we show three typical forms of column behavior depending on the input energy of the system. The parameters used are $N = 10$, $f = 20\ s^{-1}$, $\varepsilon_p = 1$, and $\varepsilon = 0.92$. The amplitude A_0 varies from 4.97 mm in Fig.13(a) to 1.24 mm in Fig.13(b) and 0.932 mm in Fig.13(c). In Figures 13(a), 13(b) and 13(c), α [Eq.(8)] is 8.0, 2.0 and 1.5 respectively. The trajectories of the particles show the progressive condensation of the column. To illustrate this change of behavior we use a grey code: light grey indicates high velocities and dark grey low velocities. It is evident from Figs.13 that for lower acceleration values the motion is collective; at higher acceleration values we find that the role of the fluctuations increases. In the inserts of Figs.13 we show the frequency spectra obtained through a fast Fourier transform (FFT) algorithm for the motion of the center of mass (cm). In the FFT algorithm the position of the diameter dependent height of cm (h_{cm}) was evaluated 25 times per period during a total of some 328 periods, within which 2^{13} data points were obtained. At still higher energies, the motion of the cm displays a continuous spectrum, see Fig.13(a). When the input energy decreases, the motion of the center of mass begins to show the harmonics and the subharmonics of the excitation frequency, Fig.13(b). If the energy decreases more, Fig.13(c), a Feigenbaum scenario is observed, a bifurcation cascade which displays period doubling.

Fig.13:

    (a) Motion of 10 beads for $f = 20$ s^{-1}, $\alpha = 8.0$, $\varepsilon = 0.92$ and $\varepsilon_p = 1$.
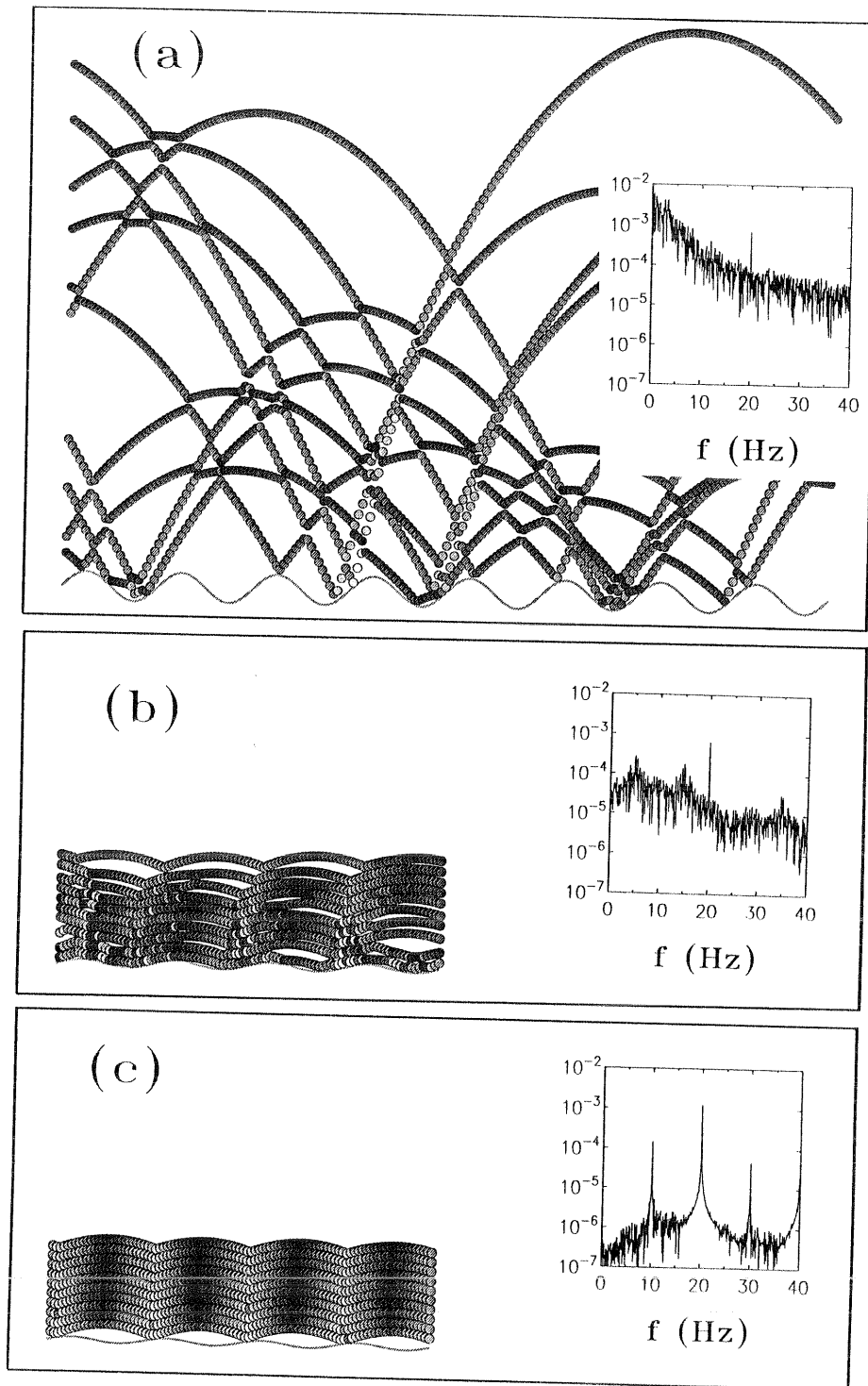
    (b) Motion of 10 beads for $f = 20$ s^{-1}, $\alpha = 2.0$, $\varepsilon = 0.92$ and $\varepsilon_p = 1$.

    (c) Motion of 10 beads for $f = 20$ s^{-1}, $\alpha = 1.5$, $\varepsilon = 0.92$ and $\varepsilon_p = 1$.

The inserts displays the frequency spectrum for the motion of the center of mass.
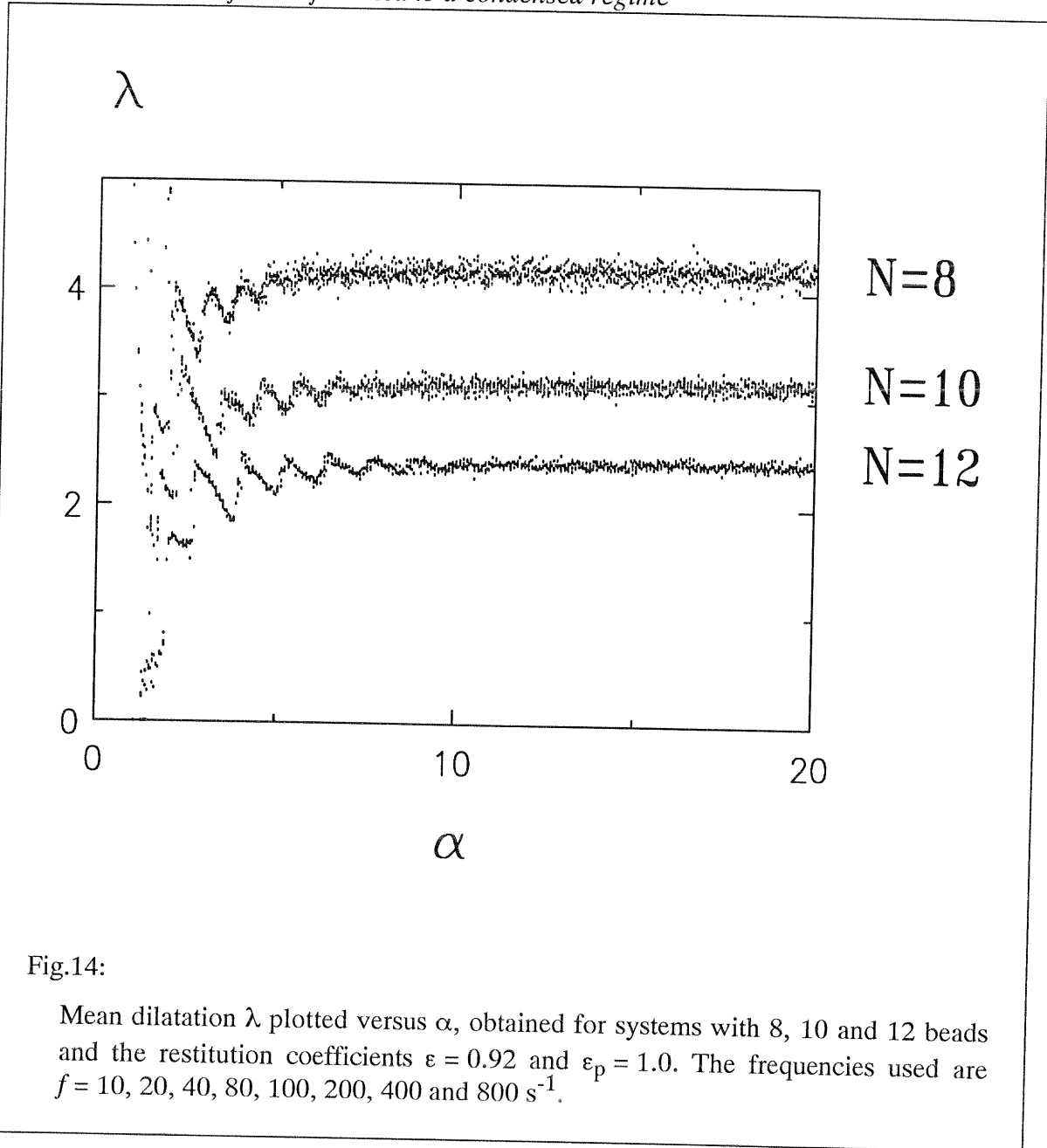
4.3.1. The dilatation of a column of particles

The passage from a fluidized state [Fig.13(a) - with the quasi-ballistic trajectories for the momentum waves] to a state involving collective motions of the column is gradual, see Figs.13(b) and 13(c). To monitor this behavior, we look at the mean dilatation of the column $<z_N-z_1>$ where z_1 and z_N are the height of the first and the N th particle. We recall that the z_i-coordinates are independent of the bead diameters, see Eq.(9). The mean dilatation is a good indicator of clusterization. In Fig.14 we depict the dilatation using the dimensionless quantity λ:

$$\lambda = \frac{\langle z_N - z_1 \rangle}{A_0 \alpha} \, . \tag{32}$$

We display λ as a function of α for $N = 8$, 10 and 12, while maintaining $\varepsilon=0.92$. The frequencies used are $f = 10$, 20, 40, 80, 100, 200, 400 and 800 s^{-1} and we vary the amplitude A_0. Note that for a given N, all the curves collapse on the same master curve. For high energy input corresponding to large α-values λ converges to a constant. Since at this limit we have $<z_1> \,<<\, <z_N>$, for fixed N the mean dilatation is proportional to the potential energy; the scaling behavior, Eq.(32) thus indicates that $<z_N-z_1>$ and hence the potential energy are also proportional to $A_0\alpha$. Therefore, in the fluidized regime the potential energy scales with $A_0^2\omega^2$. In other words, at the fluidized limit a proper scaling parameter is the squared velocity $(A_0\omega)^2$ and not the acceleration α. If α becomes less (say for $\alpha<10$) the column behaves in a complex fashion and resonances may show up. But α is not the only control parameter for the occurrence of condensation; for different N we find different behavior for the same α-values. Thus columns with larger N show less dilatation. This is due to the fact that the number of dissipative contacts increases with N; a system with larger N displays a higher dissipation. Note that for a dissipative block or a completely inelastic particle on a vibrating plate the pertinent control parameter is the relative acceleration α [68-70]. As a result one has a very complex transition between the *fluidized* state and the *clustered* regime, a transition which depends on N, on ε and also on α.

Fig.14:

Mean dilatation λ plotted versus α, obtained for systems with 8, 10 and 12 beads and the restitution coefficients $\varepsilon = 0.92$ and $\varepsilon_p = 1.0$. The frequencies used are $f = 10, 20, 40, 80, 100, 200, 400$ and 800 s^{-1}.

In the fluidized regime, the erratic motion of particles and the large dilatation of the column may suggest some analogy with the behavior of a dense gas column when connected to a heat bath, and in general to thermodynamic concepts. Mazighi, Bernu and Deylon [49] recently found an analytic description for a one-dimensional array of beads where the bottom plate follows a triangular instead of a sinusoidal function. There they find, using the dissipative Boltzmann equation, at the limit of low dissipation a density profile which is nearly exponential. We remark that the function of the bottom plate is analogous to a heat bath in providing, and sometimes taking away, energy from the system. Furthermore, we like to point out that other thermodynamic and/or hydrodynamic ideas have been advanced to describe a granular assembly [76-78]. Thus 1D columns of beads seem to be

good candidates with which to test the relevance of such an approach. But one has to pay attention to the fact that even in such "one-dimensional" systems experimentally additional effects, such as rotations, may appear and that important aspects of realistic three-dimensional systems are neglected.

We are interested in the qualitative features of the density and of the kinetic energy distributions. In Fig.15(a) we present the density of the beads as a function of the height. The density is evaluated for $N = 10$, $\varepsilon = 0.92$, and $f = 20$ s^{-1}. Here we use the diameter dependent coordinates $h_i(t)$, introduced in Eq.(9), and a diameter of $d = 3$ mm. In Fig.15(a) we show the density profiles $\rho(h)$ for different α-values (here $\alpha = 2, 3, 5$ and 8). We have also evaluated the corresponding kinetic energy profiles, by defining $\theta(h) = <v(h)^2>$. In Fig.15(b) we plot θ as a function of the height h.

With increasing α the density ρ becomes less and extends to higher h (fluidization); furthermore, θ basically decreases with increasing h; θ-curves belonging to different α-
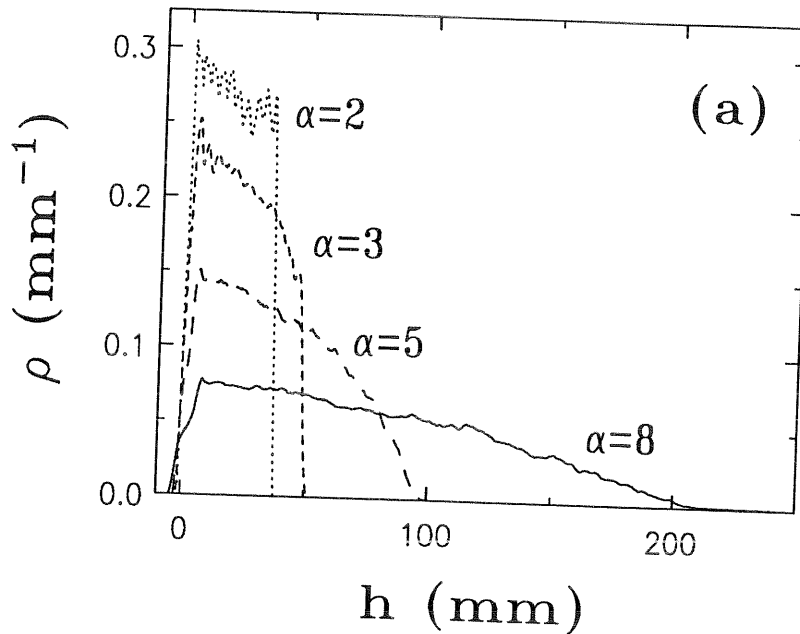

Fig.15:

(a) The number density profiles $\rho(h)$ are shown for $N = 10$, $\varepsilon = 0.92$, $\varepsilon_p = 1.0$ and $f = 20$ s^{-1} as a function of h with $d = 3$ mm for $\alpha = 2, 3, 5$ and 8.
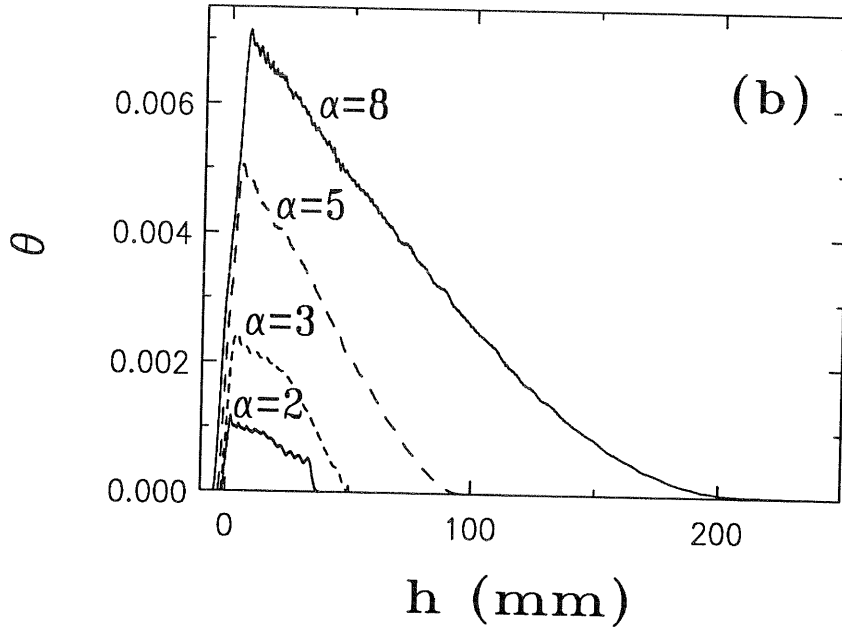
Fig.15:

(b) The kinetic energy-profiles $\theta(h)$ are shown for $N = 10$, $\varepsilon = 0.92$, $\varepsilon_p = 1.0$ and $f = 20$ s^{-1} as a function of h with $d = 3$ mm for $\alpha = 2, 3, 5$ and 8.

values do not cross.

4.3.2. The dissipation time in the fluidized regime

The following study is meant to work out the characteristic features of the fluidized regime and the conditions under which *condensation* and/or *clusterization* is obtained. We consider the mean dissipation time τ_D of the energy input in a steady state, taking the energy $\mathcal{E}$ to be zero when all beads are at rest and lie on the plate. τ_D is the ratio of the average total energy $<\mathcal{E}>$ of the system in a steady state relative to the input (or equivalently, the output) power $<P>$:

$$\tau_D = \frac{\langle \mathcal{E} \rangle}{\langle P \rangle} . \tag{33}$$

48

Evidently τ_D measures the energy dissipation in the system: on the time-scale of τ_D the kinetic energy which is introduced into the system by the motion of the bottom plate is dissipated through collisions. We note that on the average the input power is positive: Although some collisions of the bottom plate may take energy away from the column of beads, on the average the bottom plate feeds energy into the system.

Fig.16:

The dissipation time τ_D is shown in a steady state. The plot gives $\tau_D f$ as a function of α for the same parameters as in Fig.14.

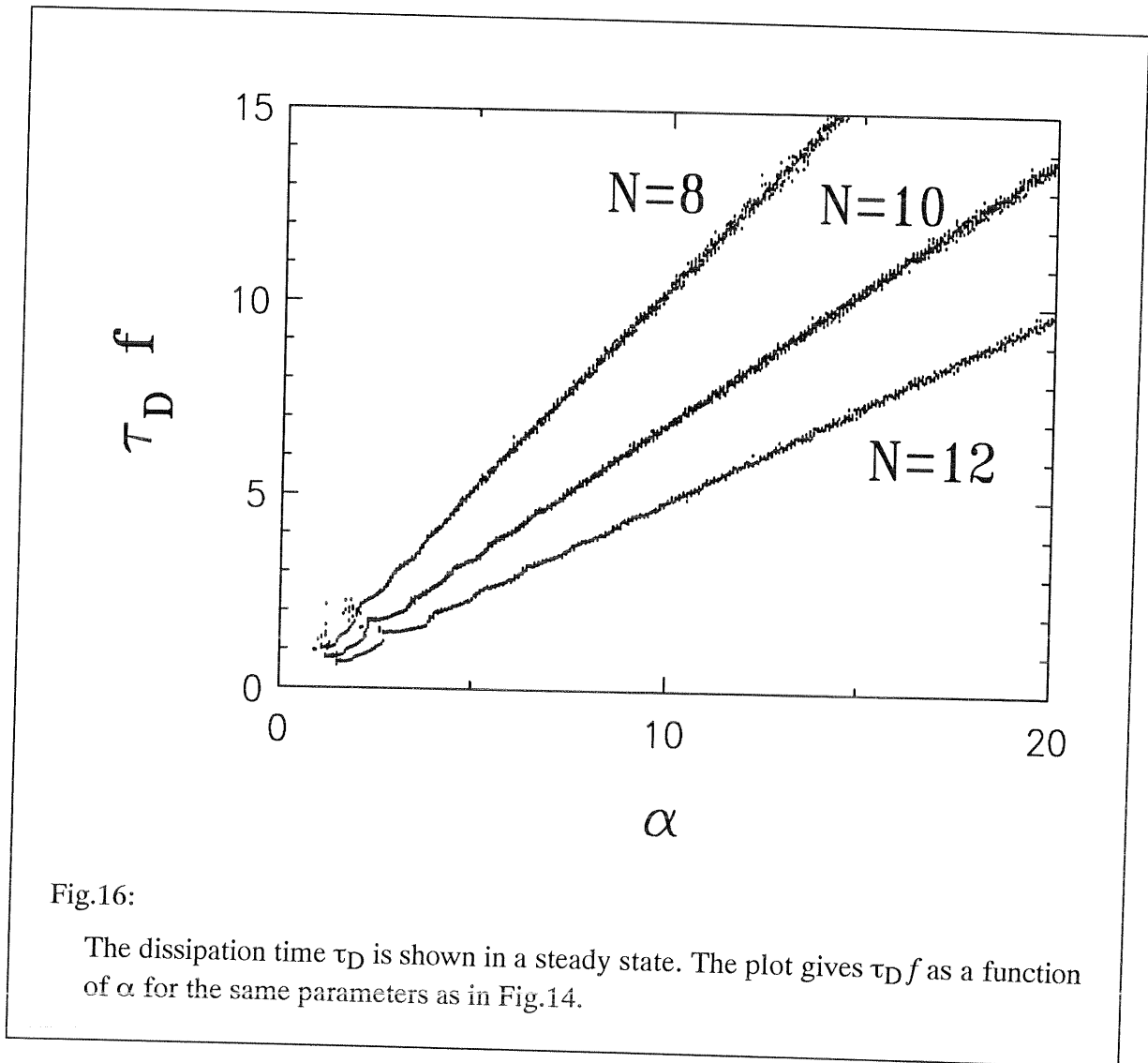Fig.16 was obtained by following the simulations to times considerably larger than τ_D; displayed is the dissipation time τ_D at steady state, as a function of α. The parameters of the simulation are the same as those used to obtain Fig.14. We see that all data fall on a master curve which depends on N. Thus $\tau_D f$ is proportional to α and therefore in the fluidized regime:

$$\tau_D \propto \frac{2A_0\omega}{g} \quad .$$ (34)

In Eq.(34) τ_D is proportional to the time of a ballistic flight with an initial velocity of $A_0\omega$, but for the moment nothing is said about the prefactor, which will be a function of N and ε. The dissipation time is larger for smaller N, because this corresponds to a smaller number of dissipative contacts. For small $\tau_D f$-values we observe (as in Fig.14) a wiggly structure superimposed on the master curves. This is typical for the transition zone between the fluidized and the condensed state.

4.3.3. Scaling behavior of the fluidized phase

Now we look at the scaling behavior of the relative height of the center of mass. In the fluidized regime, this quantity is proportional to the total energy and it can be directly measured from the experiments. As we have shown in the previous paragraph, a cross-over between a condensed regime and a fluidized regime is evidenced when the dissipation time is of the order of the excitation period. In this paragraph we work in the fluidized regime; therefore, for each numerical result, we verified that the dissipation time was much larger than the excitation period. Moreover, we make sure that the simulations have reached a steady state before the average data were produced, i.e. we start the average at $t = 10\,\tau_D$ and end at $t = 50\,\tau_D$.

We denote the height of cm by h_{cm0} when the system rests on the bottom plate; thus $h_{cm}\text{-}h_{cm0}$ is diameter independent. From dimensional analysis and according to Eq.(34), it is obvious that the relative height of the center of mass should scale with a typical velocity square $(A_0\omega)^2$, the prefactor being a dimensionless function $F(N,\varepsilon)$.

$$h_{cm} - h_{cm0} = \frac{A_0^2\omega^2}{g}F(N,\varepsilon) \quad .$$ (35)

To determine the function $F(N,\varepsilon)$ we carried out a series of simulations by varying α ($\alpha=10,...,10000$), varying N ($N=2,...,100$) and varying ε ($\varepsilon=0.9995,...,0.01$); ε_p is either held equal to one or set to $\varepsilon_p=\varepsilon$.

Fig.17:

(a) The diameter independent height of the center of mass is plotted as a function of (1-ε) for different N-values and for $\alpha = 10$ and $\varepsilon_p = 1$. Crosses, triangles and squares correspond to $N = 20$, 10 and 5 respectively, while the dashed line gives a slope of -1.
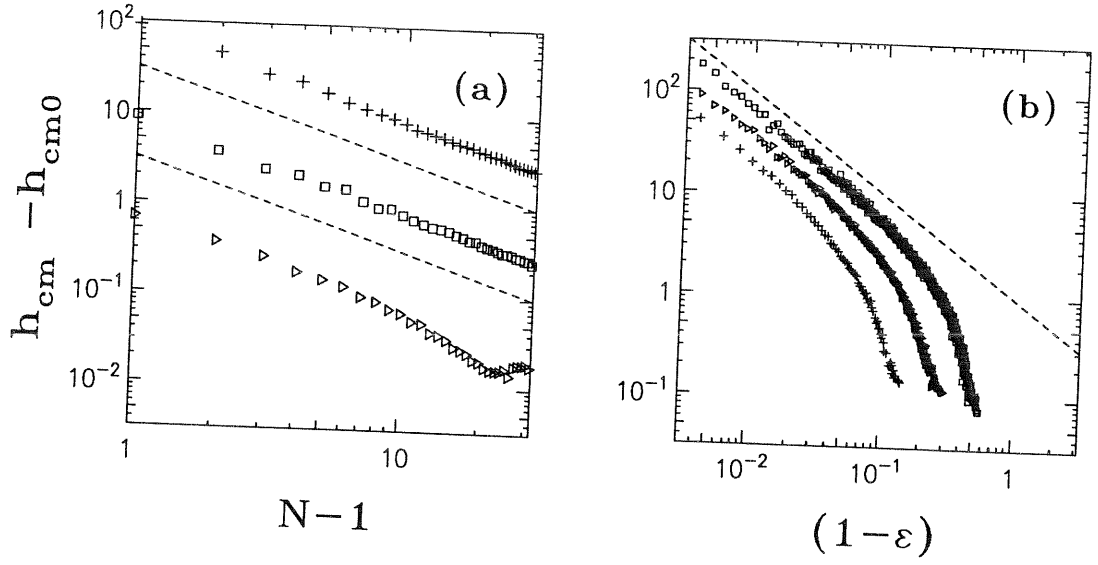
(b) The diameter independent height of the center of mass is plotted as a function of N-1, for different ε-values and for $\alpha = 10$ and $\varepsilon_p = 1$. Crosses, squares and triangles correspond to $1 - \varepsilon = 10^{-3}$, 10^{-2}, 10^{-1} respectively, while the dashed lines give a slope of -1.

In the following we will first find the behavior in the nearly elastic regime. The height of cm diverges for ε→1, since in this case very little energy is dissipated per collision and around this limit fluidization is more likely to occur. Fig.17(a) shows $h_{cm}-h_{cm0}$ as a function of (1 - ε) for $\alpha = 10$, $\varepsilon_p = 1$ and $N = 5$, 10 and 20. We obtain at the limit ε→1:

$$h_{cm} - h_{cm0} \propto (1 - \varepsilon)^{-\beta_1} \qquad (36)$$

with $\beta_1 = 1.00\pm0.02$. The next step is to find the N-dependence of $h_{cm}-h_{cm0}$. It is obvious that the cm is higher for smaller N and vice versa. We propose that $h_{cm}-h_{cm0}$ should depend on the number of dissipative contacts in the system which is N-1 for $\varepsilon_p = 1$ and N for $\varepsilon_p = \varepsilon$. Fig.17(b) gives simulation results for $h_{cm}-h_{cm0}$ as a function of N-1 for $\alpha = 10$, $\varepsilon_p = 1$ and ε = 0.999, 0.99 and 0.9. The simulations lead to:

51

$$h_{cm} - h_{cm0} \propto (N-1)^{-\beta_2}$$ (37)

with $\beta_2 = 1.01 \pm 0.02$, i. e. within our accuracy $\beta_1 = \beta_2 = 1$. Therefore, both the N and the ε dependence have the same exponent. We introduce the parameter X by setting:

$$X = (N-1)(1-\varepsilon) \quad \text{for } \varepsilon_p = 1$$ (38a)

and

$$X = N(1-\varepsilon) \quad \text{for } \varepsilon_p = \varepsilon .$$ (38b)

X seems to be the main variable of the problem as long as it is small. In Fig.18(a) we plot h_{cm}-h_{cm0} divided by $A_0^2 \omega^2 / g$ as a function of X found from 4000 realizations of the process using several parameter values. In the fluidized regime all data points fall on the same master curve. Fig.18(a) is plotted in a log-log scale to show the behavior of h_{cm}-h_{cm0}; at values $X < 0.1$ the master curve shows a slope of around -1. Using the points displayed, we obtain $F(N,\varepsilon) = F(X) = 4/(3X)$ for $F(N,\varepsilon)$ introduced in Eq.(35), so that the height of the cm for small X ($X < 0.1$) can be approximated through:

$$h_{cm}^{(0)} = h_{cm0} + \frac{4}{3} \frac{A_0^2 \omega^2}{g} \frac{1}{X} .$$ (39)

On the other hand for $X > 0.1$ the data follow a master curve only for $N \gg 1$ and high acceleration. On Fig.18(b) we fit the data obtained for $\alpha \geq 1000$, $N \geq 20$ and $\varepsilon \geq 0.8$ and thus extend the validity of Eq.(39) to the range $X \leq 2.8$, by setting:

$$h_{cm}^{(1)} = h_{cm0} + \frac{4}{3} \frac{A_0^2 \omega^2}{g} \frac{\varphi(X)}{X} ,$$ (40a)

with

$$\varphi(X) = 1 - a_1 X - a_2 X^2 .$$ (40b)

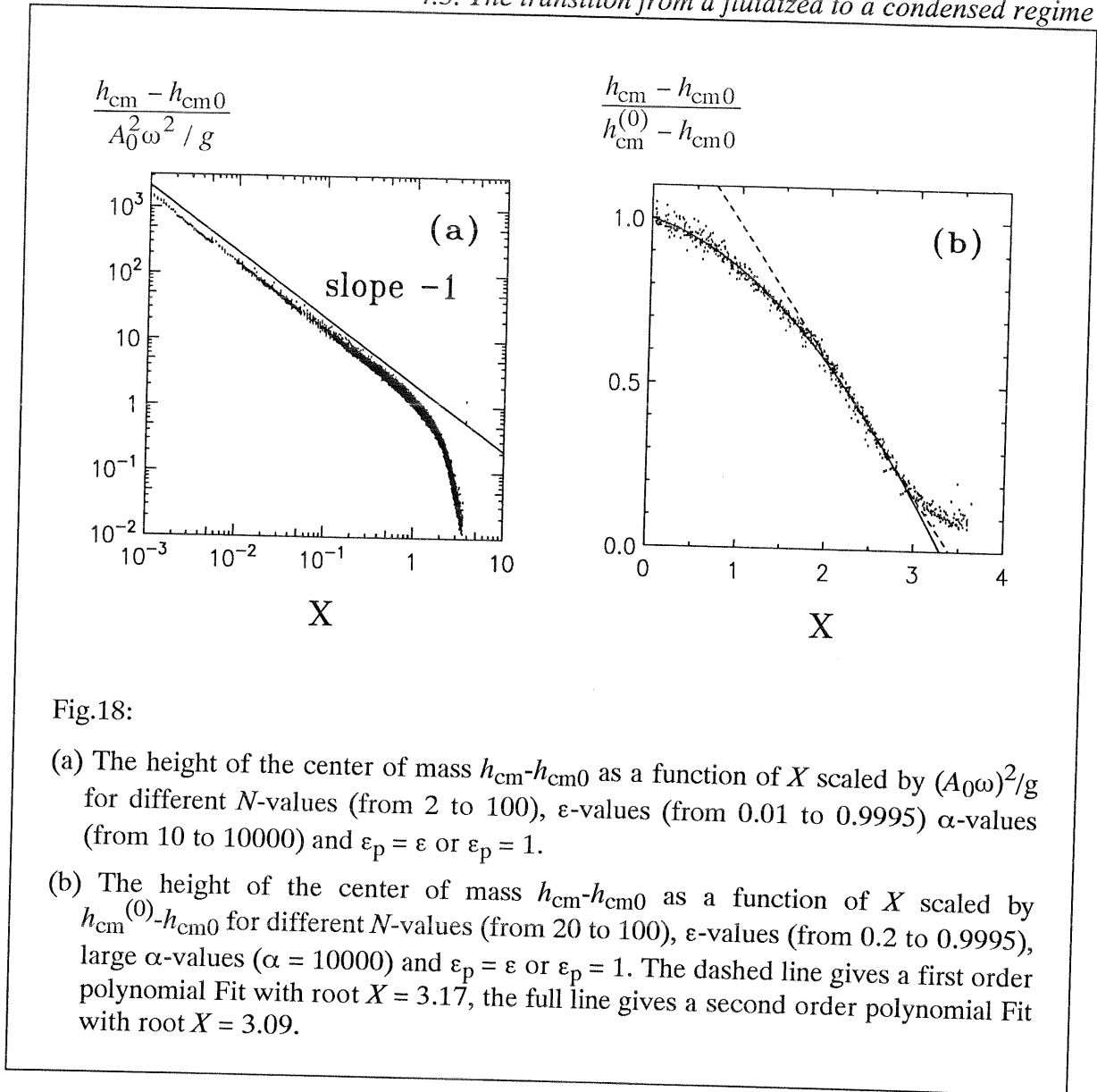where the constants are $a_1 = 0.098$ and $a_2 = 0.073$.

Fig.18:

(a) The height of the center of mass h_{cm}-h_{cm0} as a function of X scaled by $(A_0\omega)^2/g$ for different N-values (from 2 to 100), ε-values (from 0.01 to 0.9995) α-values (from 10 to 10000) and $\varepsilon_p = \varepsilon$ or $\varepsilon_p = 1$.

(b) The height of the center of mass h_{cm}-h_{cm0} as a function of X scaled by $h_{cm}^{(0)}$-h_{cm0} for different N-values (from 20 to 100), ε-values (from 0.2 to 0.9995), large α-values ($\alpha = 10000$) and $\varepsilon_p = \varepsilon$ or $\varepsilon_p = 1$. The dashed line gives a first order polynomial Fit with root $X = 3.17$, the full line gives a second order polynomial Fit with root $X = 3.09$.

This expression was obtained through a polynomial fit in the interval from 0 to 2.8. As can be seen from Fig.18(b), for $X > 2.8$ the curve changes from concave to convex. Eqs.(40a) and (40b) extrapolate to an intersection with the real axis at $X = X_c = 3.09$. A linear data fit plotted as a dashed line in Fig.18(b) and carried out in the interval from 2 to 2.8 leads to an intersection at $X = X_c = 3.17$. These findings suggest that in the absence of additional effects clusterization occurs around $X_c \cong 3.1$. Indeed for $X > X_c$ one never reaches a fluidized phase, regardless of the acceleration. On the other hand - in the intermediate region, i.e. for $2.5 < X < 4$, and for very large accelerations, α-values between 10^4 and 10^6, the simulations lead to the separation of the column into an array of beads condensed at the bottom and of several beads fluidized at the top. Thus for X above X_c the dissipation inside the column is so important, that no complete fluidization ever occurs and the lower part of the column stays condensed. This means that the motion of the lower

beads is always correlated . We can relate our X_c value to the work of Bernu and Mazighi [31], who find $X'_c = \pi$ for a column of balls colliding with a wall (see Appendix E). Note however, that the situation investigated by Bernu and Mazighi is different from ours: They monitor the dissipation of the *initial* internal energy; we have a steady influx of energy into the system. This difference may also be the reason why we obtain partially condensed states for $X > X'_c$.

In a way similar to the above we establish the scaling behavior of the dissipation time τ_D, obtaining:

$$\tau_D = \pi \frac{A_0 \omega}{g} \frac{\varphi'(X)}{X^\chi} \,, \tag{41a}$$

where

$$\varphi'(X) = 1 - a_3 X - a_4 X^2 \,. \tag{41b}$$

Again the data were fitted in the interval from 0 to 2.8; the values of the parameters are now $a_3 = 0.087$, $a_4 = 0.065$ and $\chi = 1.5$.

4.3.4. A crossover from the fluidized to the condensed phase

From Eq.(41) we infer a condition for fluidization in the range $X < X_c$. In the fluidized regime the time-scale of energy dissipation is much larger than one period. Thus we use $\tau_D f \gg 1$ as a criterion for fluidization. Translated in terms of the acceleration α this gives:

$$\alpha \gg \alpha_c \equiv 2 \frac{X^\chi}{\varphi'(X)} \,. \tag{42}$$

For $X \to 0$ we find $\alpha_c \to 0$; this seems to be a problem, since for $\alpha < 1$, a cluster that lies on the bottom plate, never lifts off. It is in a stable state, i.e. it moves together with the bottom plate. The transition from a cluster to a fluidized or condensed column of beads is only possible for $\alpha > 1$. Eq.(42) has to be understood as a condition for the stability of the dilute regime. For $\alpha \gg \alpha_c$ a system with non-zero initial energy stays in the dilute state. For $\alpha < \alpha_c \leq 1$ the system tends towards the situation of a cluster, moving together with the bottom plate.

In Fig.19 we plot the α-X parameter-space and display α_c as a function of X (straight line). We have three regimes: In regime (1), for $\alpha \gg \alpha_c$, the column is fluidized whereas in regime (2) for large α-values a fluidized phase (at the top) coexists with a
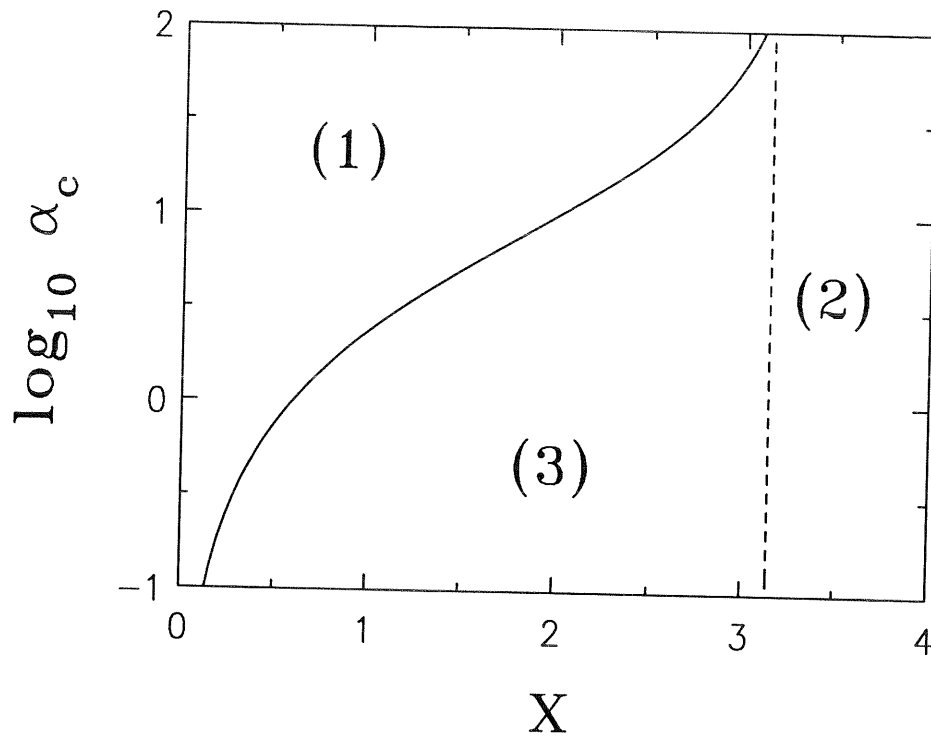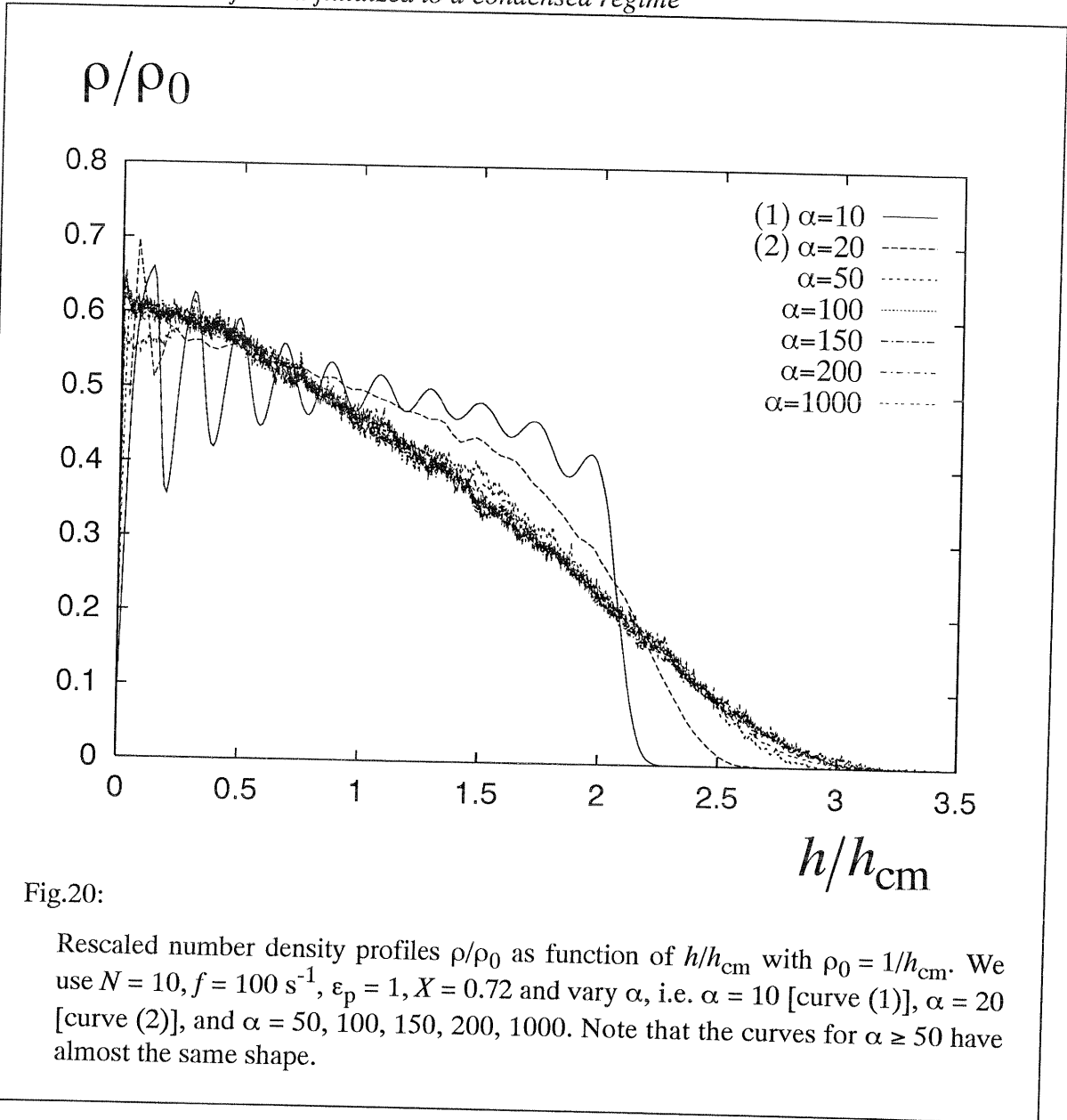
Fig.19:

Phase diagramm in the α-X-plane. $\log_{10} \alpha_c$, Eq.(42), is plotted as a function of X. In regime (1), for $\alpha \gg \alpha_c$, the system is fluidized and the shape of the density profile depends on X. In regime (2) no overall fluidization is possible, i.e. $X > X_c$, and in regime (3) the column of beads is condensed and the shape of the density profile depends on both α and X.

condensed phase (at the bottom) phase. For small α-values, i.e. $\alpha < \alpha_c$ and in regime (3) all beads are condensed or clustered. Fluidized here means the uncorrelated motion of the beads, a condition which does not neccessarily lead to a Boltzmann like density profile of exponential shape.

Varying α from large, i.e. $\alpha \gg \alpha_c$, to small values, i.e. $\alpha \ll \alpha_c$, corresponds to a transition from the fluidized to the condensed regime. In Fig.20 we plot the normalized number density profiles for $N = 10$, $f = 100$ s^{-1}, $\varepsilon_p = 1$, $X = 0.72$, i.e. $\varepsilon = 0.92$, and α in the range $10 < \alpha < 1000$. The shape of the density profile does not change for $\alpha \geq 50$ - the system is fluidized. For $\alpha < 50$ a transition from the fluidized to the condensed regime takes place, i.e. the shape of the density profile depends on α. Decreasing α, and thus decreasing the amplitude of the bottom plate, obviously decreases the height of the center of mass h_{cm}. With decreasing h_{cm} the condensed part of the column extends from the bottom to the top. The condensed regime shows up with clear peaks for each bead.

On the other hand, varying X from small to large values also leads to a transition

Fig.20:

Rescaled number density profiles ρ/ρ_0 as function of h/h_{cm} with $\rho_0 = 1/h_{cm}$. We use $N = 10$, $f = 100$ s^{-1}, $\varepsilon_p = 1$, $X = 0.72$ and vary α, i.e. $\alpha = 10$ [curve (1)], $\alpha = 20$ [curve (2)], and $\alpha = 50, 100, 150, 200, 1000$. Note that the curves for $\alpha \geq 50$ have almost the same shape.

from the fluidized regime to the condensed regime. In Figs.21 we plot the number density as a function of the height for simulations with $N = 20$, $\alpha = 10000$, $f = 10000$ s^{-1} and $\varepsilon_p = 1$. We vary ε in the range $0.99 > \varepsilon > 0.8$, such that $0.19 < X < 3.8$. In Figs.21(a-f) we find a continuous transition from a dilute to a dense regime for increasing X. In detail, the shape of the density profile changes from almost exponential [Fig.21(a)] to linearly decreasing (two slopes) [Fig.21(b)]. For intermediate X-values an almost constant density shows up [Figs.21(c) and (d)], whereas for large X-values condensed beads at the bottom coexist with fluidized beads at the top [Figs.21(e) and (f)]. Due to the large α-values used here, i.e. $\alpha \gg \alpha_c$, we never find a completely condensed regime.

Note that in Figs.20 and 21 the shape of the density profile changes with the X-value, not with the α-value, as long as $\alpha \gg \alpha_c$. For $X = 0.72$ [Fig.21] the density profile is
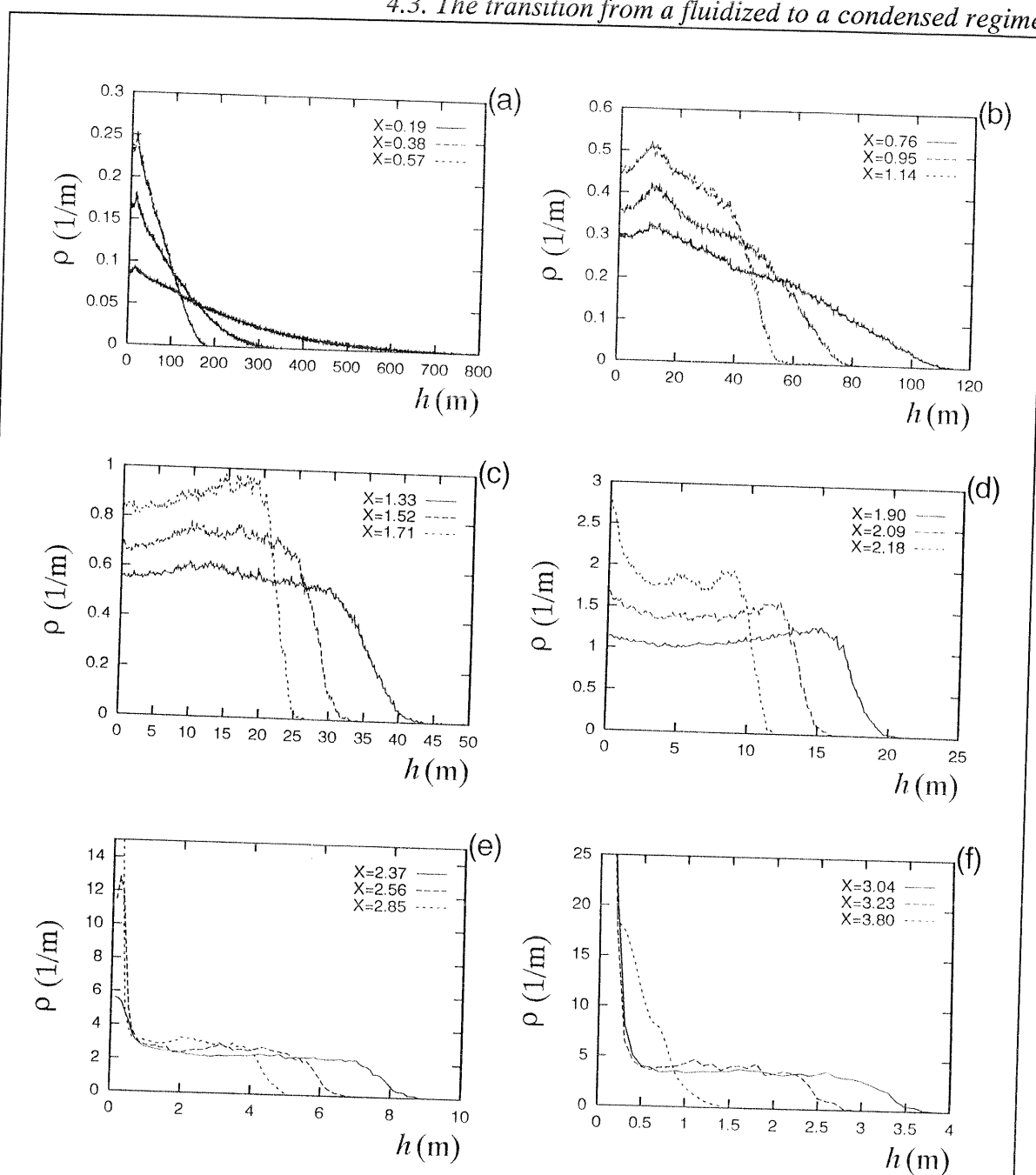
Fig.21:

Number density profiles ρ as a function of the height h for $N = 20$, $\alpha = 10000$, $f = 10000$ s^{-1}, $\varepsilon_p = 1$ and varying $1 - \varepsilon = X/(N-1)$. The X-values are inserted in the plots; note the different axes.

not of exponential shape. This means that the parameter X characterizes the shape of the density profile, a fact, which is well corrobarated by additional simulations.

4.4. The weakly dissipative regime (steel beads)

In this subsection we investigate the behavior of a column of steel beads undergoing vibrations in the gravitational field using both simulations and experiments. We let the bottom plate vibrate according to Eq.(7). We know from previous subsections that the particles are fluidized for sufficiently large agitation. We present experimental results which are reproduced by both ED and MD simulations.

4.4.1. A comparison of ED simulations with experiments

The following experiments were performed using steel beads. First we measured the value of the restitution coefficient, by determining the height of rebound for a bead dropped from a height of one meter on a smooth block of the same material. In this way we found $\varepsilon = 0.90 \pm 0.05$.

With the help of a video-camera connected to an image processing device, we accumulated images of the light dots formed at the center of the beads by a remote light source. The results permit experimental access to the density profile of the column of beads. From such profiles we extract the height of the center of mass h_{cm} (here a diameter-dependent quantity). We compare these data to the corresponding computer simulations; the best fits to all our experimental data are obtained for $\varepsilon = 0.92 \pm 0.01$, while we take $\varepsilon_p = 1$. The data obtained in three experimental runs with steel beads are presented in Figs.22(a-e); the curves show h_{cm} as a function of α and N. The first set of data is displayed in Figs.22(a) and (b) where the frequency was set at $f = 16.5$ s^{-1} and at $f = 15$ s^{-1}, while the amplitude A_0 was varied. The second set of experiments was performed at amplitudes $A_0 = 3.42$mm and $A_0 = 1.96$mm, while the frequency was varied [see Figs.22(c) and (d)]. In the third set of experiments we kept the amplitude $A_0 = 2.98$mm and the frequency $f = 15$ s^{-1} constant and we varied the number of beads N; the results are shown in Fig.22(e). In all these figures we plot the simulation results as small squares, the experimental data as circles and the limiting scaling laws for the fluidized regime as continuous curves; see Eq.(40). We are now in the intermediate α-regime, in which the simulations exhibit a complicated resonant behavior as discussed in the previous subsection. The scaling predictions of the fluidized phase agree quite well with the experimental results. Although not all theoretical details are reproduced: Thus the wiggly structure does not appear, possibly due to disturbances induced by the friction with the walls, a fact which may destabilize the organization of the column and therefore cause a disordered regime to occur more rapidly.
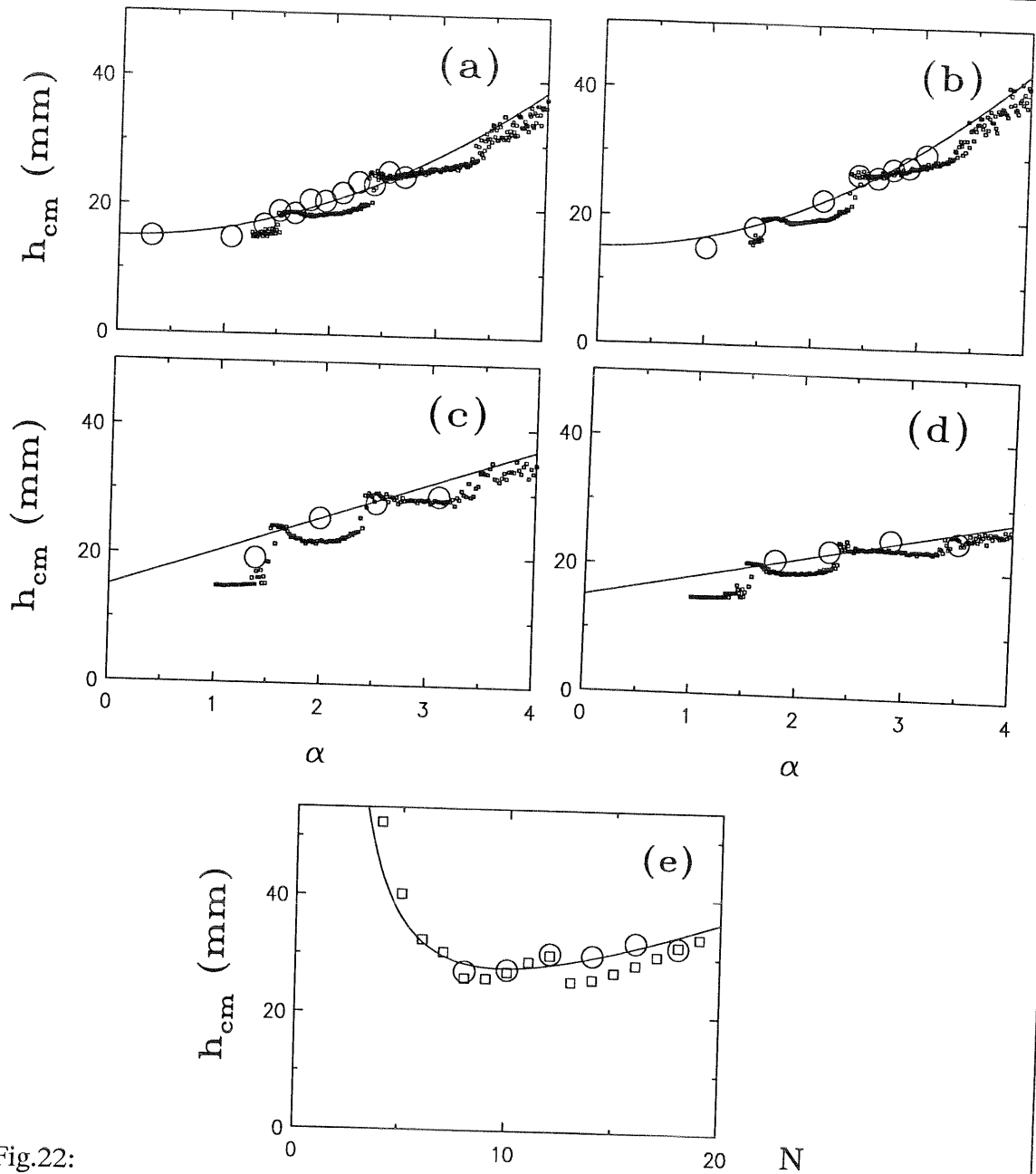
Fig.22:

(a) Experimental (circles), simulation (dots) and fit (full line) results for the height of the center of mass h_{cm} of $N = 10$ beads (here diameter dependent with $d = 3$ mm) as a function of α. The frequency is $f = 16.5$ s^{-1} and the restitution coefficients are $\varepsilon = 0.92$ and $\varepsilon_p = 1$.

(b) The same results as in Fig.22(a) but the frequency is here $f = 15$ s^{-1}.

(c) The same results as in Fig.22(a) but here we varied the frequency and held the amplitude constant $A_0 = 3.42$ mm.

(d) The same results as in Fig.22(c) but the amplitude is here $A_0 = 1.97$mm.

(e) The same results as in Fig.22(a) with $A_0 = 2.98$mm, $f = 15$ s^{-1} and $N = 8$, 10, 12, 14, 16 and 18. The simulations are here depicted by squares.
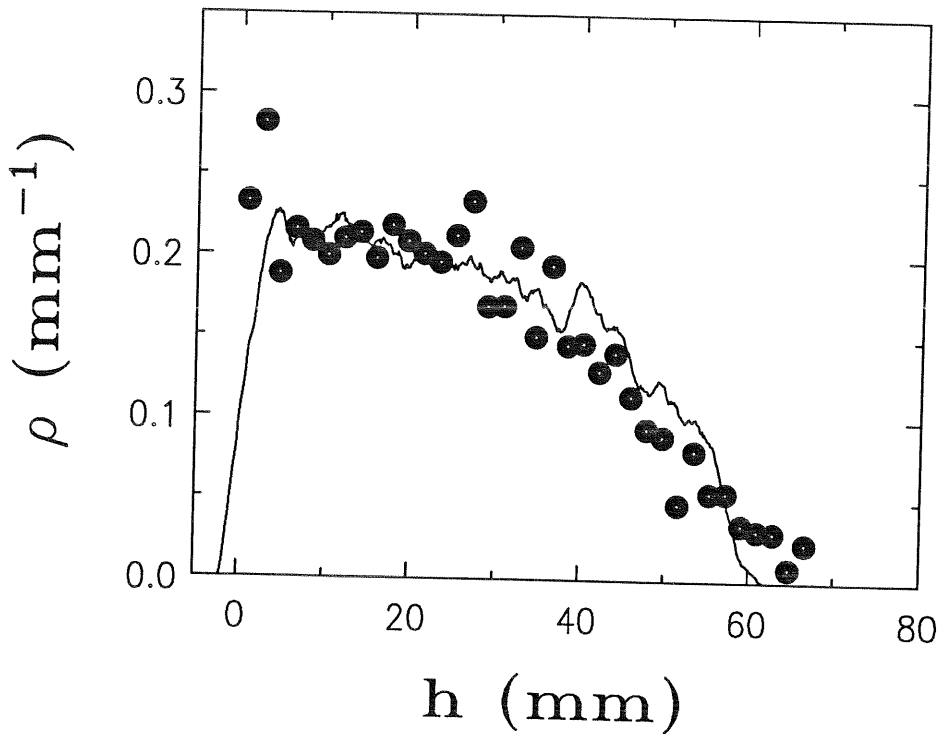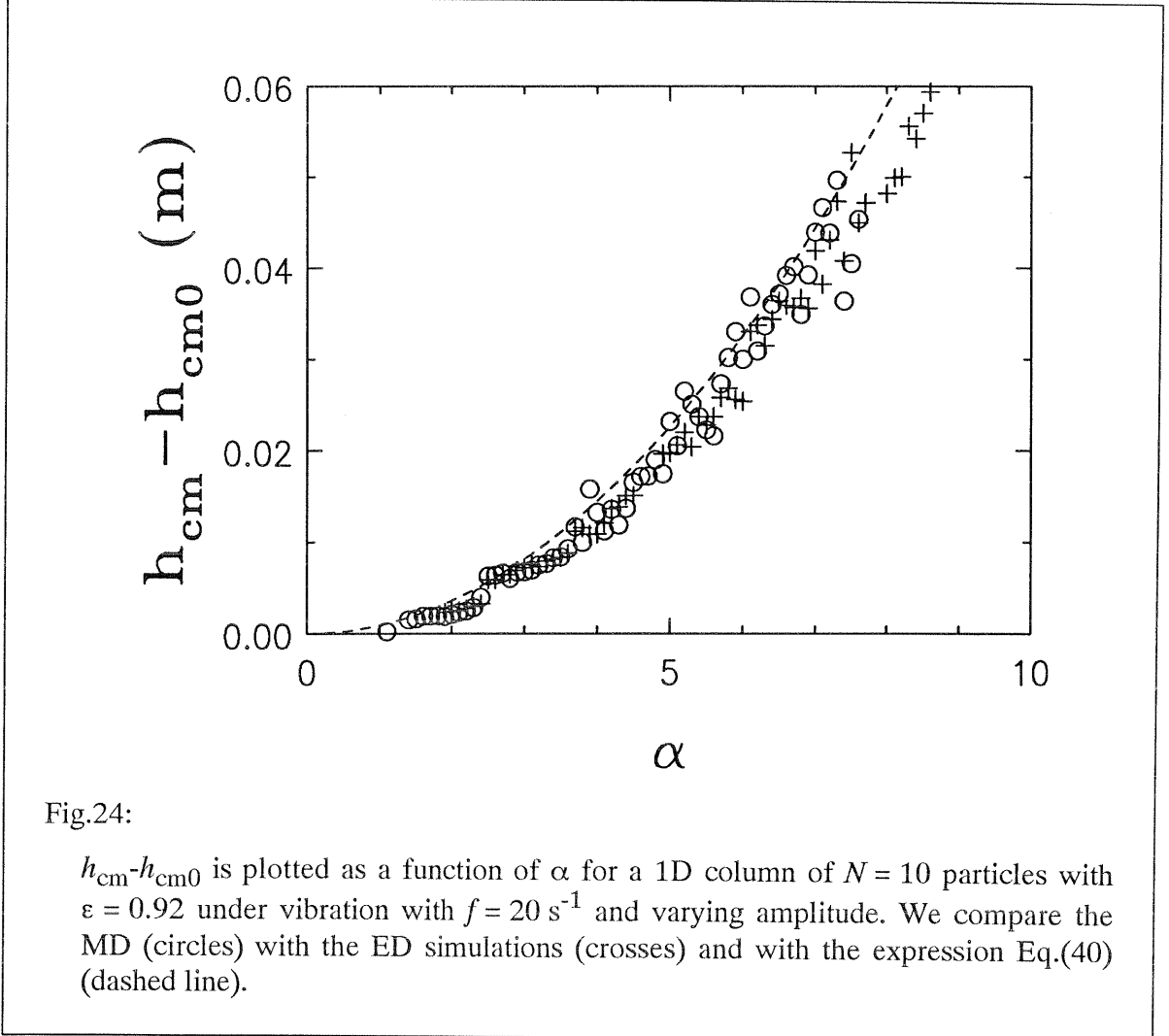
Fig.23:

The number density ρ as a function of the height h; compared are experiment (circles) and simulation (line) for $N = 10$, $f = 21$ s^{-1}, $A_0 = 1.97$ mm, $\varepsilon = 0.92$ and $\varepsilon_p = 1$.

In Fig.23 we compare the experimental density profile (here $N = 10$, $A_0 = 2$ mm and $f = 21$ s^{-1}) with the simulation results in the fluidized regime for $\varepsilon = 0.92$; we find that the overall agreement is fair. Hence the experimental data can indeed be understood from simulations, in which a single parameter (namely $\varepsilon = 0.92$) is entered.

4.4.2. A comparison of ED and MD simulations

We now turn to MD simulations of systems under strong agitation. In subsection 4.3.3 a scaling behavior for the center of mass h_{cm} was found from ED simulations in the case of high agitation α, low dissipation $(1-\varepsilon) \ll 1$ and a large number of particles N, i.e. $X = N(1-\varepsilon) < 2.8$, see Eqs.(40a) and (40b). We call this regime in the following the high energy and low dissipation regime (HLR). In Fig.23 we display results of ED and MD simulations of $N = 10$ particles with $\varepsilon = 0.92$ and $f = 20$ s^{-1}. In Fig.23 the crosses denote the

ED and the circles denote the MD results. Furthermore, we compare the results with Eq.(40), depicted as a dashed line. We average h_{cm} over more than 100 periods and set $t_c = 10^{-4}$ s, in the MD simulations. As a result we find that the ED and MD methods lead to similar results.

Fig.24:

h_{cm}-h_{cm0} is plotted as a function of α for a 1D column of $N = 10$ particles with $\varepsilon = 0.92$ under vibration with $f = 20$ s^{-1} and varying amplitude. We compare the MD (circles) with the ED simulations (crosses) and with the expression Eq.(40) (dashed line).

In Fig.25 we plot h_{cm} as a function of X obtained from simulations with different numbers of particles N and with $\varepsilon = 0.92$, $f = 20$ s^{-1} and $\alpha = 10$. In Fig.26 we plot h_{cm} as a function of X, but here we vary ε and use $N = 10$, $f = 20$ s^{-1} and $\alpha = 10$. The contact time for the MD simulations is $t_c = 4 \times 10^{-5}$s. The simulation results, MD (circles) as well as ED (crosses) deviate from the fit (dashed line) for $X > 2.4$. This is due to the fact, that $\alpha = 10$ is too small to fluidify the column for this high effective dissipation; thus the system is not in the HLR and thus Eq.(40) is not valid for $X > 2.4$ and $\alpha = 10$.

Discrepancies between MD and ED simulations become apparent when the

dissipation (or the number of dissipative contacts) becomes high and/or the acceleration α becomes low. In contrast, the results of ED and MD simulations agree well in the HLR, where we have large separations s_0 and a long time of free flight s_0/v_0 between the collisions. The conclusion is that we can choose quite long contact times as long as the condition $\sigma \gg 1$ is fullfilled.

The computer time needed for event-driven algorithms is proportional to the number of events; ED algorithms are therefore most effective in HLR. MD algorithms consume computer time proportionally to the simulated time and are therefore less effective in HLR. On the other hand, the detachment effect will be strongest in the low-energy high-dissipation regime. The particles are almost always in contact here. In this regime, where $\sigma < 1$, we have to choose the contact times as well as the interaction models carefully.

Fig.25:

We plot h_{cm}-h_{cm0} as a function of X; we vary N, such that $6 \le N \le 36$, and use $\varepsilon = 0.92$, $f = 20$ s^{-1} and $\alpha = 10$. We compare MD (circles) with event-driven simulations (crosses) and a high agitation fit (dashed line) Eq.(40).
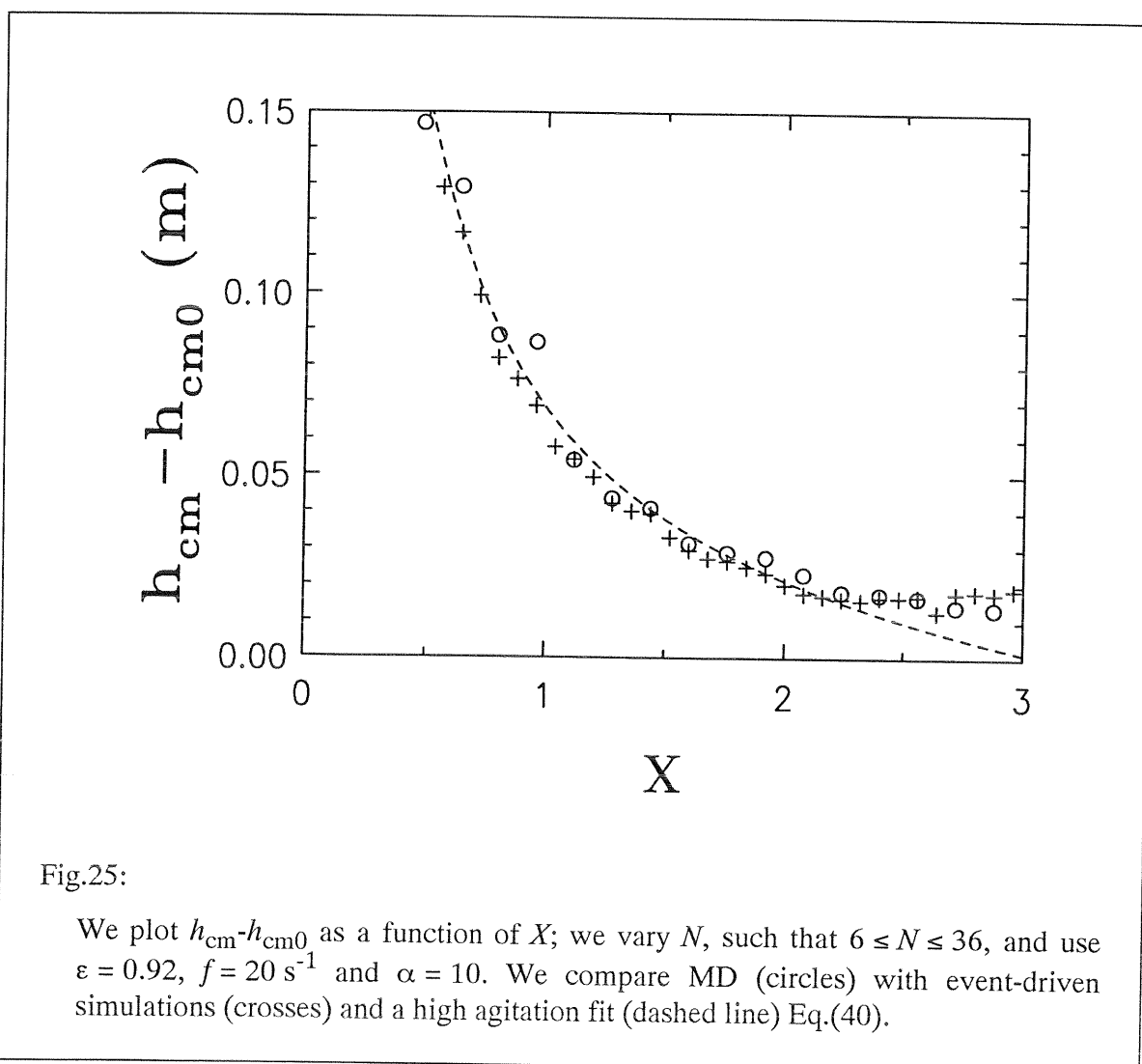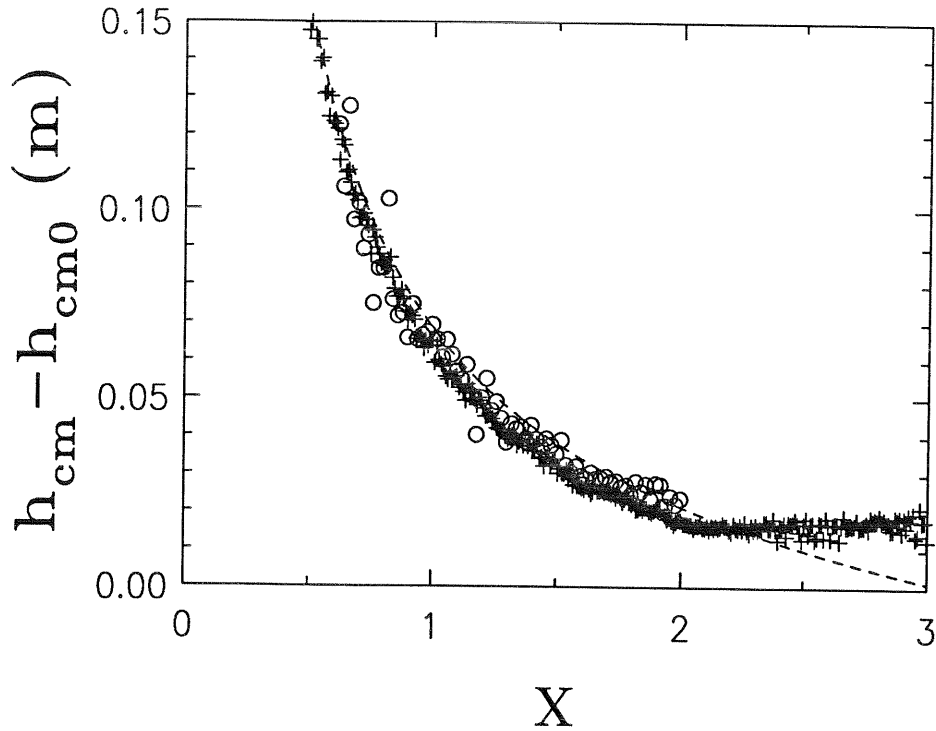
Fig.26:

We plot $h_{cm}-h_{cm0}$ as a function of X; we vary ε such that $0.7 \leq \varepsilon \leq 0.95$ and use $N = 10$, $f = 20\ \mathrm{s}^{-1}$ and $\alpha = 10$. We compare MD (circles) with event-driven simulations (crosses) and a high agitation fit (dashed line), i.e. Eq.(40).

4.5. The strongly dissipative regime (aluminum beads)

We look for the behavior of a column of aluminum beads undergoing vibrations in the gravitational field. The aim is to find out under which conditions MD and ED results are comparable and when deviations in the computed macroscopic properties occur. We also present experimental results; these are reproduced more effectively by ED than by MD simulations.
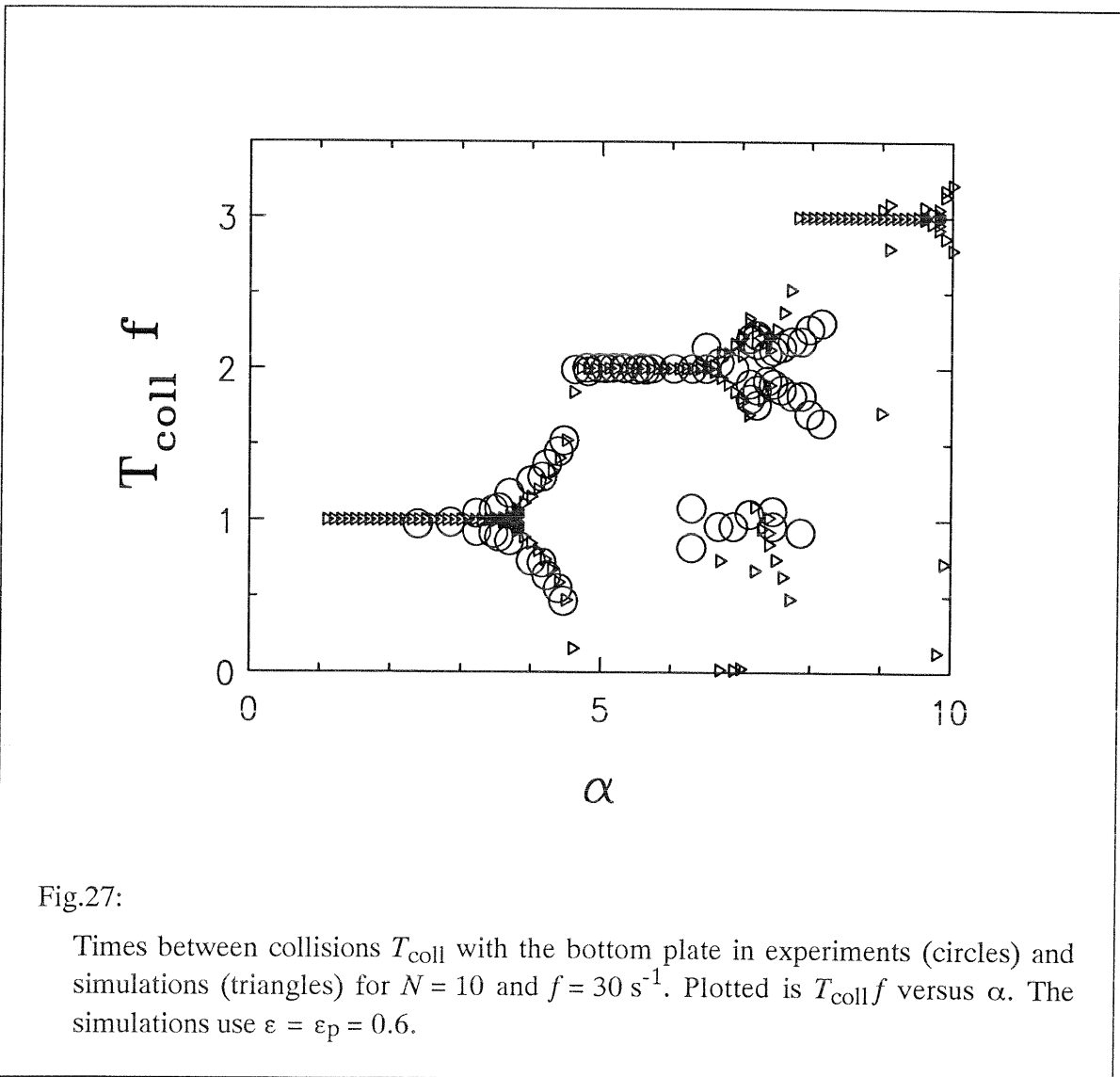
4.5.1. Comparison with experiments

We report two experiments with aluminum beads. The restitution coefficient for

aluminum beads was experimentally measured to be $\varepsilon = 0.60 \pm 0.05$. Again the column consists of $N = 10$ beads with a diameter of $d = 3$ mm. The behavior of the column of beads is vastly different from what we found for steel beads; in fact the column behaves as a condensed/clustered block. If microfluctuations exist in the positions, they occur at a scale much smaller than the size of the beads.

In the first experiment, we found it convenient to measure the time between two collisions of this block with the bottom plate; we denote this time by T_{coll}. The time T_{coll} is determined as a function of the normalized acceleration α, by recording the sound created by the heap when colliding with the bottom plate. In Fig.27 we plot the experimental findings and the results of two numerical simulations for $N = 10$, $\varepsilon = \varepsilon_p = 0.6$ and for $N = 1$,

Fig.27:

Times between collisions T_{coll} with the bottom plate in experiments (circles) and simulations (triangles) for $N = 10$ and $f = 30$ s^{-1}. Plotted is $T_{coll}f$ versus α. The simulations use $\varepsilon = \varepsilon_p = 0.6$.

$\varepsilon_p = 0$ on the same diagram. The simulation results for these two cases virtually coincide in the range displayed in the figure, and hence only lead to one curve (denoted by triangles). The curve for $N = 1$ and $\varepsilon = 0$ can be also achieved by using the iterative scheme [Eq.(30)] for the motion of one completely inelastic particle.

We recall that in the one-bead problem a series of bifurcations occurs [68,69], which involve a set of fundamental modes that are multiples of the lowest fundamental period $T = 1/f$. Our experimental findings with aluminum beads, given in Fig.27, parallel this picture in that the experiments clearly display the first two bifurcations, whose onset nicely mirrors the simulation results. To what extent the bifurcation cascade can be monitored is an interesting, still open, question since even in a dissipative one-ball system fully-developed chaos should not show up [79].

The second experiment is monitored by a camera that *moves horizontally* at a regular pace in front of the vibrating cell. The display is lighted using a stroboscopic flashing light tuned to a frequency slightly different from the excitation frequency. In this way, we obtain a (false) slowing down impression. An image processing device hooked up to the camera records and accumulates the traces of the beads' centers of mass. One thus observes the positions of the beads as a function of the phase of the excitation. On Fig.28(a) we show such a picture for an acceleration of $\alpha = 2$ and a frequency of $f = 10\ s^{-1}$. The column appears to stay clustered in all cases considered by us. On Fig.28(b) we present a MD simulation for the trajectory of the centers of mass of the beads for $N = 10$, $\varepsilon = 0.6$, and linear interaction-laws ($\beta = \gamma = 0$). On Figs.28(c) and (d) we present MD simulations with non-linear interaction laws, $\beta = 1/2$, $\gamma = 0$ [Fig.28(c)] and $\beta = \gamma = 1/2$ [Fig.28(d)]. The MD calculations for linear as well as non-linear interaction laws may lead to large separations in the positions of the beads. On the other hand an ED algorithm leads to clustered dynamics for the above parameters and thus reproduces the experimental results. Comparing Figs.28(b-d), we find a decreasing amplitude in the separations and also the pattern (Separation-Clustering) is no longer strictly periodic in the nonlinear case [Figs.28(c,d)]. The reason for the small separation in Fig.28(d) is the dependence of the dissipation on the velocity of contact (see Appendix C). The dissipation is small for small velocities and thus the non-linear particles loose less relative energy during a collision than linear particles. Since the relative energy is rather large σ is also large. Thus the separation is rather large after a collision of a column with the bottom plate and so the detachment effect appears to be less dramatic.

(a)

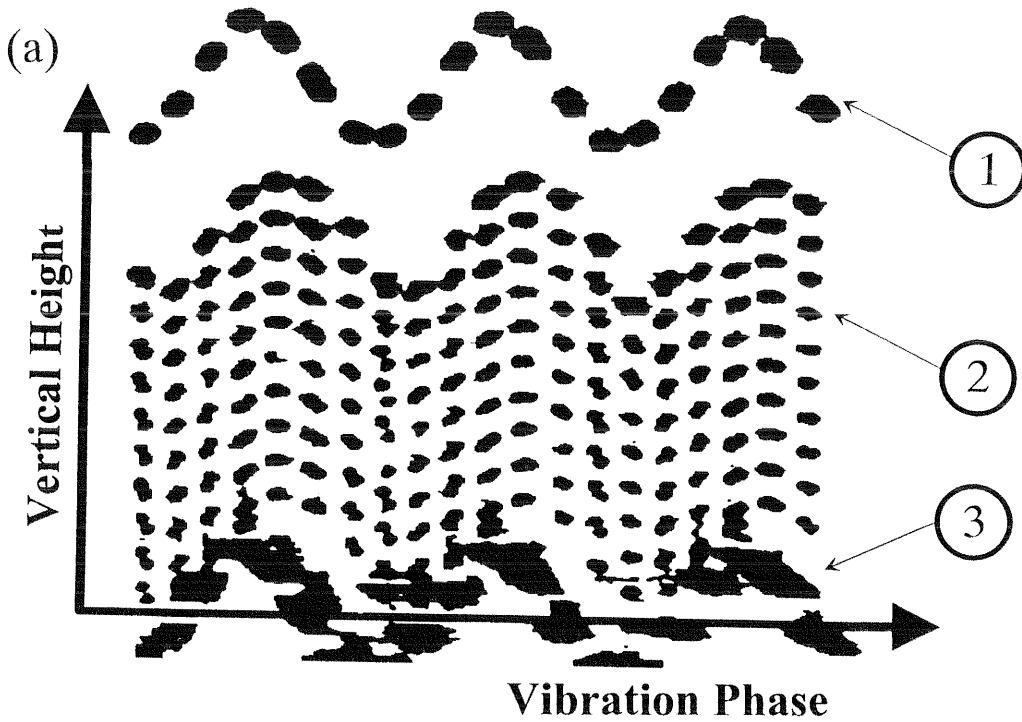**Vertical Height** (vertical axis label)

Vibration Phase

Fig.28

(a) Experimental result of a 1D column of $N = 10$ aluminum beads under vibration with $f = 10$ s^{-1}, and $\alpha = 2$. Plotted is the vertical position as a function of the vibration phase. (1) indicates the position of a reference bead, glued some fourteen bead diameters above the bottom plate. (2) indicates the position of the center of mass (dark dot) of the seventh bead. (3) indicates the bottom plate.

(b) Trajectiories of $N = 10$ particles as a function of time obtained from a MD simulation with $f = 10$ s^{-1}, $\alpha = 2$, $\varepsilon = 0.6$, $t_c = 3.6 \times 10^{-6}$s and the interaction laws are linear, i.e. $\beta = \gamma = 0$.

(c) Results of a MD simulation under the same conditions as in (b). The parameters used are $\beta = 1/2$, $\gamma = 0$, $K/m_{red} = 6.6 \times 10^{14}$ s^{-2}m$^{-1/2}$ and $D_n = 4 \times 10^4$ s^{-1}. This leads to $\varepsilon = 0.6$ and $t_c = 10^{-5}$s for an initial velocity of $v_0 = 0.66$ ms^{-1}.

(d) Results of a MD simulation under the same conditions as in (b). The parameters used are $\beta = 1/2$, $\gamma = 1/2$, $K/m_{red} = 6.6 \times 10^{14}$ s^{-2}m$^{-1/2}$ and $D_n = 2.2 \times 10^5$ s^{-1}. This leads to $\varepsilon = 0.6$ and $t_c = 10^{-5}$s for an initial velocity of $v_0 = 0.66$ ms^{-1}.
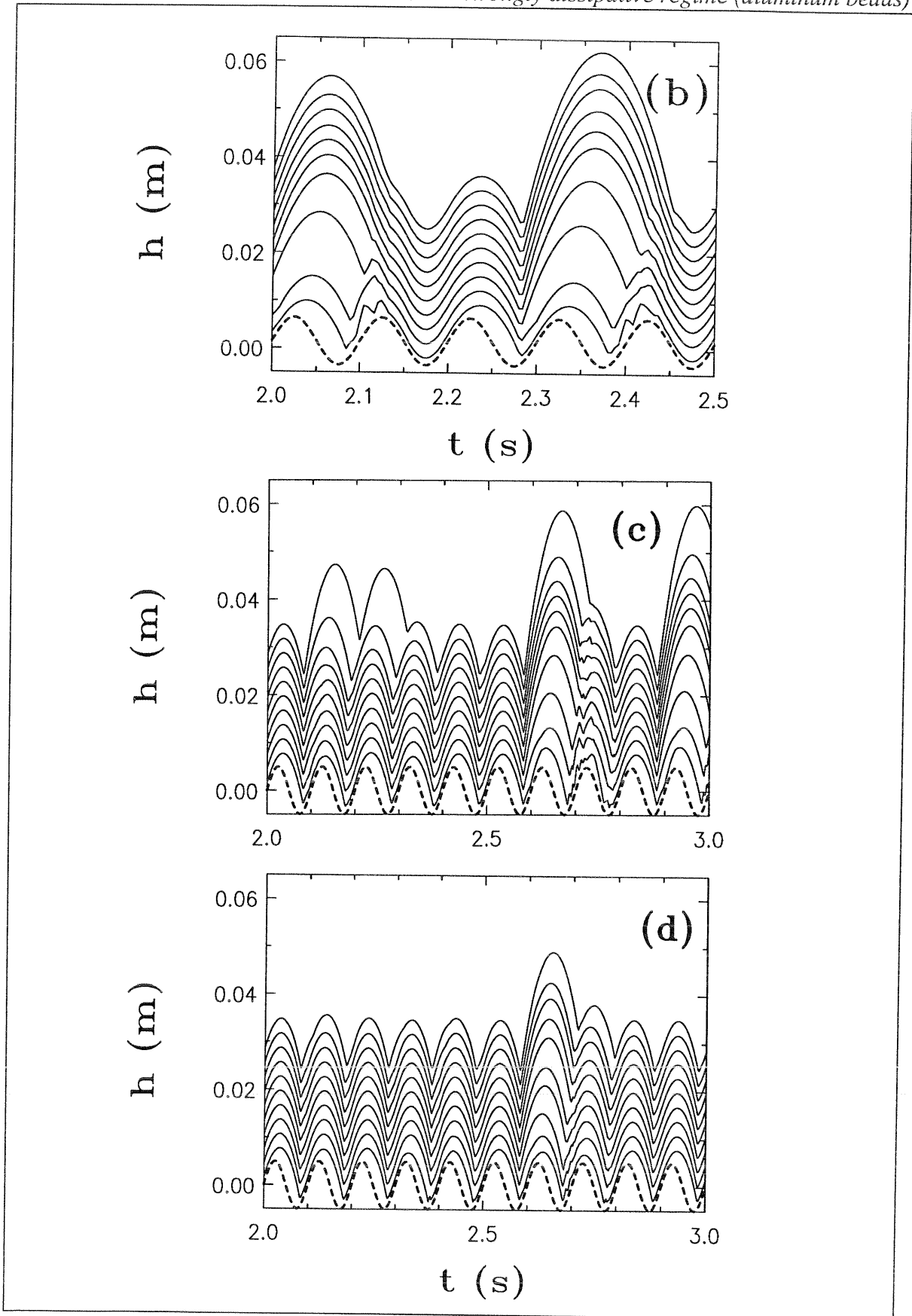
4.5.2. *The anomalous behavior of a vibrated column of beads*

In order to explain the large separations that show up in MD simulations [Fig.28] we present the MD trajectories of the centers of the beads calculated using $N = 10$ and $\varepsilon = 0.6$ in Fig.29. The bottom plate moves according to Eq.(7) with an amplitude of $A_0 = 1.24\,d$ and a frequency of $f = 20$ s^{-1}; this leads to a maximal acceleration of $2g$, i.e. $\alpha = 2$. The y-axis displays the reduced height according to Eq.(9). The value $\varepsilon \cong 0.6$ is typical for aluminum beads. From previous studies we know, both from experiments and from ED simulations [36,62], that such a collection of beads ($N = 10$, $\varepsilon = 0.6$) has a very low effective restitution coefficient ($\varepsilon_{eff} \cong 0$) and that the system forms a cluster whose behavior mirrors that of a very inelastic single bead [70]. The MD results were obtained for $t_c = 7 \times 10^{-4}$s, 7×10^{-5}s, 7×10^{-6}s, and 2×10^{-6}s. Note that large fluctuations occur in the inter-bead separations when t_c is large [Fig.29(a)]; this is due to the fact that the contact time of 10 particles with the bottom plate is roughly 15 percent of the period and is thus too large to decouple the collisions from the vibration. An additional reason for the large fluctuations is the ratio $\sigma = s_0 / (v_0 t_c)$ of the time between events to the contact time. For large t_c the value of σ becomes small and thus detachment (together with weak energy dissipation) is active. In Figs.29(c) and (d), where the contact time of the beads is much shorter than the excitation period, we observe a periodic pattern which alternates between condensed states, with almost zero relative energy, and states with large interbead separations due to large relative energies. In the condensed state we find very small separations, i.e. $\sigma \ll 1$, and therefore the detachment effect is active, which means that the next collision sequence occurs under very low energy loss. After this collision sequence the separations between beads become be large, i.e. $\sigma > 1$. Therefore in the next collision sequence much energy is lost, so that the separations again decrease. This periodic change from high to low σ values and back again is the reason for the pattern observed in Figs.29(c) and (d). Remember that for large t_c values σ stays small most of the time so that the system remains in a high-energy state, in which detachment as well as large fluctuations occur.
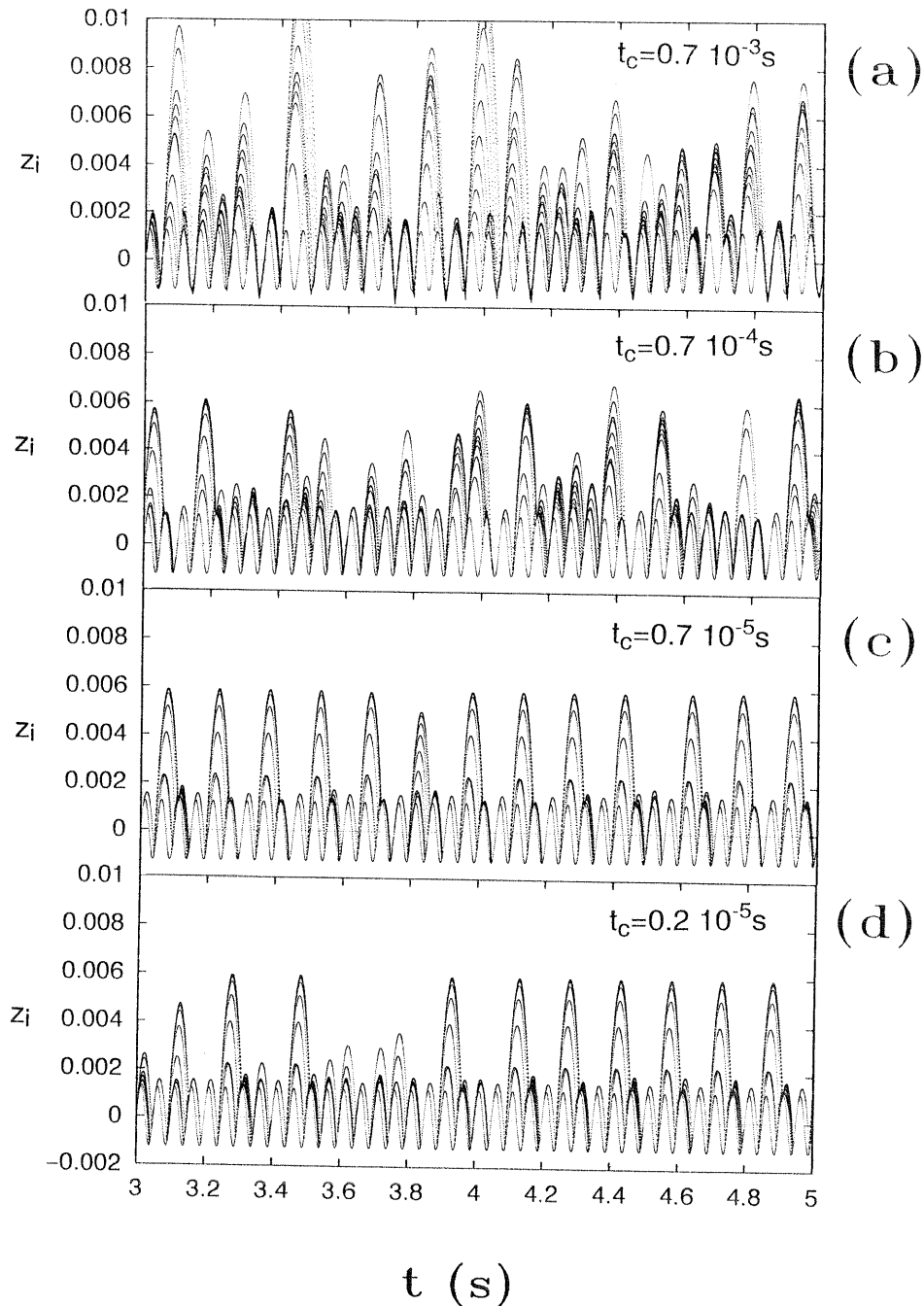
Fig.29:

The MD trajectories [reduced coordinates z_i Eq.(9)] of $N = 10$ beads with $\varepsilon = 0.6$ for $A_0 = 1.24\ d$ and $f = 20\ \text{s}^{-1}$ are plotted. The contact time values are inserted in Figs.29(a)-(d).

An ED algorithm as introduced in Refs.[36,62] shows completely different behavior in this parameter range. For $N = 10$ and $\varepsilon = 0.6$ the event-driven LRV-procedure leads to $\varepsilon_{\text{eff}} = 0$, i.e. the *inelastic collapse* [32,33]; in other words, the energy of collision is always

dissipated inside the column, so that the particles stay clustered. This leads to a pattern for the cm-trajectory similar to the one of a single, completely inelastic particle [70], i.e. the relative energy always vanishes for these parameters.

The relative energy E_{rel} ('granular temperature') is plotted in Fig.30 for some 20 periods of a MD simulation with $N = 10$, $\varepsilon = 0.6$, $f = 20$ s^{-1}, $\alpha = 2$ and $t_c = 0.7 \times 10^{-5}$s, i.e. the simulation shown in Fig.29(c). Plateaus in E_{rel} correspond to free flights of all beads; steps in E_{rel} correspond to collisions of particles and $E_{rel} = 0$ corresponds to a cluster of beads. If such a cluster, with $E_{rel} = 0$, denoted by the dotted line, hits the bottom plate, a peak in the relative energy appears, i.e. $E_{rel} \cong 0.02$. These peaks occur in Fig.30 at times $t = 0.64, 0.79, 0.94, 1.19$ and 1.34 and are denoted by a dashed line. The reason is that due to the detachment effect a certain amount of the initial kinetic energy is transferred to relative energy. However E_{rel} may get larger than these peaks which appear due to the detachment effect. E_{rel} may vanish again when due to a large number of dissipative collisions all relative energy is spent.
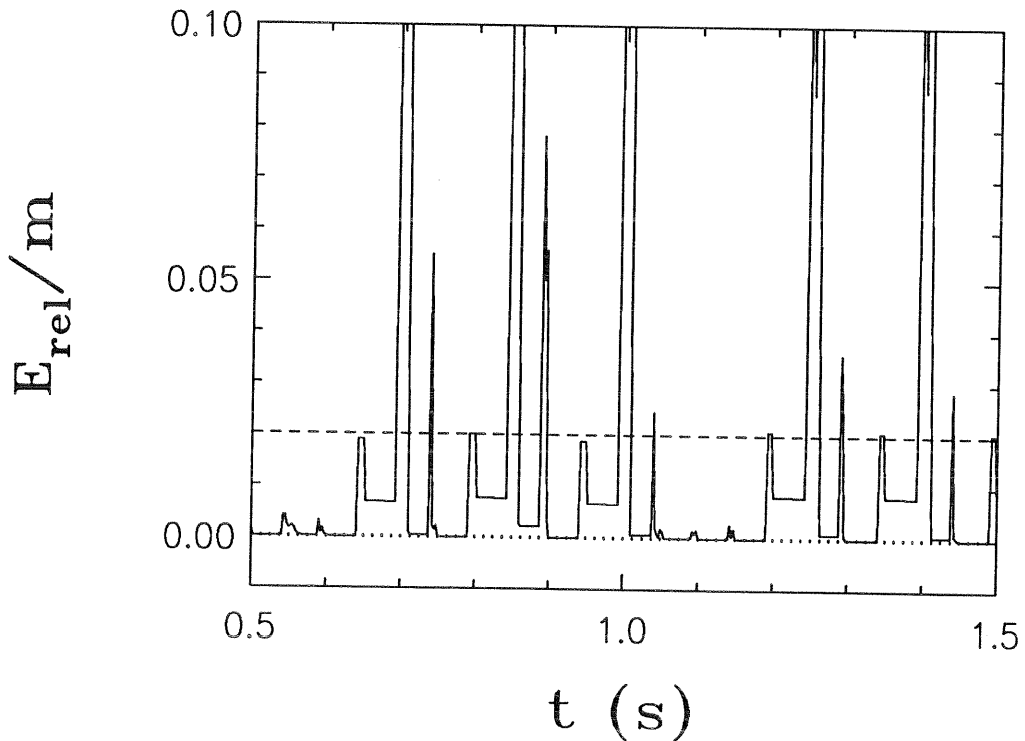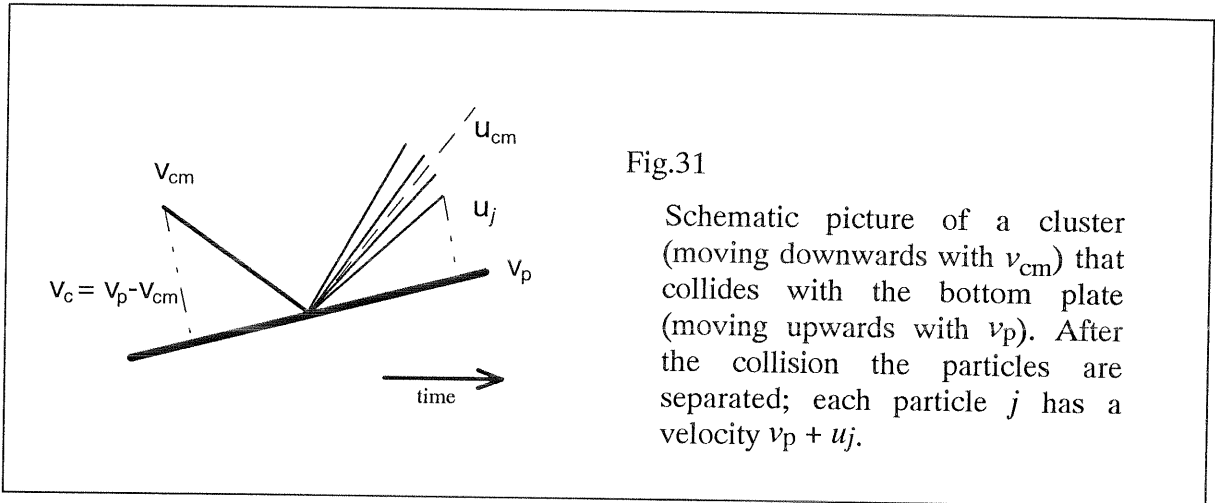

Fig.30:

The relative energy E_{rel} in units of the mass is plotted as a function of time for the parameters used in 29(c).

4.5.3. *The detachment effect in MD simulations of aluminum beads*

We now turn to a more quantitative description of the anomalous behavior, reported above [see Fig.30]. Assume N particles, each with mass m; we focus on the situation, where all relative energy is dissipated, i.e. the velocities of all particles in the cluster are equal, and the cluster lies on the bottom plate. The cluster moves together with the bottom plate until the acceleration becomes larger than g. We know from subsection 4.2. that this cluster lifts off from the bottom plate at the phase $\varphi_1 = \arcsin(1/\alpha)$. The phase φ_2, at which the cluster hits the bottom plate again is given by Eq.(30); the (positive) relative velocity $v_c = v_p - v_{cm}$ between bottom plate and cluster (v_{cm} is the velocity of the cluster in the system's frame of reference) at phase φ_2 is given by Eq.(31) [see Fig.12(b)]. We give a schematic picture of the situation in Fig.31

Fig.31

Schematic picture of a cluster (moving downwards with v_{cm}) that collides with the bottom plate (moving upwards with v_p). After the collision the particles are separated; each particle j has a velocity $v_p + u_j$.

Assuming $t_c \ll T$, i.e. the contact time is much smaller than the period of the bottom plate, we may turn to the reference frame of the bottom plate; for the sake of simplicity we also neglect the influence of gravity during such short time intervals. This situation, i.e. the collision of a cluster with a wall, was discussed in subsection 3.2. There the effective restitution coefficient ε_{eff} was defined as $\varepsilon_{eff} = \sqrt{E_f/E_0}$ where E_0 and E_f are the energies just before and just after the collision. This leads to an expression for E_f that includes only the parameters v_c and ε_{eff}:

$$E_f = \frac{m}{2} \sum_{j=1}^{N} u_j^2$$

$$= \varepsilon_{eff}^2 E_0$$

$$= \varepsilon_{eff}^2 \frac{Nm}{2} v_c^2 \quad , \tag{43}$$

where u_j is the velocity of particle j relative to the bottom plate. Evidently, u_j has two components, the velocity of the center of mass relative to the bottom plate $u_{cm} - v_p$ and the velocity relative to the center of mass $\Delta u_j = u_j - u_{cm} + v_p$. Separating u_j in Eq.(43) we get

$$E_f = \frac{m}{2} \sum_{j=1}^{N} \left(\Delta u_j + u_{cm} - v_p \right)^2 \tag{44}$$

$$= \frac{Nm}{2} \left(u_{cm} - v_p \right)^2 + \frac{m}{2} \sum_{j=1}^{N} \Delta u_j^2 \quad .$$

Note that the sum over the velocities relative to the center of mass vanishes, i.e. $\sum_{j=1}^{N} \Delta u_j = 0$. We derive the velocity of the center of mass, using the definition of the relative energy $E_{rel} = \frac{m}{2} \sum_{j=1}^{N} \Delta u_j^2$, from Eqs.(43) and (44):

$$u_{cm} = v_p + \sqrt{\varepsilon_{eff}^2 v_c^2 - \frac{2E_{rel}}{Nm}} \tag{45}$$

$$= v_p + \varepsilon_{eff} v_c \sqrt{1 - \frac{2E_{rel}}{Nm\varepsilon_{eff}^2 v_c^2}}$$

$$\cong v_p + \varepsilon_{eff} v_c (1 - \Phi/2) \quad ,$$

with $\Phi = E_{rel}/E_f \ll 1$. Thus the relative kinetic energy

$$E_{rel} = \Phi E_f \tag{46}$$

$$= \Phi \varepsilon_{eff}^2 E_0$$

$$= \Phi \frac{Nm}{2} v_c^2 \varepsilon_{eff}^2$$

of the cluster does not depend explicitly on the velocity of the bottom plate. This is so because v_c is a function of α, see Eq.(31); from the simulations, presented in subsection 3.2., the values of $\varepsilon_{eff}(N,\varepsilon)$ [Fig.7(b)] and $\Phi(N,\varepsilon)$ [Fig.7(c)] can be obtained. As an example we give $\varepsilon_{eff}(N=10, \varepsilon=0.6) = 0.89$ and $\Phi(N=10, \varepsilon=0.6) = 0.056$.

The kinetic energy of the column after the collision in the system's frame of reference is now

$$E_{\text{kin}} = \frac{m}{2} \sum_{j=1}^{N} \left(v_{\text{p}} + u_j \right)^2 \tag{47}$$

$$= \frac{m}{2} \sum_{j=1}^{N} \left(v_{\text{p}} + (u_{\text{cm}} - v_{\text{p}}) + \Delta u_j \right)^2$$

$$= \frac{Nm}{2} u_{\text{cm}}^2 + \frac{m}{2} \sum_{j=1}^{N} \Delta u_j^2$$

$$= E_{\text{cm}} + E_{\text{rel}} \ .$$

Inserting Eq.(45) in Eq.(47) and only calculating terms of order Φ we obtain

$$E_{\text{kin}} \cong \frac{Nm}{2} \left(v_{\text{p}} + \varepsilon_{\text{eff}} v_{\text{c}} \right)^2 - \frac{Nm}{2} \varepsilon_{\text{eff}} v_{\text{c}} v_{\text{p}} \Phi \ . \tag{48}$$

Eq.(48) is consistent with Eq.(13) in the limiting case of one particle, i.e. $N = 1$, $\Phi = 0$ and $\varepsilon_{\text{eff}} = \varepsilon$.

In Figs.32(a) we plot the kinetic energy in units of the mass, i.e. the first term of Eq.(48), and in Fig.32(b) we plot the relative energy in units of the mass, i.e. Eq.(46), as a function of the acceleration α. We present numerically calculated values (lines) as well as values extracted from MD simulations (circles). The parameters of the simulations are $N = 10$, $\varepsilon = 0.6$, $t_{\text{c}} = 7 \times 10^{-5}$ s and $f = 20$ s^{-1}. The numerical solution of Eqs.(46) and (48) was carried out using MAPLE V; for details see Appendix D1. The relative energy, obtained from Fig.30 for $\alpha = 2$ has to be compared with the value of $E_{\text{rel}}(\alpha=2)$ obtained from Fig.32(b); we find that both values coincide, i.e. $E_{\text{rel}}(\alpha=2)=0.02$.

The important consequence is that the periodic pattern we observed during MD simulations with rather short contact times [Figs.29(c) and (d)] and linear interactions does not vanish for smaller contact times. We were able to predict the relative energy E_{rel} with simple arguments and without using the contact time as a parameter. Thus the detachment effect is model dependent; moreover using physically correct material parameters (together with the corresponding contact time) does not stop the detachment effect. The detachment effect occurs for small σ-values and on the other hand could not be observed for large σ-values, i.e. $\sigma > 1$. Furthermore, the results of MD and ED simulations agree with experiments in 1D as long as $\sigma \gg 1$. In the following we will proceed to examine the detachment effect in 2D model systems. The question is if detachment appears in 2D under the same conditions as in 1D.
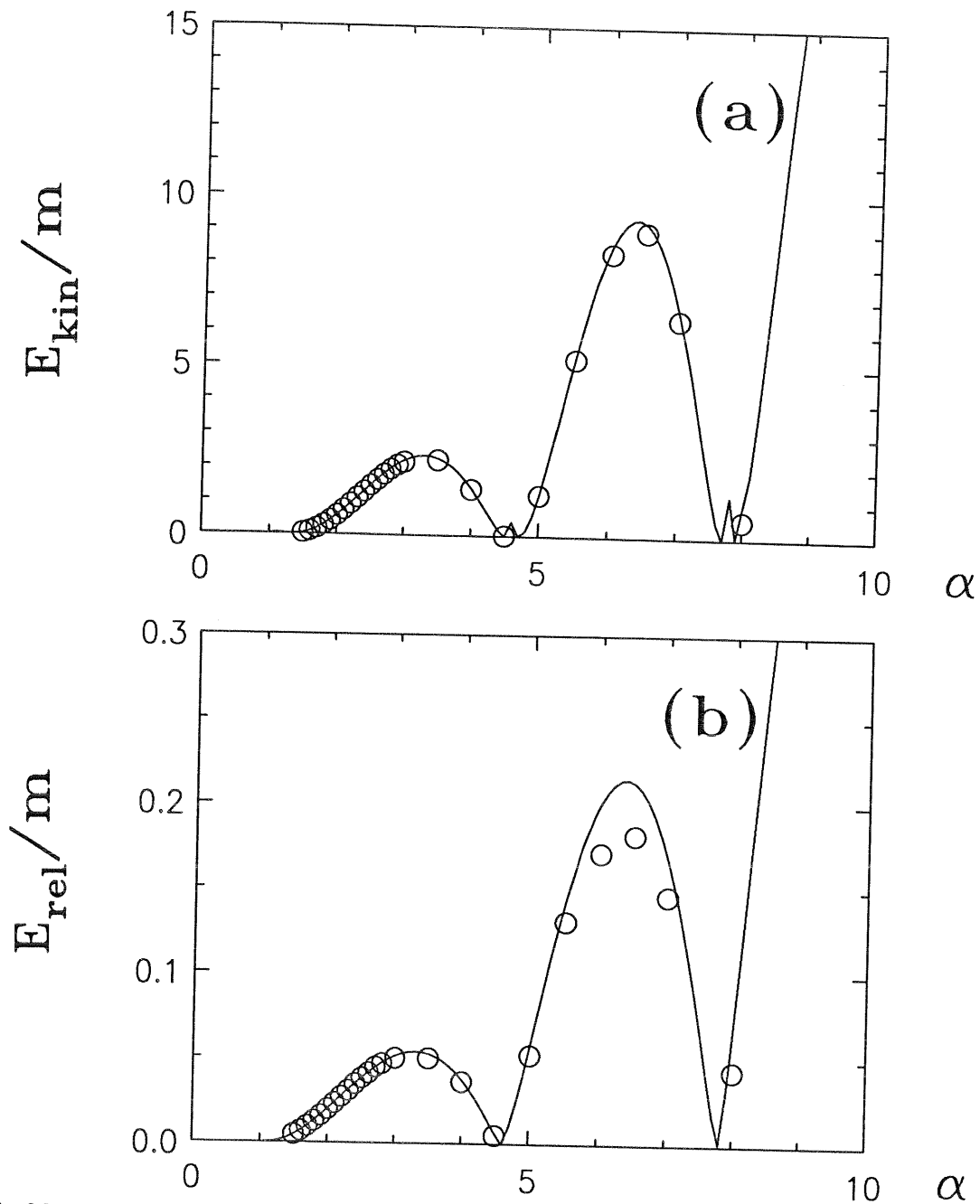
Fig.32:

(a) The kinetic energy E_{kin} of $N = 10$ particles with $\varepsilon = 0.6$ is plotted in units of the mass after a collision with the bottom plate at phase φ_2. Circles give data extracted from MD simulations; see text for details. The line gives the numerical solution of Eq.(48).

(b) The relative energy E_{rel} is plotted in units of the mass for the MD simulation of Fig.32(a). The line gives the numerical solution of Eq.(46).

5. Results of Simulations in 2D

In the following we will discuss the behavior of N particles of diameter d and restitution coefficient ε. First we let the particles fill a box of width L, where in their state of lowest energy they form a triangular lattice. The height of the center of mass of this arrangement is

$$h_{cm0} = \frac{n_b d}{2N}\left[(1 - \sqrt{3}/2)n_h + \sqrt{3}/2\, n_h^2\right] + \frac{n_o d}{2N}\left[1 + \sqrt{3}n_h\right] \; . \tag{49}$$

$n_b = L/d\text{-}1/2$ is the average number of beads per layer in the presence of walls (L/d for periodic boundary conditions). In Eq.(49) $n_h = \texttt{int}(N/n_b)$ is the number of full layers and $n_o = N\text{-}n_h n_b$ is the number of beads in the uppermost layer. For $N = 50$, $n_b = 12.5$ and $d = 10^{-3}$ m we find $n_h = 4$ and $n_o = 0$, which leads to $h_{cm0} = (d/2)\left[1 + 3\sqrt{3}/2\right] = 1.8 \times 10^{-3}$ m.

We now turn to the discussion of typical time scales in 2D systems. In Sec.3.1.2 the contact time was evaluated to be $t_c \approx 3 \times 10^{-6}$ s for the collision of two steel beads with diameter $d = 1$ mm (for details see Appendix C). At low dissipation and for the LSD-model t_c is proportional to $K^{-1/2}$, see Eq.(22), so that an increase of K by a factor of 100 decreases t_c by a factor of 10. Taking physically reasonable values for t_c leads to extremely high MD computing times. This is due to the fact that one has to insure that several time scales of the system are well-separated. Ideally one should have:

$$t_{MD} \; << \; t_c \; << \; T \; , \tag{50}$$

where t_{MD} denotes the time between the simulation steps, t_c is the contact time and $T = 1/f$ is the period of the vibration. The MD simulations reported here were done with $t_{MD} < t_c/40$, while T is in the range 0.0025 s $< T < 0.05$ s. For convenience we used t_c values in the range 2.2×10^{-5} s $< t_c < 7 \times 10^{-4}$ s, by choosing K accordingly, i.e. $t_c < T/100$. Here we let ourselves be lead by the model character of Eq.(19).

Another time variable to be aware of is the average time t_{ev} between collision events. One may approximate t_{ev} by $t_{ev} \approx l/\bar{v}$, where l is the mean free path. In 2D l is comparable to $(h_{cm}\text{-}h_{cm0})L/(Nd)$, where the quantities h_{cm} and h_{cm0} denote, as before, the

height of the cm and $\bar{v} = \left\langle v^2 \right\rangle^{1/2}$ is an average velocity. We now use the quotient

$$\sigma = t_{\mathrm{ev}}/t_{\mathrm{c}} = (h_{\mathrm{cm}} - h_{\mathrm{cm}0})L/(Nd\,t_{\mathrm{c}}\bar{v}) \ , \tag{51}$$

similar to the definition of σ in Sec.3.2.1. The value of σ is the ratio between the average time of free flight and the contact time t_{c}. For $\sigma \gg 1$ one almost exclusively finds that only pairs of particles collide. For $\sigma \ll 1$ the contact time t_{c} is larger than the average time between collisions. In other words, during the time t_{c} there is a high probability for a bead to interact with several others. In this case the use of the restitution coefficient ε used to describe the energy dissipation is questionable with ε only being defined for two-particle collisions only (see Sec.3.2). In several test runs we found the condition $\sigma \gg 1$ to render the MD results independent of t_{c}. For the calculations reported here we checked that $\sigma > 2$ always holds; in fact, in most cases we even have $\sigma > 5$.

Since we utilize both, MD and ED methods, we recall the connection between the parameters K and μ used in MD and the restitution coefficient ε used in ED simulations, see Eq.(23) in Sec.3.1.1.

In our simulations we have $d = 10^{-3}$ m, $K/m_{\mathrm{red}} = 2 \times 10^9 \mathrm{s}^{-2}$, $\mu = 2 \times 10^3 \mathrm{s}^{-1}$ as typical parameters. These parameters together with the above equations lead to $\varepsilon = 0.87$ and $t_{\mathrm{c}} = 7 \times 10^{-5}$s so that we use $t_{\mathrm{MD}} = 10^{-6}$s. The maximal penetration for these parameters is $x_{\mathrm{max}} = 2.1 \times 10^{-5}$m for $v_0 = 1 \mathrm{\,ms}^{-1}$, i.e. $x_{\mathrm{max}} = 0.02\,d$. The restitution coefficient ε is experimentally found to be only weakly velocity dependent; for velocities around $1 \mathrm{\,ms}^{-1}$ one finds $\varepsilon = 0.6$ for aluminum and $\varepsilon = 0.92$ for steel, see Sec.4. We note here that we are allowed to use the parameters given above only for systems in which all velocities remain smaller than $1 \mathrm{\,ms}^{-1}$. In systems in which larger velocities occur one has to decrease the contact time to a reasonable value.

5.1. Simulations in the fluidized regime

In subsection 4.3. scaling behavior was reported for the position of the center of mass of a 1D-column of beads undergoing external vibrations. The observation in 1D was that in the fluidized regime the height of the center of mass (h_{cm}) obeys Eq.(40). In the following we will present the corresponding scaling laws for 2D-arrays of beads.

5.1.1. Fluidization due to the vibrating bottom plate

In the following we will analyse the behavior of the height of the center of mass h_{cm}

as a function of the parameters A_0, f, N and ε. Before recording the data used in the averaging we let the bottom plate perform from 50 up to 1000 vibration cycles, in order to ascertain that the system is near its steady-state. The displacements, velocities, and energies are then determined by averaging over up to 4000 cycles.

Snapshots of the system with $N = 50$ and $\varepsilon = 0.9$ are plotted in Fig.33(a) for different values of the dimensionless acceleration $\alpha = A_0\omega^2/g$ of the box (here $\alpha = 0$, 1, 2, 5, and 10). The contact time used here was $t_c = 0.7{\times}10^{-4}$ s. In Fig.33(b) we plot the corresponding number-density profiles. For small α-values we find that most particles are situated near the bottom of the box; the packing is dense. For large α-values, the particles

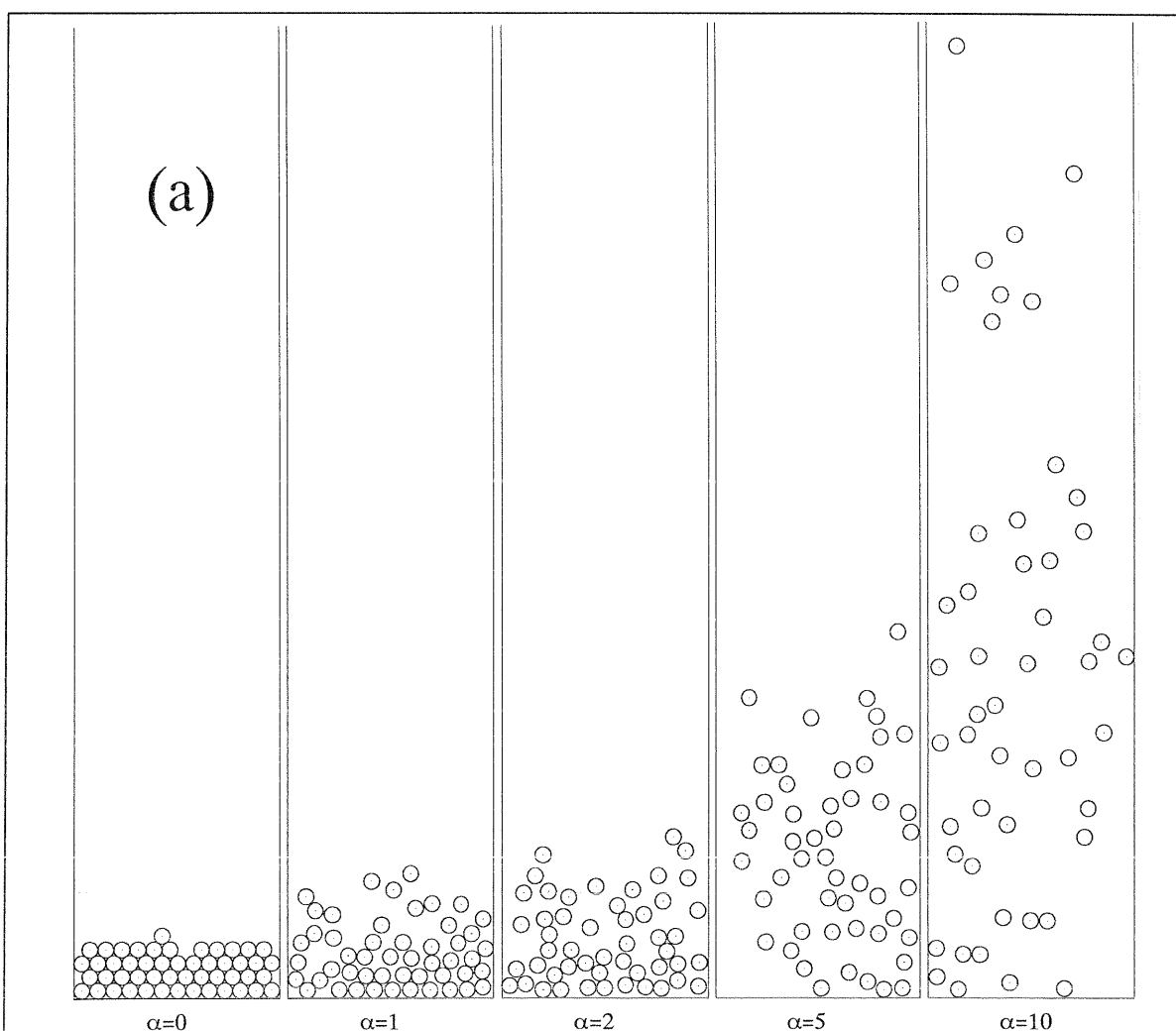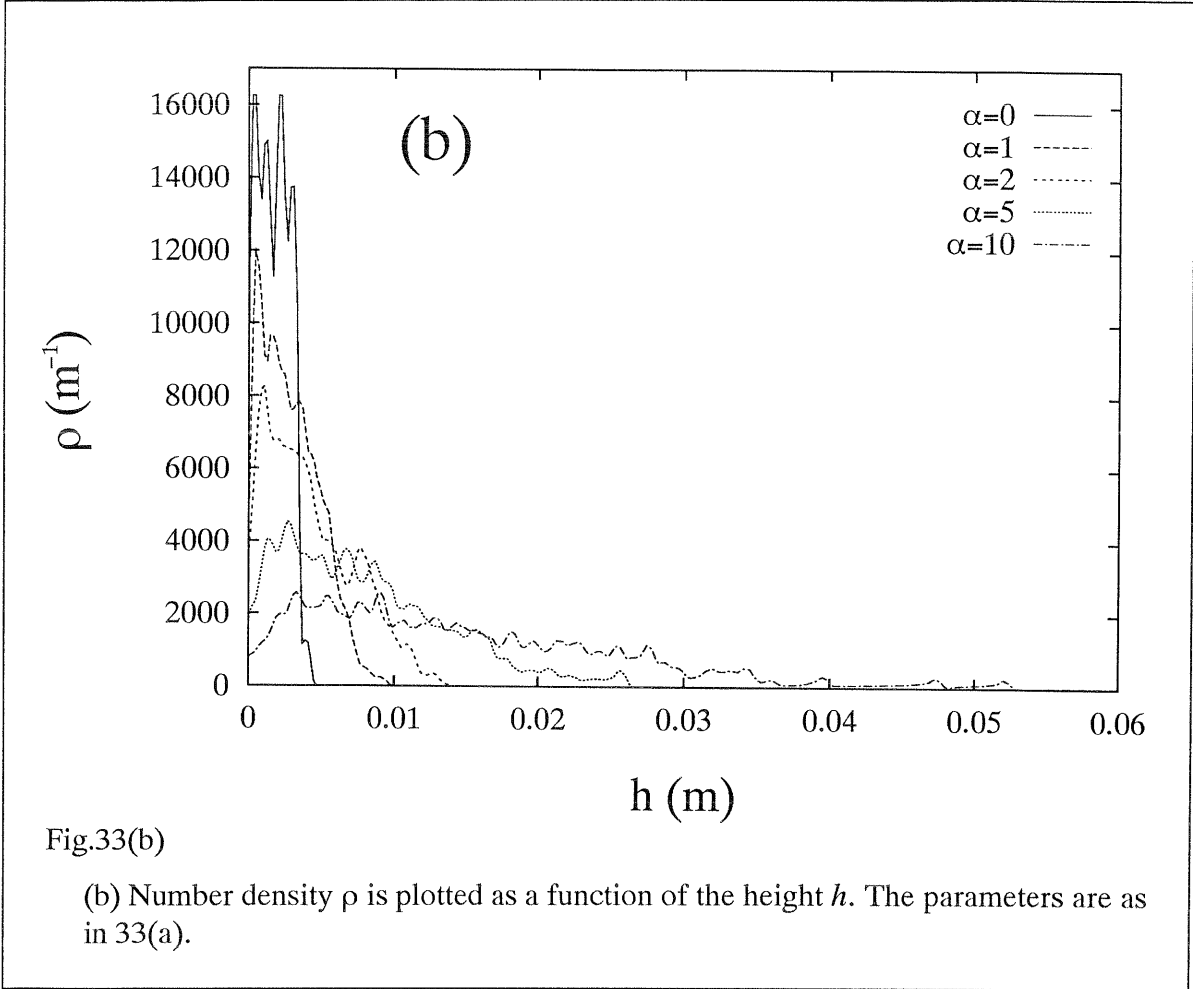| $\alpha=0$ | $\alpha=1$ | $\alpha=2$ | $\alpha=5$ | $\alpha=10$ |

Fig.33:

(a) Typical snapshots of MD simulations. We have $N = 50$ particles in a box of width $L = 13\,d$. The parameters used are $\varepsilon = 0.92$, $t_c = 0.7{\times}\,10^{-4}$ s, $f = 40$ s^{-1}, and α varies between 1 and 10. The snapshots are taken in the steady state at phase zero.

Fig.33(b)

(b) Number density ρ is plotted as a function of the height h. The parameters are as in 33(a).

have long times of free flight between collisions. For the simulations in Fig.33 we calculated σ, as given in Eq.(51), and found $\sigma \cong$ 37, 52, 74, and 120 for $\alpha = 1$, 2, 5, and 10, respectively.

At first using $N = 50$ and $\varepsilon = 0.92$ we perform simulations in which we vary both the frequency f and the amplitude A_0 of the vibrations. Results are displayed in Figs.34. In Fig.34(a) we plot $h_{cm}-h_{cm0}$ as a function of α for several simulations, in which t_c varies between 7×10^{-4} s ($K/m_{red} = 2\times10^7\text{s}^{-2}$, $\mu = 118.7\text{ s}^{-1}$) and 2.2×10^{-5} s ($K/m_{red} = 2\times10^{10}\text{s}^{-2}$, $\mu = 3752\text{ s}^{-1}$). The amplitude A_0 varies from $0.1\ d$ to $6\ d$ and the frequency f varies from 20 s^{-1} up to 400 s^{-1}. The parameter sets for the symbols in Fig.34(a) are given in Table.1.

To examine the dependence of the results on size dispersity we perform two series of simulations with frequency $f = 40\text{ s}^{-1}$ in which we vary A_0, so that $0.08 < A_0/d < 5.9$; here $L/d = 13$ and $t_c = 7\times10^{-4}\text{s}$. As the size distribution parameter we take $w=0$ (open triangles) and $w=0.05$ (filled circles). Hence, for slight diameter fluctuations we observe no difference in the behavior of h_{cm}. For $\alpha > 10$ these data increase superlinearly. We connect this to the fact that for the parameters used, in this α-range the maximal penetration x_{max}

becomes comparable to the radius of the particles, and thus the MD simulations no longer reproduce the behavior of metallic particles. To ascertain this statement further we present simulations (full triangles) obtained for $3.1 < A_0/d < 7.0$, and $w = 0$, for the same values of f and L/d. Contrary to the situation above we use a much smaller contact time, $t_c = 7\times10^{-5}$s here. In this case the linear regime extends to higher α-values. This result is reasonable, and is supported by the fact that we find that the data converge when t_c is decreased; in the following we will take care that the values of t_c used are small enough.

To test that the algebraic dependence of h_{cm}-h_{cm0} on α, i.e. on A_0 is not due to the particular frequency used we carried out two series of simulations in which we set $f = 100$ s^{-1}; the first uses $t_c = 7\times10^{-4}$s and $0.01 < A_0/d < 0.32$ (diamonds for $\alpha < 20$), the second one $t_c = 7\times10^{-5}$s and $1.25 < A_0/d < 4.34$ (diamonds for $\alpha \geq 50$). Here we again find an algebraic dependence of h_{cm}-h_{cm0} on α over two orders of magnitude in α. To find the dependence of h_{cm}-h_{cm0} on the frequency f we performed three series of simulations with slightly varying A_0, so that $0.50 < A_0/d < 0.63$ and varying frequency, 20 s^{-1} $< f < 141$ s^{-1}; the contact times are here 2.2×10^{-5}s $< t_c < 2.2\times10^{-4}$s (open circles). Note the different slope of these results, which indicates that the dependence of h_{cm}-h_{cm0} on f^2 is different from that on A_0. Note that f^2 is proportional to $\alpha = (A_0\omega^2)/g$.

To demonstrate that the presence of the walls only plays a limited role in this parameter range we also performed simulations under periodic boundary conditions, by taking as the repeat unit a box of width $L/d = 14$. Because of this somewhat larger L-value, we expect the results to change in the order of 10%. Paralleling the last simulations (open circles) we varied A_0, f and t_c by taking $0.50 < A_0/d < 0.55$ as well as 60 s^{-1} $< f < 141$ s^{-1}, and $2.2\times10^{-5} < t_c < 7\times10^{-5}$ s. The data for periodic boundary conditions (filled squares) display behaviors similar to the data found for boxes with walls; as expected, the value of h_{cm}-h_{cm0} is somewhat higher. To look at the behavior of the system at lower amplitudes we performed for periodic boundary conditions ($L/d = 14$) an additional set of simulations with $A_0/d = 0.16$ and $t_c = 2.2\times10^{-4}$ s, in which we varied f in the range 40 s^{-1} $< f < 98$ s^{-1} (open squares). Finally to test the behavior of the system for extremely small amplitudes (and high frequencies) we performed a set of simulations in which we varied A_0 such as to have $5\times 10^{-6} < A_0/d < 10^{-4}$, while keeping fixed $f = 400$ s^{-1}, $L/d = 14$, and $t_c = 2.2\times10^{-4}$ s (crosses).
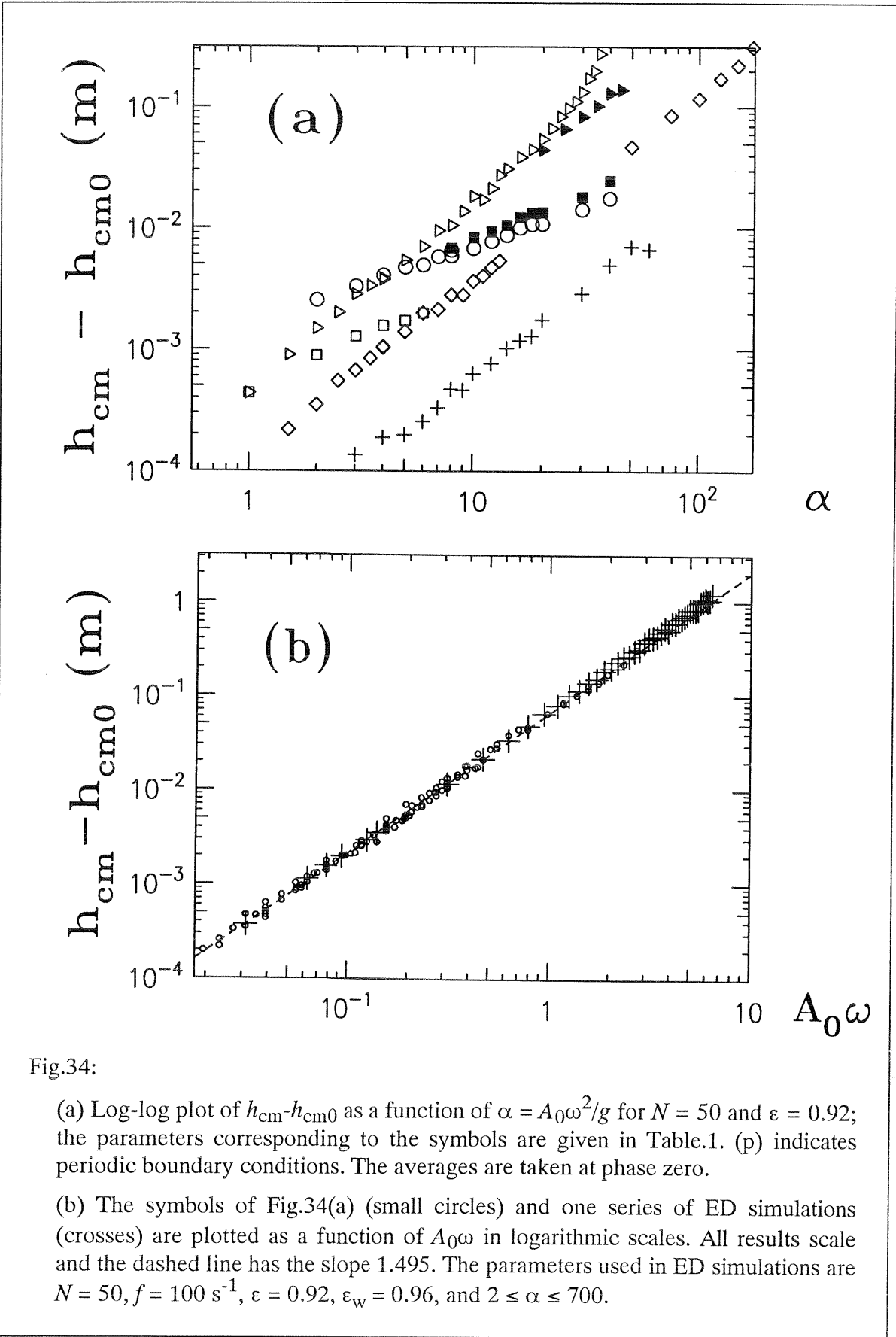
Fig.34:

(a) Log-log plot of h_{cm}-h_{cm0} as a function of $\alpha = A_0\omega^2/g$ for $N = 50$ and $\varepsilon = 0.92$; the parameters corresponding to the symbols are given in Table.1. (p) indicates periodic boundary conditions. The averages are taken at phase zero.

(b) The symbols of Fig.34(a) (small circles) and one series of ED simulations (crosses) are plotted as a function of $A_0\omega$ in logarithmic scales. All results scale and the dashed line has the slope 1.495. The parameters used in ED simulations are $N = 50, f = 100$ s^{-1}, $\varepsilon = 0.92$, $\varepsilon_w = 0.96$, and $2 \leq \alpha \leq 700$.

	A_0/d_0	$f\,(\text{s}^{-1})$	L/d_0	$t_c\,(\text{s})$
▷	0.08 - 5.9	40	13	7×10^{-4}
●	0.08 - 5.9	40	13 $w=0.05$	7×10^{-4}
▶	3.1 - 7.0	40	13	7×10^{-5}
◇	0.01 - 0.32 1.25 - 4.34	100 100	13 13	7×10^{-4} 7×10^{-5}
○	0.63 0.55 0.50	20 - 57 60 - 90 100 - 141	13 13 13	2.2×10^{-4} 7×10^{-5} 2.2×10^{-5}
■	0.55 0.50	60 - 90 100 - 141	14 (p) 14 (p)	7×10^{-5} 2.2×10^{-5}
□	0.16	40 - 98	14 (p)	2.2×10^{-4}
+	$5\times10^{-6} - 10^{-4}$	400	14 (p)	2.2×10^{-4}

Table.1

Parameters and symbols used in Fig.34(a).

In Fig.34(b) we replot the results of Fig.34(a) (except for the data where x_{max} was found to be too large, see the discussion above). We display the dependence of $h_{cm}-h_{cm0}$ on $A_0\omega$ in logarithmic scales. We observe an impressive scaling of the data; a linear fit leads to a slope of 1.495 ± 0.009. Within this uncertainty we can hence assert that $h_{cm}-h_{cm0} \propto (A_0\omega)^{3/2}$. Now we plot, as crosses, the result of a series of ED simulations, where we use $N = 50$ particles, $f = 100\ \text{s}^{-1}$, $\varepsilon = 0.92$, $\varepsilon_w = 0.96$ and we vary α in the range $2 \le \alpha \le 700$. As is obvious from the figure the ED simulations lead to the same results as the MD simulations.

In Fig.35 we plotted the number-density profiles $\rho(h)$ for different α-values, $6 < \alpha < 50$. We scale the results by displaying the height h in units of h_{cm} and the number-density in units of $\rho_0 = 1/h_{cm}$. For comparison we also give the exponential function $\exp(-h/h_{cm})$, represented as a straight line. This exponential form is the density profile of a Boltzmann gas without dissipation. From Figs.34 and 35 we find that in the fluidized regime the height of the center of mass (and thus the potential energy) scales with the typical velocity $A_0\omega$, i.e. $(A_0\omega)^{3/2}$, of the box and not with the acceleration α. This situation parallels our findings [62] in the 1D case (see Sec.4). The density profiles for different amplitudes and frequencies also scale with h_{cm} and do not change for given N and ε as long as the system is fluidized (compare Sec.4.3.4 for 1D). We attribute the fact that the density profiles differ from the Boltzmann-gas behavior to the dissipative aspect of the collisions.
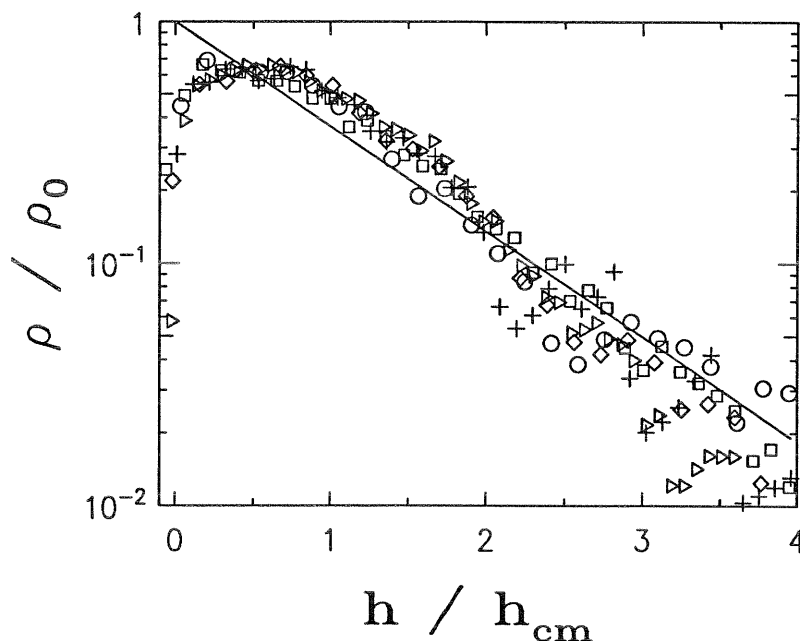
Fig.35:

Logarithmic-linear plot of the normalized number density ρ/ρ_0 for $N = 50$ and $\varepsilon = 0.92$ and different f- and A_0-values from Figs.2. We use $f = 40 \text{ s}^{-1}$ with $A_0/d = 0.93$ such that $\alpha = 6$ (squares), $A_0/d = 2.17$ such that $\alpha = 14$ (diamonds) and $A_0/d = 4.7$ such that $\alpha = 30$ (circles). These data correspond to the triangles of Fig.2(a). We also use $f = 100 \text{ s}^{-1}$ with $A_0/d = 0.5$ such that $\alpha = 20$ (triangles) and $A_0/d = 1.24$ such that $\alpha = 50$ (crosses). These data correspond to the diamonds of Fig.34(a). The straight line corresponds to $\exp(-h/h_{cm})$.

5.1.2.   Dissipation in 2D systems

In the following we will discuss the dependence of h_{cm} on N and ε, the parameters which control dissipation. In Fig.36(a) we plot h_{cm}-h_{cm0} as a function of $X = (N/n_b)(1-\varepsilon)$. The choice of X is based on the findings of Sec.3.2.4.; the definition is consistent with the 1D case, in which $n_b = 1$, so that in 1D one has, as before, $X = N(1-\varepsilon)$. In the simulations displayed in Fig.36(a) we use $L = 13\,d$ (no periodic boundary conditions), the other parameters can be extracted from Table.2. To find the behavior of the system for different ε-values we first carry out three series of simulations, in which we set $N = 50$ and scan ε in the range $0.5 < \varepsilon < 0.99$. Here we use $f = 40\ \text{s}^{-1}$ and $\alpha = 10$ (open triangles), $f = 100\ \text{s}^{-1}$ and $\alpha = 10$ (filled triangles) as well as $f = 100\ \text{s}^{-1}$ and $\alpha = 50$ (circles); t_c is taken in the range $7{\times}10^{-5}\text{s} < t_c < 7{\times}10^{-4}\text{s}$. In general we find that h_{cm}-h_{cm0} decreases with increasing X, i.e. with decreasing ε.

Furthermore, in two more sets of simulations we keep $N = 100$ fixed and scan ε in the range $0.2 < \varepsilon < 0.97$. We take here $t_c = 7{\times}10^{-5}\text{s}, f = 100\ \text{s}^{-1}$ and choose $\alpha = 10$ (results indicated by diamonds) and $\alpha = 50$ (results indicated by crosses). The result of this set of simulations is that for $X > 2$, i.e. $\varepsilon < 0.5$, the data no longer follow an algebraic behavior; in this X-range the fluctuations of h_{cm}-h_{cm0} are much larger than for $X < 2$. The system is here quite far from the fluidized regime.

To test the behavior of the system when the number of particles changes, we vary N in the range $15 < N < 250$ and use ε-values in the range $0.9 < \varepsilon < 0.98$; furthermore, we take $f = 40\ \text{s}^{-1}$ and $\alpha = 10$ (open squares), $f = 100\ \text{s}^{-1}$ and $\alpha = 10$ (hexagons) as well as $f = 100\ \text{s}^{-1}$ and $\alpha = 50$ (filled squares), while t_c varies in the interval $3{\times}10^{-5}\text{s} < t_c < 7{\times}10^{-4}\text{s}$. We again find that h_{cm}-h_{cm0} decreases with increasing X, i.e. with increasing N. We tested for several parameters that the height of the center of mass does not change much with decreasing t_c.
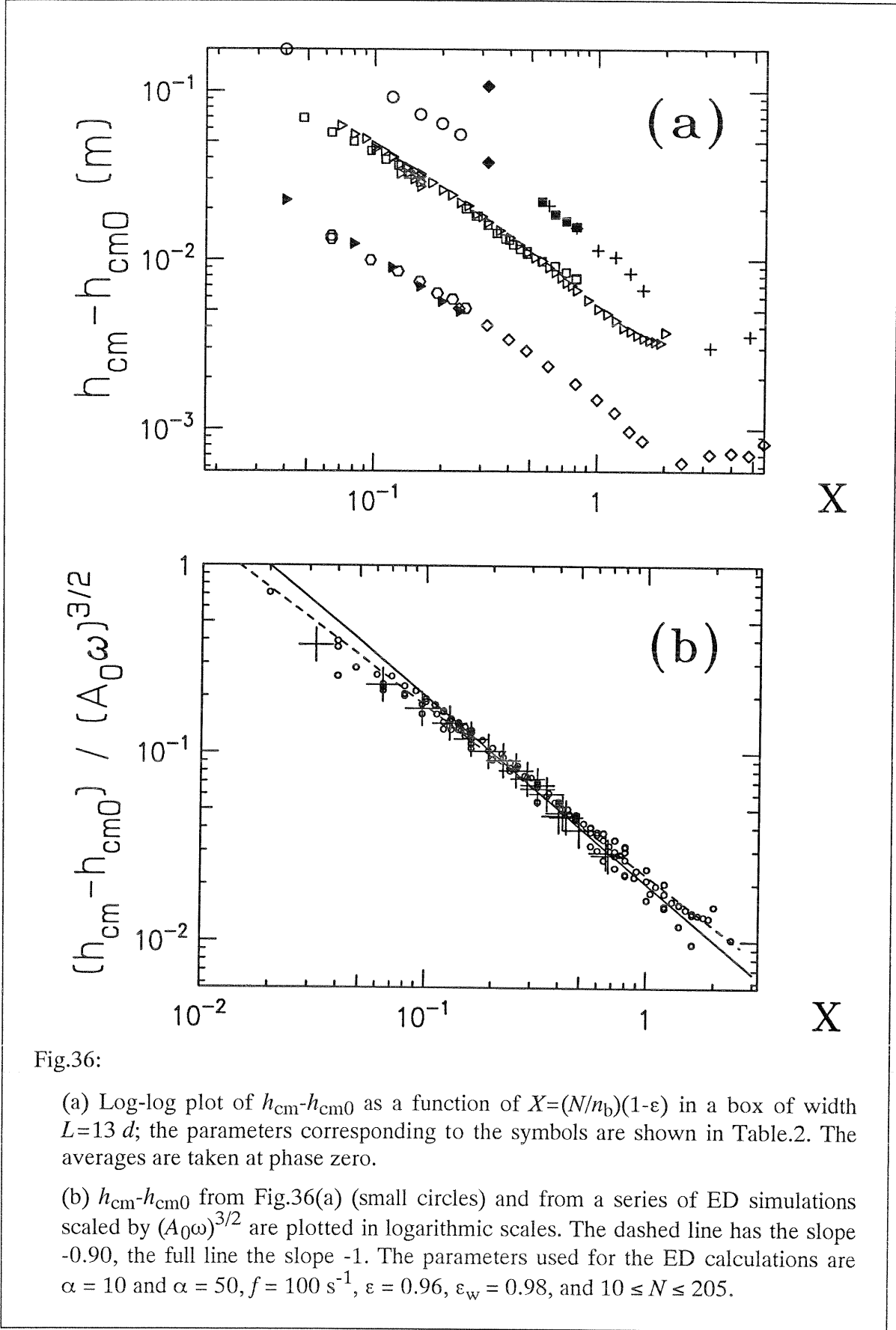
Fig.36:

(a) Log-log plot of h_{cm}-h_{cm0} as a function of $X=(N/n_b)(1$-$\varepsilon)$ in a box of width $L=13$ d; the parameters corresponding to the symbols are shown in Table.2. The averages are taken at phase zero.

(b) h_{cm}-h_{cm0} from Fig.36(a) (small circles) and from a series of ED simulations scaled by $(A_0\omega)^{3/2}$ are plotted in logarithmic scales. The dashed line has the slope -0.90, the full line the slope -1. The parameters used for the ED calculations are $\alpha = 10$ and $\alpha = 50, f = 100$ s^{-1}, $\varepsilon = 0.96$, $\varepsilon_w = 0.98$, and $10 \le N \le 205$.

	N	ε	α	$f\,(\mathrm{s}^{-1})$	$t_c\,(\mathrm{s})$
▷	50	0.5 - 0.9825	10	40	$7\times10^{-5} - 7\times10^{-4}$
▶	50	0.94 - 0.99	10	100	7×10^{-5}
○	50	0.7 - 0.925	50	100	7×10^{-5}
◇	100	0.2 - 0.97	10	100	7×10^{-5}
+	100	0.2 - 0.925	50	100	7×10^{-5}
□	15-250	0.96	10	40	$7\times10^{-5} - 7\times10^{-4}$
⬡	40-160	0.98	10	100	3×10^{-5}
■	175-250	0.9	50	100	$7\times10^{-5} - 7\times10^{-4}$
◆	100 200 400	0.96 0.98 0.99	100 100 50	100 100 100	7×10^{-5}

Table.2

Parameters and symbols used in Fig.36(a).

In Fig.36(b) we plot on the vertical axis $(h_{\mathrm{cm}}-h_{\mathrm{cm0}})/(A_0\omega)^{3/2}$ as a function of X and we again find that the data scale. The best linear fit to the data gives the slope -0.90 ± 0.01; as indicated in Fig.36(b), a value of -1 is still acceptable. Hence, for simplicity we have $h_{\mathrm{cm}}-h_{\mathrm{cm0}} \propto 1/X$. In addition, we carried out a series of ED simulations, where we used $f = 100\,\mathrm{s}^{-1}$, $\alpha = 10$ and $\alpha = 50$, $\varepsilon = 0.96$, and $\varepsilon_{\mathrm{w}} = 0.98$, while we varied N in the range of $10 \leq N \leq 205$. These data are plotted as crosses in Fig.36(b); we again find the results of ED and MD simulations to be in impressive agreement. We attribute the deviations from the X^{-1} behavior for small X-values to the dissipative collisions with the walls.

Fig.37:

Logarithmic-linear plot of the normalized number density ρ/ρ_0 for $N = 50$, $A_0 = 1.55\,d$ and $f = 40\,\mathrm{s}^{-1}$, such that $\alpha = 10$. Here ε equals 0.6 (crosses), 0.8 (triangles), 0.9 (diamonds) and 0.95 (squares, connected by dashed lines). These simulations correspond to the triangles of Fig.36(a). The straight line corresponds to $\exp(-h/h_{\mathrm{cm}})$.
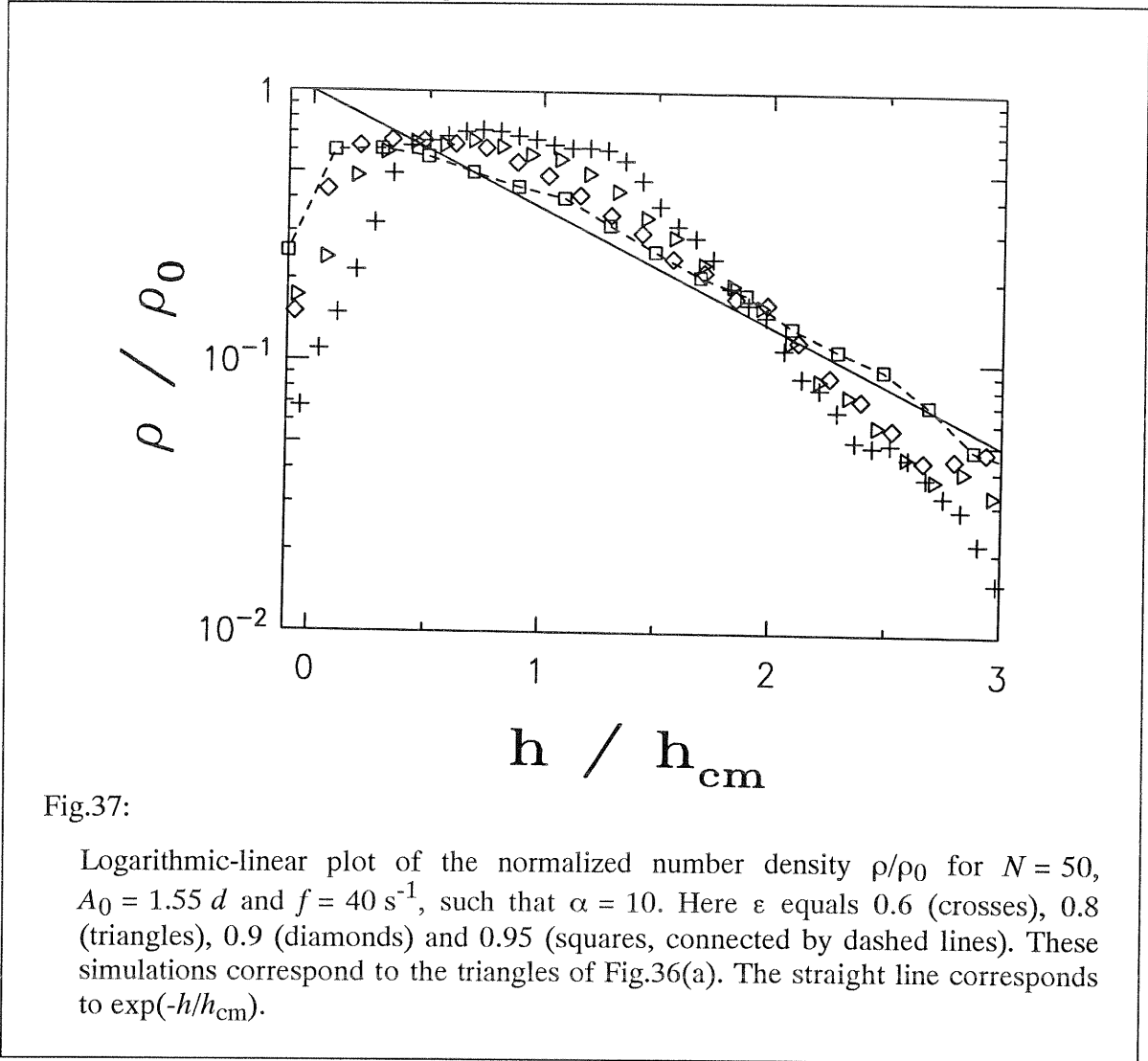
In Fig.37 we plot the normalized density profiles for $N = 50$, $f = 40\,\mathrm{s}^{-1}$ and $\alpha = 10$, while we vary ε between 0.6 and 0.95, i.e. $1.6 > X > 0.2$. The normalized density profiles tend to an exponential function when ε tends towards unity. In other words, if the dissipation is low (small X) the density profiles are of nearly-exponential form, whereas for large X-values deviations occur: the particles concentrate mainly at the bottom, and the system is less spread-out, i.e. a dense state coexists with a dilute state at the top - we have surface fluidization. For large height-width ratios, i.e. $n_{\mathrm{h}}/n_{\mathrm{b}} > 1$, we find an additional dilute region with extremely high average velocities at the bottom.

86

5.1.3.   The effect of walls in 2D

We focus on the height-width ratio n_h/n_b of the system and on effects induced by the walls. In Fig.34 we presented some simulations with periodic boundary conditions, i.e. no walls. For the parameters used the behavior of the system does not depend on the existence of walls. To test this statement for distinct conditions we present a series of MD simulations where we vary the width of the box n_b and the acceleration of the bottom plate α. In Fig.38 we plot the reduced height of the center of mass scaled by $(A_0\omega)^{3/2}$ as a function of the width of the box n_b. We fix the height of the system at rest such that $n_h = 4$ and $N = n_h n_b$. We use $f = 100$ s^{-1}, $\varepsilon = 0.95$, $t_c = 2\times10^{-4}$s and vary the amplitude A_0 such that $\alpha = 10$, 20, and 50 corresponding to $A_0\omega = 0.156$, 0.312, and 0.781 ms^{-1}. The results for a fixed n_b and
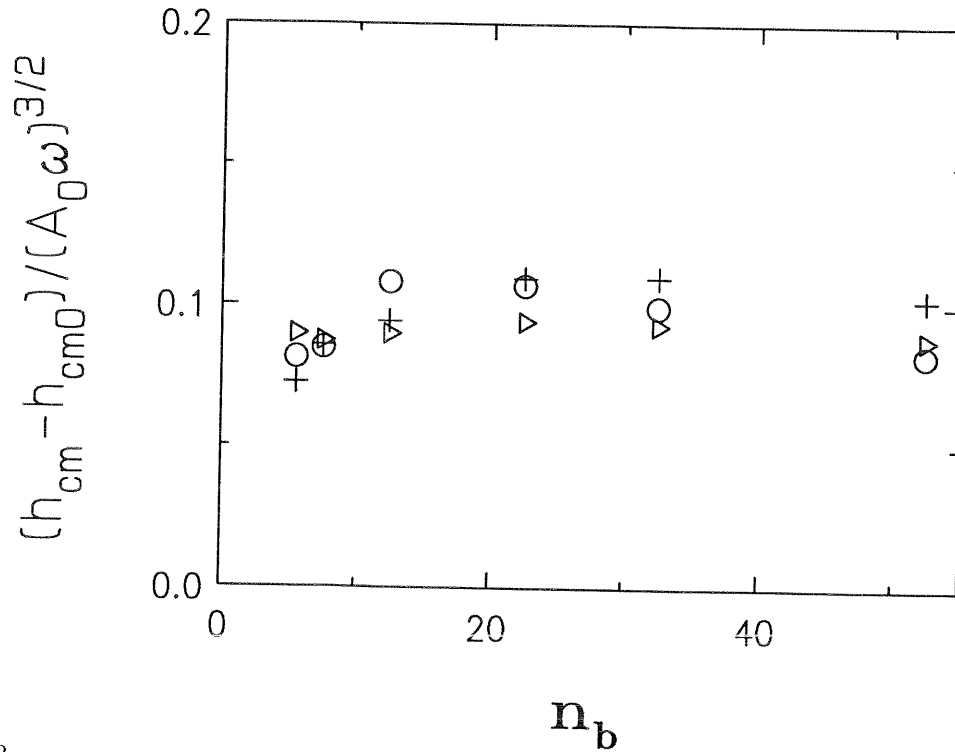
Fig.38:

h_{cm}-h_{cm0} scaled by $(A_0\omega)^{3/2}$ is plotted as a function of the width n_b of the box for $\varepsilon = 0.95$, $f = 100$ s^{-1} and fixed height $n_h = 4$ such that $N = n_h n_b$. We use different accelerations $\alpha = 10$ (triangles), $\alpha = 20$ (circles), $\alpha = 50$ (crosses). Here $t_c = 2\times 10^{-4}$s.

different α scale within the statistical fluctuations of the height of the center of mass and agree with the predicted value of $\left(h_{cm} - h_{cm0}\right)/\left(A_0\omega\right)^{3/2} \cong C_{2D}/X = 0.1$ where $C_{2D} = 0.02 \text{ s}^{3/2}\text{m}^{-1/2}$ is a constant obtained from the simulation results of this subsection and $X = (N/n_b)(1-\epsilon) = 4(1-\epsilon)$. Thus the consequences of the width of the container for the behavior of the system are rather weak.

To test the influence of dissipative walls on the system we present a set of ED simulations in Fig.39 with $N = 50$ particles in a box of width $L = 13$ d; the frequency of vibration is $f = 100 \text{ s}^{-1}$ and the amplitude is varied such that $4.8\times10^{-5}\text{m} < A_0 < 0.02$ m. One series of simulations is carried out using $\epsilon = 0.92$ and $\epsilon_w = 0.96$, depicted as small crosses [compare to Fig.34(b)] and as triangles. For the second series we again use $\epsilon = 0.92$ but here the dissipation during collisions with the wall is neglected, i.e. $\epsilon_w = 1$; these simulations are depicted as circles. We find that all data follow the power law $(A_0\omega)^{3/2}$, observed in
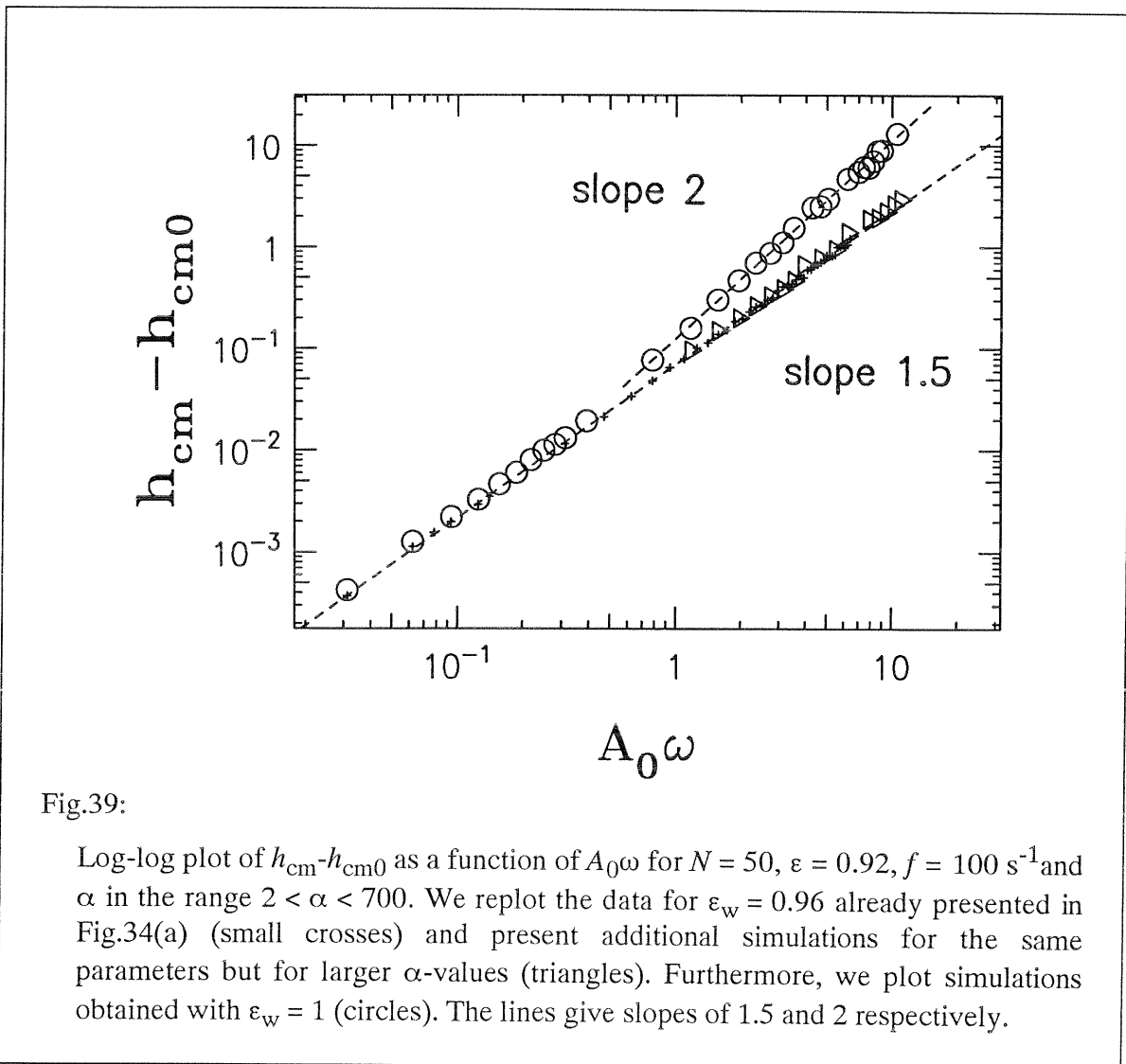
Fig.39:

Log-log plot of h_{cm}-h_{cm0} as a function of $A_0\omega$ for $N = 50$, $\epsilon = 0.92$, $f = 100 \text{ s}^{-1}$ and α in the range $2 < \alpha < 700$. We replot the data for $\epsilon_w = 0.96$ already presented in Fig.34(a) (small crosses) and present additional simulations for the same parameters but for larger α-values (triangles). Furthermore, we plot simulations obtained with $\epsilon_w = 1$ (circles). The lines give slopes of 1.5 and 2 respectively.

Fig.34(b) for $A_0\omega < 0.4\,\text{ms}^{-1}$ whereas the power is 2 instead of 3/2 for $A_0\omega > 0.4\,\text{ms}^{-1}$ if $\varepsilon_w = 1$. The power laws 3/2 and 2 are represented as dashed lines in Fig.39. These calculations leads to the conclusion that 2D vibrated systems depend on the velocity of the bottom plate like 1D columns [Sec.4] but the power law is different due to the existence of dissipative walls. If the dissipation with the walls is neglected the power law shows up with a cross over from 3/2 to 2 (for our parameters the crossover velocity is $A_0\omega \cong 0.4\,\text{ms}^{-1}$). For small velocities, i.e. $A_0\omega << 0.4\,\text{ms}^{-1}$ the system is rather dense whereas for large velocities, i.e. $A_0\omega >> 0.4\,\text{ms}^{-1}$ it is dilute. We attribute the change in behavior to the mean free path l. For the simulation with $A_0\omega = 0.4\,\text{ms}^{-1}$ we compute $l \cong 0.38\,L$.

Thus the behavior of vibrated arrays of beads in 2D changes if the mean free path is comparable to the size of the system and if the collisions with the walls are not dissipative. If the density is large, i.e. $l \cong d << L$, the next collision of a selected bead will involve one of its nearest neighbors; in contrast, if the density is small, i.e. $l >> L$, the bead can collide with another particle or with a wall. If the contact with the walls is dissipative the behavior of the systems is the same for $l/L << 1$ as well as for $l/L >> 1$ because any contact is dissipative. The situation is changed dramatically if the possible contact with the walls is *not* dissipative; the larger l/L, i.e. the larger the probability for a contact with a wall, the lower the average dissipation.

5.2. MD simulations of convection

In the following we present results of MD simulations in 2D with dissipative walls; the system consists of $N = 100$ particles of mass m with restitution coefficient $\varepsilon = 0.9$. To facilitate the connection to Ref.[48] we use the same units: the length is then given in units of 1 mm and the time in units of $0.01\,\text{s} = 1\,\text{cs}$. We set $g = 10\,\text{ms}^{-2} = 1\,\text{mm/(cs)}^2$, $d = 2\,\text{mm}$ and $A_0 = 0.55\,d = 1.1\,\text{mm}$. We vary t_c between 0.00316 cs and 0.316 cs, i.e. from a realistic value to a value two orders of magnitude larger. With these ε and t_c, K/m in Eq.(14) obeys $493500\,\text{(cs)}^{-2} > K/m > 49.35\,\text{(cs)}^{-2}$; furthermore, one also has $33.3\,\text{(cs)}^{-1} > D_n = D_t > 0.333\,\text{(cs)}^{-1}$ in Eqs.(15) and (16). We take $\tilde{D}_n$ and $\tilde{D}_t$ as dissipation parameters for the interactions between the particles and the lateral walls $\tilde{D}_n = 20\,D_n$ and $\tilde{D}_t = 20\,D_t$.

To monitor the onset of convection we use the order parameter J introduced by Taguchi [48]. For this the container is divided into cells of size length $d = 2\,\text{mm}$ (this corresponds to the spheres' diameter). One counts the number of particles coming into or going out of the cell centered at r, and averages with respect to time:

$$\langle J(r) \rangle = \left\langle \sum_{i=1}^{N} \tfrac{1}{2} \big| \delta(x_i(t) - r) - \delta(x_i(t - \Delta t) - r) \big| \big\{ x_i(t) - x_i(t - \Delta t) \big\} \right\rangle_t .$$ (52)

Here r denotes the integer coordinates of the cell considered; $x_i(t)$ is the integer coordinate of the cell which contains the center of particle i at time t. Thus $\delta(x_i(t) - r)$ equals one, if particle i is at time t in cell r, and zero otherwise. In Eq.(52) the term with absolute value signs equals zero for the particles which during Δt did not change their cells; it equals unity for the particles which have changed their cell between times t-Δt and t. The brackets indexed with t denote the temporal averaging. We now define J, the overall strength of convection through:

$$J = \sqrt{\sum_r J(r)^2} .$$ (53)

In Fig.40 we plot J, averaged over 180 periods, as a function of α for the t_c values 0.141 cs, 0.1 cs, 0.0316 cs and 0.00316 cs. The error bars on J are of the order of magnitude of the symbol size. The main result of Fig.40 is that J is in general an increasing function of α. For quite large α J decreases again, a fact due to the decrease in the particles' density. We focus on the onset of convection. Of interest are moderate values of α. We find that for large t_c convection starts for α around unity (as found by Taguchi [48,91]) whereas for small t_c, i.e. closer to the physical situation, the onset of convection is above $\alpha = 2$. Furthermore, the strength of the convection decreases with decreasing t_c.

To visualize this statement we present in Figs.41(a)-41(c) simulations performed at constant α and ε ($\alpha = 2$, $\varepsilon = 0.9$), while t_c varies: we use $t_c = 0.222$ cs (a), 0.1 cs (b), and 0.01 cs (c). We display the displacements of the particles after 10 vibration periods (at phase 0) by arrows; the initial positions are given by circles. Fig.41(a) shows convection in the whole volume, Fig.41(b) only in the upper half and Fig.41(c) only some motion in the uppermost layer. Paralleling Figs.41(a) and 41(b) we plot in Figs.42(a) and 42(b) the field $J(r)$. The average is taken over 180 vibration periods; for convenience of presentation the length of the arrows was increased by a factor of four. Again, for decreasing t_c we find decreasing convection. An analogous figure to 41(c) shows no convection; we restrain from presenting it here.
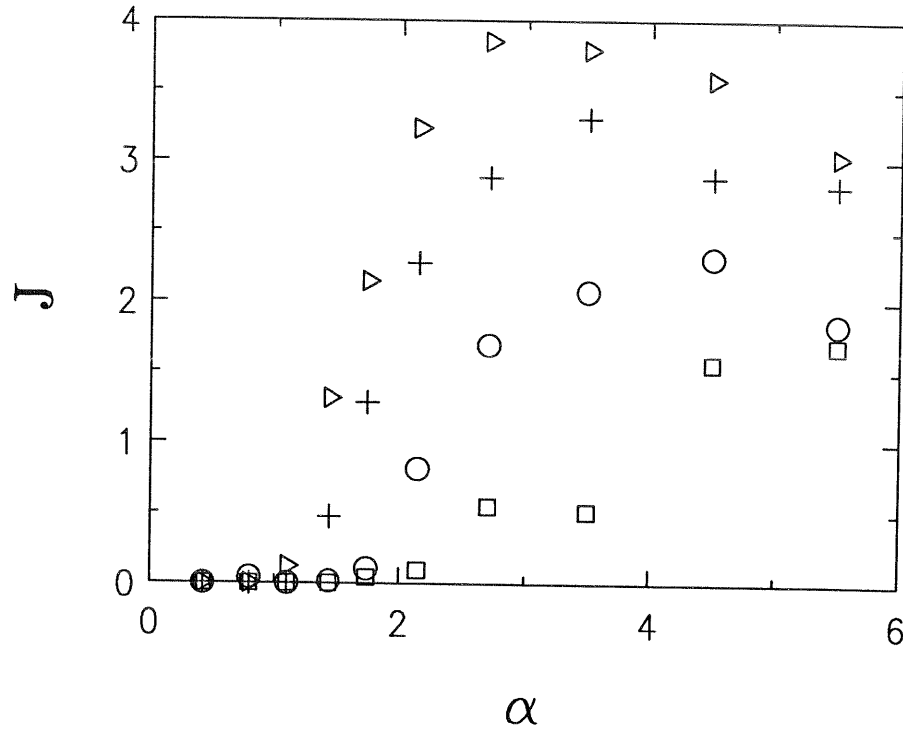
Fig.40:

The convection strength J, Eq.(53), as a function of α, Eq.(8). The parameters used are $g = 10 \, \text{ms}^{-2}$, $N = 100$, $\varepsilon = 0.9$, $d = 2 \, \text{mm}$, $L = 13d$, and $A_0 = 1.1d$. The contact times t_c are 0.141 cs (triangles), 0.1 cs (crosses), 0.0316 cs (circles) and 0.00316 cs (squares).

An explanation for the dependence of J on t_c may be found in terms of the detachment effect. In previous sections we showed that even when colliding pairs dissipate their energy strongly, the MD simulations may lead to large interparticle-distance fluctuations and low overall dissipation. A characteristic parameter for this behavior is the ratio $\sigma = l/(\bar{v}t_c)$ between the typical free-flight time and t_c, see Eq.(51). In Eq.(51) l was approximated through the mean free path $l \approx (h_{\text{cm}} - h_{\text{cm0}})L / (Nd)$ (here $2(h_{\text{cm}} - h_{\text{cm0}})L$ is the average free volume and $2d$ is the cross section of hard spheres in 2D); $\bar{v}$ is a typical relative velocity, say $\bar{v} = \sqrt{\langle v^2 \rangle}$. The main result of subsection 5.1 was that when $\sigma \gg 1$ the simulation results (MD and event-driven, ED) agree quite well in 2D. For $\sigma \ll 1$, on the other hand, spurious effects connected with detachment occur (see Sec.3.2.3.). Thus σ is determined using $\sigma = (h_{\text{cm}} - h_{\text{cm0}})L / (Nd \, \bar{v}t_c)$, see Eq.(51), where h_{cm} is the height of the center of mass and h_{cm0} is the height of the center of mass at rest.
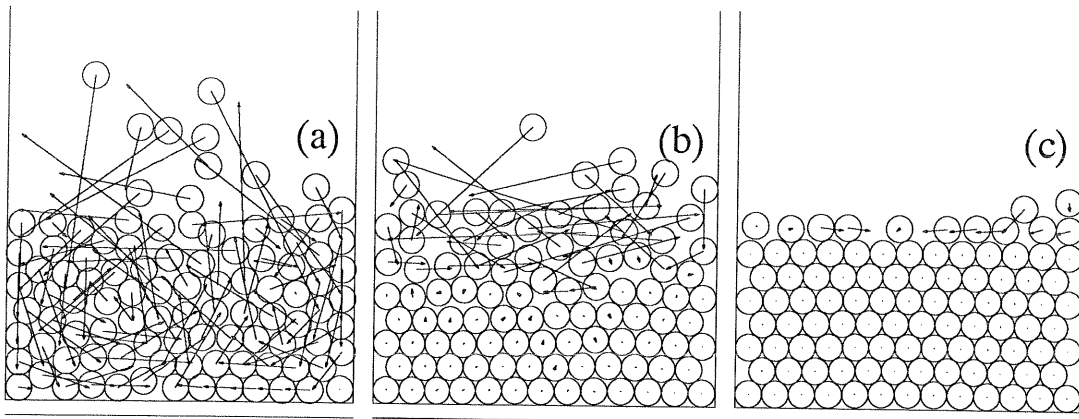
Fig.41:

(a) Plot of the particle distribution and the displacements for $g = 10$ ms^{-2}, $N = 100$, $\varepsilon = 0.9$, $d = 2$ mm, $L = 13d$, $A_0 = 1.1d$, and $\alpha = 2$. Here $t_c = 0.222$ cs.

(b) Parameters as in Fig.41(a). Here $t_c = 0.1$ cs.

(c) Parameters as in Fig.41(a). Here $t_c = 0.01$ cs.
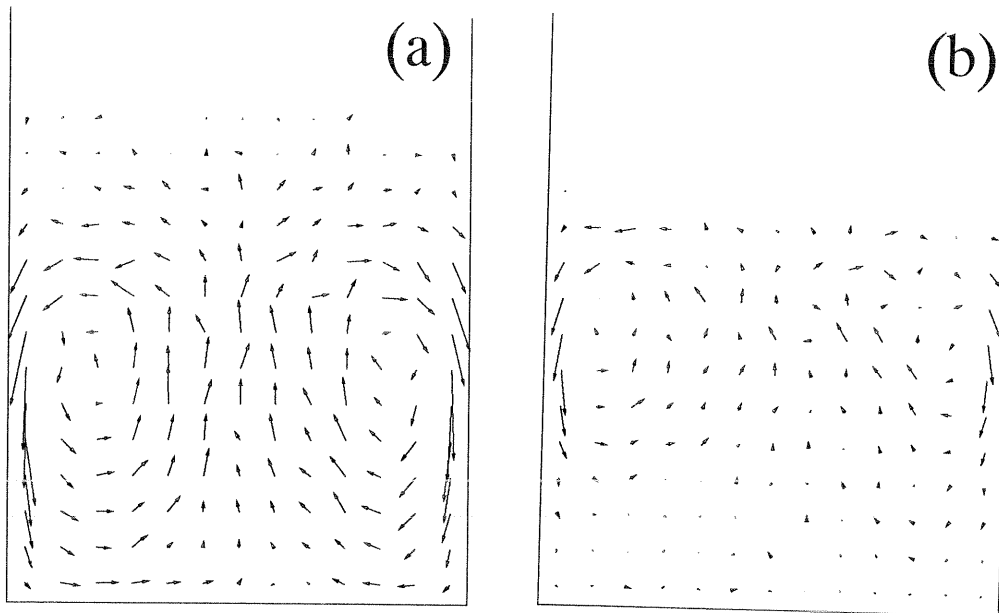
Fig.42:

(a) Plot of $J(r)$, Eq.(52), for the simulations shown in Fig.41(a).

(b) Plot of $J(r)$, Eq.(52), for the simulations shown in Fig.41(b).
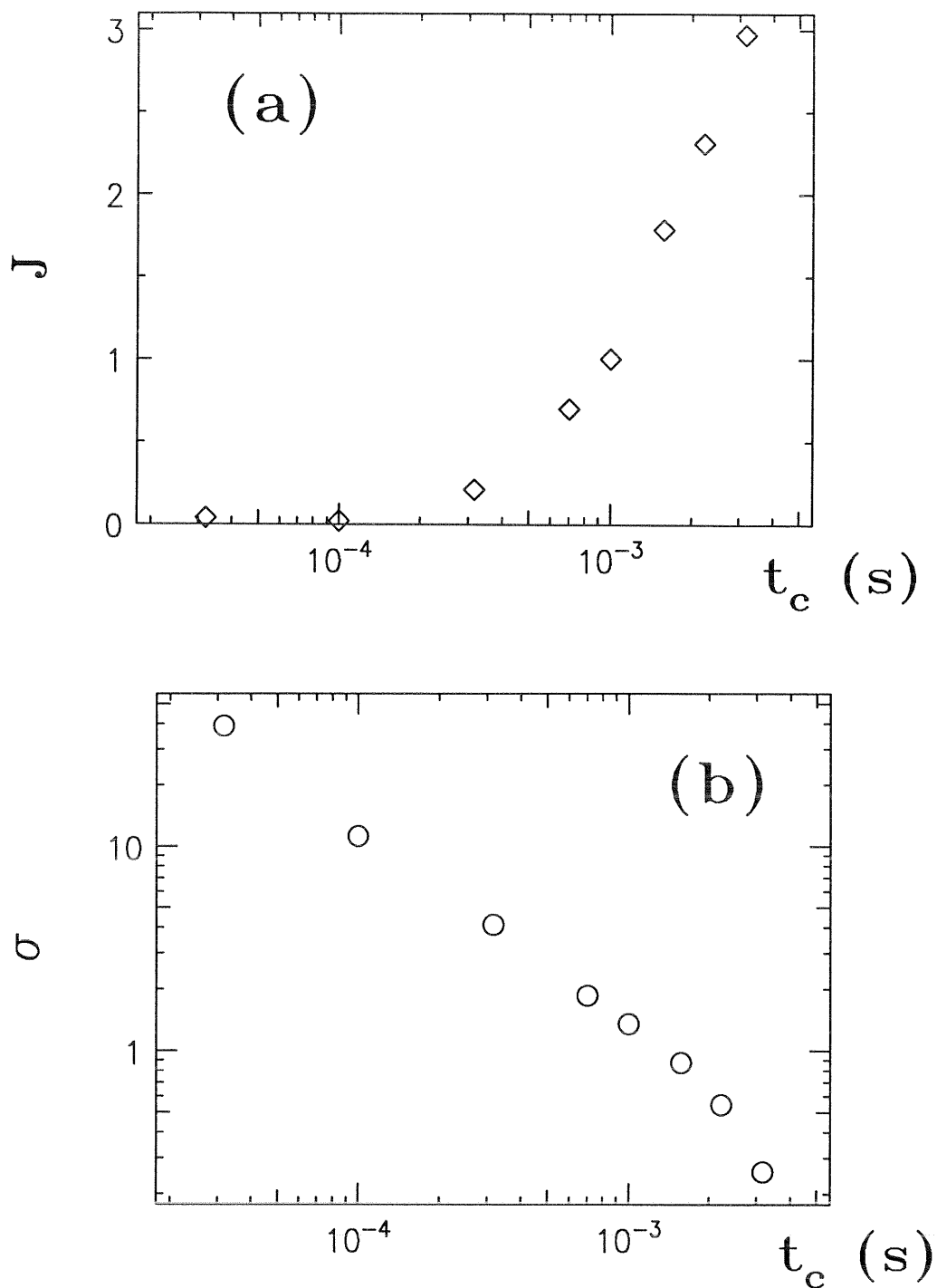
Fig.43:

(a) The convection strength J as a function of t_c for $g = 10\,\text{ms}^{-2}$, $N = 100$, $\varepsilon = 0.9$, $d = 2\,\text{mm}$, $L = 13d$, $A_0 = 1.1d$ and $\alpha = 2$. Here t_c varies between 0.00316 cs and 0.316 cs.

(b) Plot of σ as a function of t_c for the same parameters as in Fig.43(a).

We argue that the observed convection is related to high t_c-values (and small σ-values). To justify this we give results obtained for $N = 100$, $\varepsilon = 0.9$, $\alpha = 2$ and $A_0 = 0.55d = 1.1$ mm in Figs.43. In Figs.43(a) and 43(b) J and σ are plotted as a function of t_c. We observe that the sharp increase in the convection strength J correlates with the decrease in σ to values below unity and hence with the onset of the detachment effect in MD simulations.

We conclude that lowering t_c reduces the detachment, i.e. increases the density; by this convection is rendered more difficult. The time scales are also different: MD simulations may already show convection when monitoring a few vibration periods, whereas convection in experiments, such as block-motion, has waiting times much larger than the period of excitation [13].

6. Discussion and Conclusions

In summary, we introduced event driven as well as molecular dynamics methods to study dry granular materials. We presented an ED algorithm suited to dealing with both the fluidized and the clustered phase; furthermore, we discussed a MD scheme using linear as well as non-linear interaction laws. We established the connection between both simulation methods and gave an explanation for differences obtained in the results. In addition, we studied one-dimensional and two-dimensional model systems undergoing vertical vibrations and explored the transition from the fluidized to the condensed and clustered regime. We found scaling laws for the fluidized regimes in 1D and in 2D and presented the relevant parameters for granular systems under vibrations. We find that the behavior of 2D systems is strongly influenced by the existence of the walls. Besides fluidization we were interested in the onset of convection in model systems, an effect depending on the parameters used in MD simulations.

The ED simulations we presented follow a sequence of events and are based on binary collisions. If particles are in contact very often the computing time needed for ED simulations becomes very large. In 1D we developed the LRV procedure which is able to circumvent this problem. Clusters are allowed to occur for vanishing relative velocities and we sort events inside a cluster with respect to the relative velocites, i.e. the first event in a cluster involves the pair of particles with the largest relative velocity.

For MD simulations we introduced microscopic contact interaction laws and thus integrated Newtons equations of motion. The basic difference between ED and MD methods is the time, particles are in contact. In ED simulations the contact time is implicitly zero, whereas for MD simulations the contact time depends on the parameters used. We relate the restitution coefficient, defined for ED simulations, to the parameters used in MD simulations, i.e. to the spring constant and the dissipation parameter. A large spring constant, for example, corresponds to a small interaction time. We computed the contact time and we present the dependence of ε on the relative velocity for linear as well as non-linear interactions. We found that MD calculations imply insufficient energy dissipation in the system considered, when the number of dissipative contacts is large. This implies that the MD simulations over-estimate the density and energy fluctuations. The effect is most

obvious for linear interaction laws but also holds for non-linear interaction laws.

As a measure for the occurence of anomalous low energy dissipation, one can use the ratio σ between the time of free flight and the contact time t_c. The MD simulations underestimate the energy dissipation and lead to large fluctuations for $\sigma \ll 1$. On the other hand for $\sigma \gg 1$ no particular precautions are necessary and we find that the results of MD and ED simulations agree with each other. Note that ED simulations always behave like MD simulations with $\sigma \gg 1$. These computation-induced phenomena may be inhibited by using physically reasonable small values for the time t_c and nonlinear interactions.

Furthermore, we have achieved a direct dynamic assessment of model systems in 1D and in 2D. As stressed, in these systems a progressive transition takes place between a *condensed* phase, where the dilatation is close to zero and the beads' motion is collective, to a *fluidized* phase, where the beads' motion is erratic. We find in the fluidized regime that the height of the center of mass and hence the potential energy follows the scaling law

$$h_{cm} - h_{cm0} \approx \begin{cases} C_{1D}(A_0\omega)^2 \ X^{-1} \\ C_{2D}(A_0\omega)^{3/2} X^{-1}, \text{ for } \varepsilon_w < 1 \\ C_{2D}^*(A_0\omega)^2 \ X^{-1}, \text{ for } \varepsilon_w = 1 \text{ and } l/L \gg 1 \ , \end{cases} \tag{54}$$

where $C_{1D} = 4/(3g)$, $C_{2D} = 1/(5g)$ $m^{1/2}s^{-1/2}$ and $C_{2D}^* = 2/(5g)$. The parameters involved are A_0, ω, N and ε whereas the relevant parameters are only $A_0\omega$ and $X = (N/n_b) (1-\varepsilon)$. In particular, the velocity $A_0\omega$ controls the potential energy, whereas the effective dissipation parameter X is important for the shape of the density profile. The height of the center of mass $h_{cm}-h_{cm0}$ does not explicitly depend on the acceleration α, although the onset of fluidization does.

The main difference between one- and two-dimensional systems consists in the fact that in 2D systems with dissipative walls the power law of $A_0\omega$ is 3/2, whereas it is 2 in 1D. In a 2D situation where the collisions with the walls are elastic and the mean free path $l \gg L$ we found similar to the 1D case a power law of 2. The dependence on X is the same in 1D and in 2D. In 1D the exponent of X was found to be -1 for $X < 0.1$ (for $0.1 < X < 2.8$ a second order polynomial correction for the X-dependence was applied), while in 2D we find the exponent of X around -1 in the range $0.05 < X < 2$.

In 1D, we evaluated, as a function of the parameters ε and N, the acceleration, needed to reach the fluidized phase for all the beads. When $N \gg 1$ we showed that the acceleration scales with $X = N (1-\varepsilon)$. In particular, for very high accelerations α and for $X > X_c$ (say $X_c \approx 3.1$) we never found that the whole column fluidizes. Instead, for $2.5 < X < 4$ we find that the column separates into an array of condensed beads at the bottom and into several beads fluidized at the top. For very low accelerations we observe

that the column moves as a block, so that no fluidization occurs. For $X < X_c$ we found that a cluster separates due to a collision with the bottom plate, while for $X > X_c$ a clustered block stays clustered. Furthermore, we related the threshold value X_c to the findings of Bernu and Mazighi [31] who studied a column of beads hitting a wall without gravity; in our system with gravitation we found a variety of additional effects, since energy is steadily fed into the system.

At low accelerations the Fourier spectrum of the cm-motion shows subharmonic responses, which reproduce a Feigenbaum scenario, interrupted by series of fluidized and chaotic regimes. In this case, the column behaves for all practical purposes as a condensed block, with long phases of motion where all beads have almost the same velocity but are not necessarily in contact. An important point is that the acceleration which determines the onset of the transition regime may become extremely large in the case of low restitution coefficients and high number of beads.

The agreement between 1D experiments and numerical simulations is good. In experiments the numerically predicted fluidized regime at high restitution coefficients, for example steel beads, was observed. For small X we showed that the density profiles, found from numerical simulations scale with the experimental data. For large X ($X = 4$), for example aluminum beads, we observe a bifurcation scenario and find condensation as well as clusterization in ED simulations as well as in experiments. Our MD simulations did not lead to the clustered behavior of aluminum beads; we observed the detachment effect.

In addition, we have presented 2D situations encountered in MD simulations of rather densely packed grains. We have shown that taking realistic contact times t_c, while keeping the restitution coefficient ε constant, leads to quite small values for the convection strength J. On the other hand, when t_c becomes large convection rolls form readily. This is the domain of the detachment effect, where the interparticle distances fluctuate greatly; for due to the large friction of the particles with the boundaries convection is enhanced.

It is worth noticing that some of the features of the response of vibrated model systems in 1D reappear, at least qualitatively, in higher dimensions as well. A restriction on the simulations presented here is that they have been performed in 1D and in 2D. 3D-simulations are neccessary, since many phenomena found in granulates seem to stem from steric effects. The techniques we presented can, of course, also be applied in 3D. It is only the available computer time that at present limits our possibilities to perform simulations with 3D-systems of reasonably large sizes.

However, in 2D and 3D bifurcation scenarios are also observed [13,19,70]. Fluidization is evidenced in 2D and 3D experiments; there a fluidized regime at the surface may coexist with a condensed phase. Similarly to the 1D case, surface fluidization was

shown to be strongly dependent on the internal dissipation of the granular material [19].

Evidently, more work is neccessary in order to determine optimal parameters for MD simulations. For the study of effects like heaping, size segregation and convection one may have to include, in addition to reasonable contact times, static friction and rotation of the particles as well. For the microscopic interactions, aspects like memory, i.e. hysteresis, may be important [58,59]. The idea of pairwise interactions must be reconsidered in situations when, as a rule, a particle is in contact with several of its neighbors.

We close this study on a cautionary note about taking computer-generated patterns as a valid explanation for experimental findings: a careful comparison of the macroscopic outcome with experimental benchmarks, as well as an in-depth analysis of the parameters and models used for the simulations is always required.

Appendix A (LRV procedure in 1D)

Using the event-driven algorithm presented in subsection 2.2 we are able to simulate the fluidized regime very effectively because the computing time is proportional to the number of events, and not (like in MD simulations) to the number of time-steps. In the fluidized regime the times between collisions are large and beads move independently of each other. In the condensed regime the time intervals between collisions decrease (e.g. Fig.2) and several beads are close and move in a correlated way [compare Figs.13(b) and 13(c)]. In the following we describe a new algorithm which is able to get rid of collisions occurring at extremely short time intervals. This algorithm is similar in spirit to the procedure for individual beads but is also able to deal with clusters.

Formally, we introduce the concept of clusters as systems of beads in contact. We let two objects turn into a cluster if their relative velocities after an event lie below a certain value v_c; then we set their relative velocities to zero. As long as there is no cluster in the system, the normal event-driven procedure increases time with time steps Δt_i defined in Eq.(11). These time steps become very small for objects almost in contact (see Fig.2). Many processes then happen almost simultaneously. To speed up the algorithm we developed the **Largest Relative Velocity (LRV) procedure.** For this we compute all relative velocities $\Delta v_i = v_{i-1} - v_i$ between all pairs $(i, i\text{-}1)$ of clustered objects. Objects with $\Delta v_i \leq 0$ do not collide, whereas the objects with $\Delta v_i > 0$ are bound to interact.

The LRV procedure works as follows: we pick out the maximal value of the set (Δv_i), say $\Delta v_j = \max(\Delta v_i)$ and let the corresponding pair (say j, j-1) collide. The velocity changes are computed, using the same collision matrices as defined in Eqs.(12) and (13); then the set (Δv_i) of relative velocities is updated. The above procedure is repeated until all Δv_i of objects in a cluster are less than or equal to v_c (some Δv_i can, of course, become negative in which case some beads leave the cluster).

We will now discuss the special cases which involve collisions of clusters. On first glance we may differentiate whether the bottom plate is involved in the collision or not; this leads to three possible situations to be accounted for. If the bottom plate is not involved collisions occur between two clusters, say with N_1 and N_2 beads each. If the bottom plate is involved we have a cluster (N_1) colliding with the bottom plate, or a cluster (N_1) that collides with another cluster (N_2) which rests on the bottom plate. These situations include

as special cases the simple binary collisions of one bead with the bottom plate or with another bead (one bead is a special case for a cluster). These three distinct situations are dealt with on the same footing by the LRV procedure; they differ, however, physically, due to the very large mass (assumed infinite) of the bottom plate. We consider them one by one.

A.1.   Collisions of two clusters

In a collision involving two clusters of sizes N_1 and N_2, a total number of $M = N_1 + N_2$ objects are in contact which means in 1D a total of M-1 interacting pairs. To visualize this case we plot the trajectories of two columns of $N_1 = 2$ and $N_2 = 3$ beads each during a collision in Fig.44; the computation was performed with the restitution coefficient $\varepsilon = 0.8$.

Fig.44:

Trajectories of 5 beads, initially in two clusters, for $\varepsilon = 0.8$.
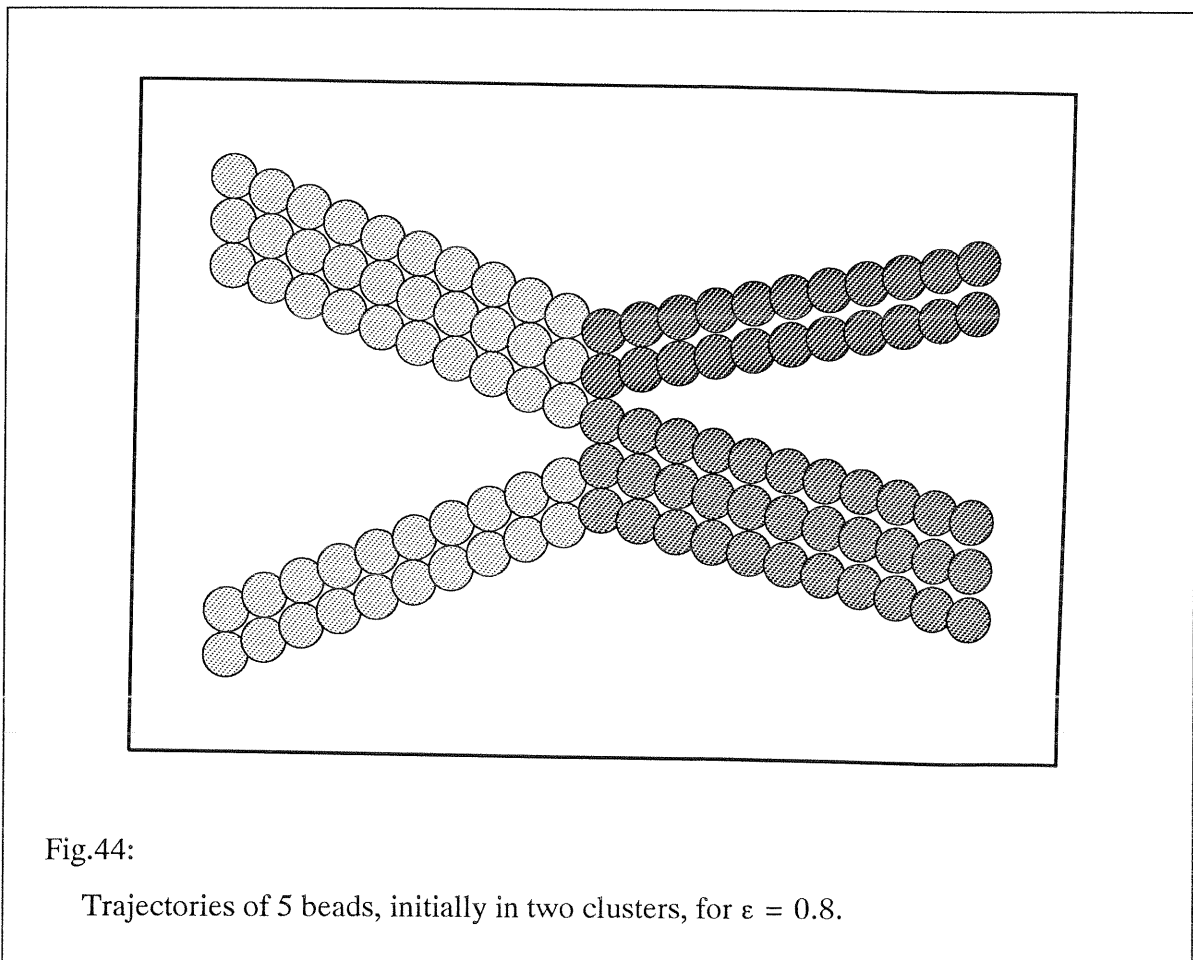
To test the outcome of the LRV procedure we look at what happens when the initial separation s_0 between the beads decreases towards zero. Thus we carry out a series of

simulations in which we vary s_0; we take it to be $s_0 = 10^{-3}$m, $s_0 = 10^{-4}$m, $s_0 = 10^{-5}$m, $s_0 = 10^{-6}$m and $s_0 = 0$ m. The simulations for $s_0 > 0$ are performed in the event-driven fashion, whereas for $s_0 = 0$ LRV is used. In all simulations the center of mass is a conserved quantity; for identical initial conditions (except s_0) the trajectories after the collisions coincide quantitatively for all $s_0 \leq 10^{-5}$m. Thus the LRV procedure reproduces the behavior of two colliding columns of beads very well when s_0 is small.

A.2. Collisions of one cluster with the bottom plate.

To illustrate this case we plot a cluster of beads ($N_1 = 5$) that hits the bottom plate in Fig.45; we take $\varepsilon = 0.9$ and $\varepsilon_p = 1.0$. This special case computed in the LRV formalism can be directly compared to the results of the independent collision wave (ICW) model introduced by Bernu and Mazighi [31]. The ICW formalism uses the transfer matrix $\mathbf{Y}$ for
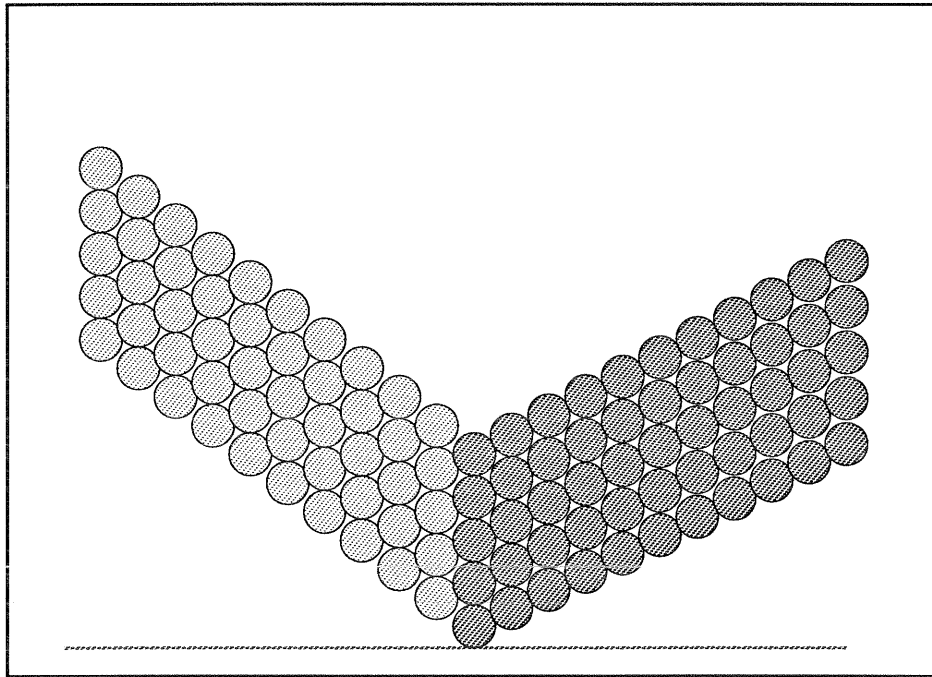
Fig.45:

Trajectories of 5 beads, initially in one cluster, which hits the bottom plate. The restitution coefficients are $\varepsilon = 0.9$ and $\varepsilon_p = 1$.

one collision wave such that $u_i = Y_{ij}v_j$, where u_i and v_j are the velocities of the particles before and after the collisions, respectively. $\mathbf{Y}$ is an ordered product of $(N+1)\times(N+1)$ matrices; say for one collision wave from below:

$$Y_n = D_{n-1,n}D_{n-2,n-1}\cdots D_{1,2}D_{0,1} \ .$$

(A1)

The $D_{i-1,i}$ are related to the $C_{i-1,i}$ of Eqs.(12) and (13); they have an almost diagonal form:

(A2)

$$
D_{i-1,i} = \begin{pmatrix}
1 & & & & & & \\
 & \ddots & & & & 0 & \\
 & & 1 & & & & \\
 & & & \boxed{C_{i-1,i}} & & & \\
 & & & & 1 & & \\
 & 0 & & & & \ddots & \\
 & & & & & & 1
\end{pmatrix}
\begin{array}{l} \\ \\ \\ \text{row } i\text{-}1 \\ \text{row } i \ . \\ \\ \\ \end{array}
$$

For small X, see Eq.(38), (say $\varepsilon = 0.9$ and $N = 5$) the collision waves do not interfere and we find that the ICW and the LRV models lead to exactly the same results. The difference in the velocity of the beads is smaller than $10^{-12}\,\text{ms}^{-1}$ after the collision. At these low X-values the order of collisions is indistinguishable in the two models. For large X, say $\varepsilon = 0.6$ and $N = 5$, the order of collisions in the two models does not coincide anymore, since different collision waves catch up with each other and interfere.

A.3. Collisions of a cluster resting on the plate with another cluster

As in A.1 and A.2 we carry out the sequence of collisions in the order specified by the LRV procedure when the clusters hit each other. As an example for this case we plot the situation when $N_1 = 3$ beads hit $N_2 = 2$ beads which rest on the bottom plate in Fig.46.
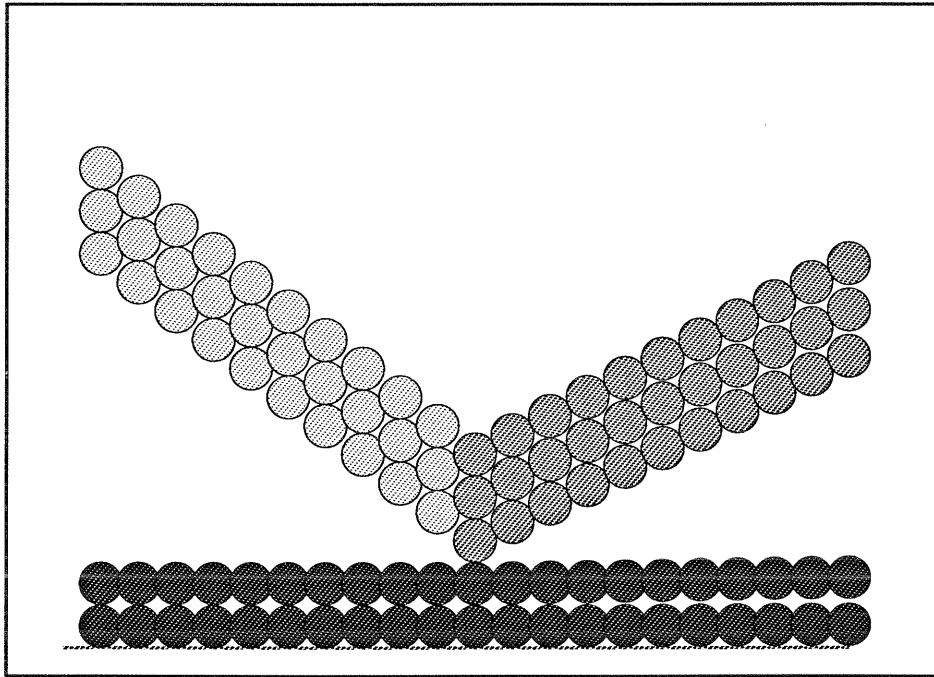
Fig.46:

Trajectories of 3 beads in a cluster which hits a cluster of 2 beads resting on the bottom plate. The restitution coefficients are $\varepsilon = 0.9$ and $\varepsilon_p = 1$.

A.4. A test for the cut-off velocity

When the relative-velocity of two objects drops below the cut-off velocity v_c we merge these objects into a cluster in the LRV-procedure. This leads to a transition from a condensed (but still separated) stack of objects to a cluster of objects in contact. In the stack the times between collisions do not vanish in general, whereas in the cluster the times

between collisions are zero. Thus we have to choose the arbitrary cut-off velocity v_c to be orders of magnitude lower than the typical velocity of the system, given by $A_0\omega$. In an independent series of simulations we have tested the dependence of the height of the center of mass h_{cm}, of the dissipation time τ_D and of the mean dilatation λ on the value of v_c We find that the choice of v_c does not influence these quantities, as long as $v_c \ll A_0\omega$. In Fig.47 we display the height of the center of mass h_{cm} (triangles), the dissipation time τ_D (circles) and the mean dilatation λ (squares) versus v_c of a system of $N = 10$ beads with $A_0\omega = 0.25$ ms^{-1}, $\varepsilon = 0.9$ and $\varepsilon_p = 1$. These values do not change as long as we choose v_c such that $v_c < 10^{-4}$ ms^{-1}; thus when computing h_{cm}, τ_D or λ taking v_c below 10^{-4} ms^{-1} leads to decreases in the computing time without effecting the outcome of the simulations.

Fig.47:

Results for h_{cm} (triangles), τ_D (circles) and λ (squares) obtained as a function of the cut-off velocity v_c. Here $N = 10$, $A_0\omega = 0.25$ms^{-1}, $\varepsilon = 0.9$ and $\varepsilon_p = 1$. Below 10^{-4}ms^{-1}, the data are independent of v_c.
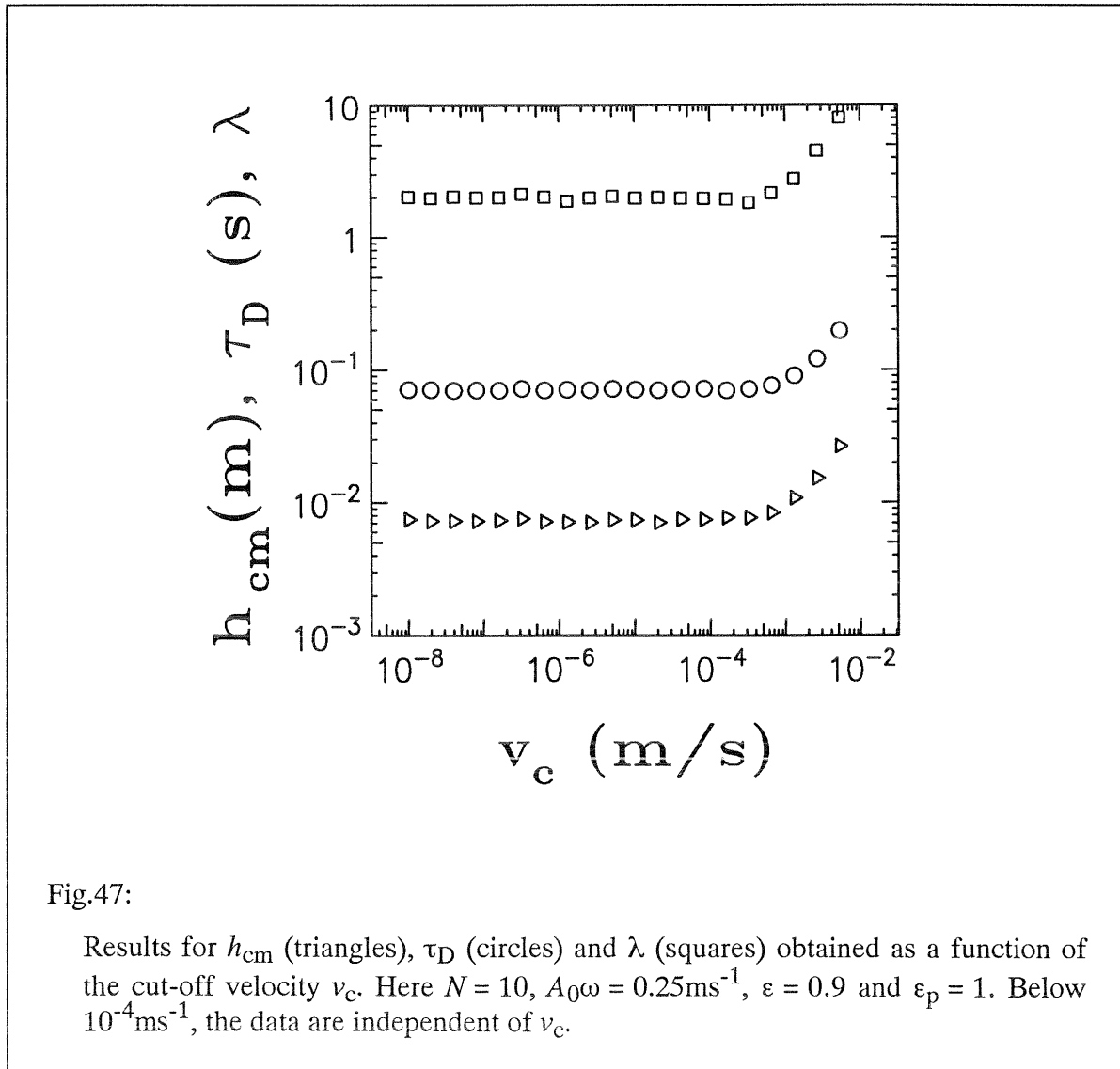
Appendix B (The predictor-corrector algorithm)

Here we focus on a numerical procedure [35] for the solution of the equations of motion for many particle systems. As usual in computer simulations one has given the position, the velocity and other dynamic information at a time t [here this information is component of a field $G(t)$] and wants to obtain the position, velocity etc. at a later time $t+\Delta t$ [i.e. one wants to obtain $G(t+\Delta t)$].

In this study Δt is equivalent to the time step of the molecular dynamics simulation, t_{MD}, and in fact limits the time-scale available in simulation. Assume a system with a vibrating container and steel spheres of diameter 2 mm, i.e. the system of Sec.5.2.; we simulated 200 periods, i.e. 10 seconds. The physically correct contact time for the spheres used is $t_c \cong 6\times10^{-6}$s, what corresponds to $t_{MD} \cong 10^{-6}$s. Thus we had to perform roughly 10^7 MD steps.

The predictor-corrector algorithm may be generalized, as follows:

(S1)	given is $G(t)$
(S2)	predict $G(t+\Delta t)$
(S3)	evaluate the forces (acceleration $a_i^P = f_i^P/m_i$) using the predicted $G(t+\Delta t)$
(S4)	correct $G(t+\Delta t)$ using the accelerations a_i^P
(S5)	calculate any values of interest and increase time: $t := t+\Delta t$
(S6)	return to step (1)

If the trajectory is continuous, an estimate of $G(t+\Delta t)$, i.e. step (S2), is a Taylor expansion about time t:

$$
\begin{aligned}
r^P(t + \Delta t) &= r(t) + \Delta t v(t) + \tfrac{1}{2}(\Delta t)^2 a(t) + \tfrac{1}{6}(\Delta t)^3 b(t) + \dots \\
v^P(t + \Delta t) &= v(t) + \Delta t a(t) + \tfrac{1}{2}(\Delta t)^2 b(t) + \dots \\
a^P(t + \Delta t) &= a(t) + \Delta t b(t) + \dots \\
b^P(t + \Delta t) &= b(t) + \dots
\end{aligned}
\tag{B1}
$$

and the superscript 'p' marks these values as 'predicted' values and r, v, a, and b stand for position, velocity, acceleration, and the third time-derivative of r respectively. Here we cut

the sequence after the third derivative; for the use in simulations we will cut after the fifth derivative. We found it convenient to use the Nordsieck-Gear predictor-corrector method, where the quantities g_i $(g_0(t) = r(t)$, $g_1(t) = \Delta t\, v(t)$, $g_2(t) = (1/2)(\Delta t)^2\, a(t)$, $g_3(t) = (1/6)(\Delta t)^3\, b(t)$, ...) are time-step scaled. Eq.(B1) now writes, up to fifth order as:

$$
\begin{pmatrix}
g_0^P(t+\Delta t) \\
g_1^P(t+\Delta t) \\
g_2^P(t+\Delta t) \\
g_3^P(t+\Delta t) \\
g_4^P(t+\Delta t) \\
g_5^P(t+\Delta t)
\end{pmatrix}
=
\begin{pmatrix}
1 & 1 & 1 & 1 & 1 & 1 \\
0 & 1 & 2 & 3 & 4 & 5 \\
0 & 0 & 1 & 3 & 6 & 10 \\
0 & 0 & 0 & 1 & 4 & 10 \\
0 & 0 & 0 & 0 & 1 & 5 \\
0 & 0 & 0 & 0 & 0 & 1
\end{pmatrix}
\begin{pmatrix}
g_0(t) \\
g_1(t) \\
g_2(t) \\
g_3(t) \\
g_4(t) \\
g_5(t)
\end{pmatrix}
,
\tag{B2}
$$

where the Matrix develops in a way similar to a Pascal triangle. Eq.(B2) will not generate correct trajectories, because we have not yet introduced the equations of motion.

The equations of motion will enter in step (S3), where we calculate the corrected accelerations $a^c(t+\Delta t)$ as functions of the predicted coordinates g^P. The corrected accelerations are then compared with the predicted accelerations, to estimate the error $\Delta a(t+\Delta t) = a^c(t+\Delta t) - a^P(t+\Delta t)$ at time $t+\Delta t$, made in the prediction step. This error together with the predicted values leads in step (S4) to the corrected values, and reads as:

$$
g_i^c(t+\Delta t) = g_i^P(t+\Delta t) + c_i \Delta a(t+\Delta t) \ ,
\tag{B3}
$$

where the index of g_i stands for the i-th, time step scaled, derivative of r and the c_i are in detail:

c_0	c_1	c_2	c_3	c_4	c_5
3/16	251/360	1	11/18	1/6	1/60

Note that the use of Eqs.(B2) and (B3) in the algorithm makes it neccessary to use, in addition to the time step scaled variables, time-step scaled parameters as well.

For the computation of average quantities like density or kinetic energy we sum the quantities observed at given times or phases in step (S5) and divide by the number of additions. In step (S6) we jump back to step (S1) until the maximum simulation time is exceeded.

Appendix C (Nonlinear interaction laws for MD)

In the following we consider nonlinear interactions between particles. Using Eq.(27) we present estimates for the contact time t_c, the maximal penetration x_{max} and the restitution coefficient ε.

The elastic energy is $E_{el} = Ed^{1-\beta} x_{max}^{2+\beta}/(2+\beta)$, as can be found by setting $\eta = 0$ in Eq.(27) and integrating it in standard fashion, after multiplication by $\dot{x}$. Suppose that the initial kinetic energy $E_k = mv_0^2/2$ is completely transferred to elastic energy. This leads to a maximal penetration depth of:

$$x_{max} = \left(1 + \frac{\beta}{2}\right)^{1/(2+\beta)} \left(\frac{m_{red}}{Ed^{1-\beta}}\right)^{1/(2+\beta)} (v_0)^{2/(2+\beta)} . \tag{C1}$$

Separating the energy conservation equation into t-dependent and x-dependent terms and integrating from $t = 0$ to $t_c/2$ or from $x = 0$ to x_{max} the contact time t_c follows:

$$t_c = I(\beta)\frac{x_{max}}{v_0} = I(\beta)\left(1 + \frac{\beta}{2}\right)^{1/(2+\beta)} \left(\frac{m_{red}}{Ed^{1-\beta}}\right)^{1/(2+\beta)} (v_0)^{-\beta/(2+\beta)} . \tag{C2}$$

In Eq.(C2) $I(\beta)$ is:

$$I(\beta) = \frac{\sqrt{\pi} \, \Gamma(\frac{1}{2+\beta})}{(1+\beta/2)\Gamma(\frac{4+\beta}{4+2\beta})} = \begin{cases} \pi & \text{for} \quad \beta = 0 \\ 2.94 & \text{for} \quad \beta = 1/2 \end{cases},$$

where $\Gamma(z)$ is the Gamma function. From Eq.(C2) one infers that the contact time follows $t_c \propto v_0^{-1/5}$ for the Hertz interaction law ($\beta = 1/2$). Eqs.(C1) and (C2) lead to the expressions of Ref.[73], valid for two spherical particles of diameter d and of the same material, when one sets $E = Y/(3(1 - \tilde{\sigma}^2))$; here Y is the Young modulus and $\tilde{\sigma}$ the Poisson ratio. Dealing with particles of different diameters requires the use of $(d_i + d_j)/(2d_id_j)$ instead of $1/d$. Using the MD formalism for binary collisions, we tested that x_{max} and t_c obey the above Eqs.(C1) and (C2) within 0.1 percent, as long as the dissipation is weak, i.e. $\varepsilon > 0.9$. One test consists of simulating the pair collisions of 200 particles, while varying the initial relative velocity v_0 of each pair. This leads to a set of data that agrees with Eqs.(C1) and (C2) over more than 15 orders of magnitude in v_0. Another test consists in solving Eq.(26) numerically (the

MAPLE V procedure for the solution is presented in Appendix D.2). The parameters used in the procedure are $\beta = 1/2$, $\gamma = 0$, $2\mu = 10\ \mathrm{s}^{-1}$ and $\omega_0^2 = 10^6\ \mathrm{s}^{-2}$. For initial velocities $v_0 = 1\ \mathrm{ms}^{-1}$, $0.1\ \mathrm{ms}^{-1}$, and $0.01\ \mathrm{ms}^{-1}$ we calculated from Eq.C2 the contact times $t_c \cong$ 0.0128 s, 0.0203 s, 0.0321 s respectively (note that these times are valid for no dissipation). The numerical solution leads to $t_c \cong 0.0129$ s, 0.0205 s, 0.0328 s and the restitution coefficients $\varepsilon \cong 0.932$, 0.894, and 0.834, respectively. In Fig.48 we plot x as a function of time for the different initial velocities. We find the maximum penetration decreasing with decreasing v_0, whereas the contact time increases with decreasing v_0. Here we used a non-linear model; in the case of a linear model, the contact time is velocity independent. We now plot in Fig.49 the first derivative of $x(t)$ scaled by v_0, i.e. v/v_0, as a function of time scaled by t_c, i.e. t/t_c. The functions v/v_0 do not scale for different initial velocities and lead to different values of v/v_0 for $t/t_c = 1$, i.e. different restitution coefficients ε.

As an example we give the contact times t_c for different diameters of the particles and for the initial relative velocity $v_0 = 1\ \mathrm{ms}^{-1}$, using Eq.(C2) with $\beta = 1/2$. For diameters $d = 1$ mm, 1.5 mm, 2 mm and 3 mm we found $t_c = 3\ \mu s$, 4.55 μs, 6.1 μs, and 9 μs, respectively; these values hold for steel or aluminum pair collisions within a deviation of few
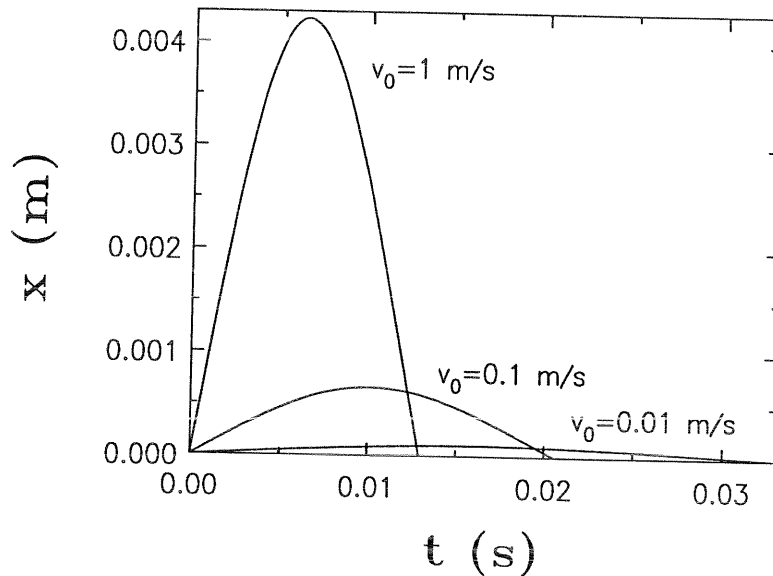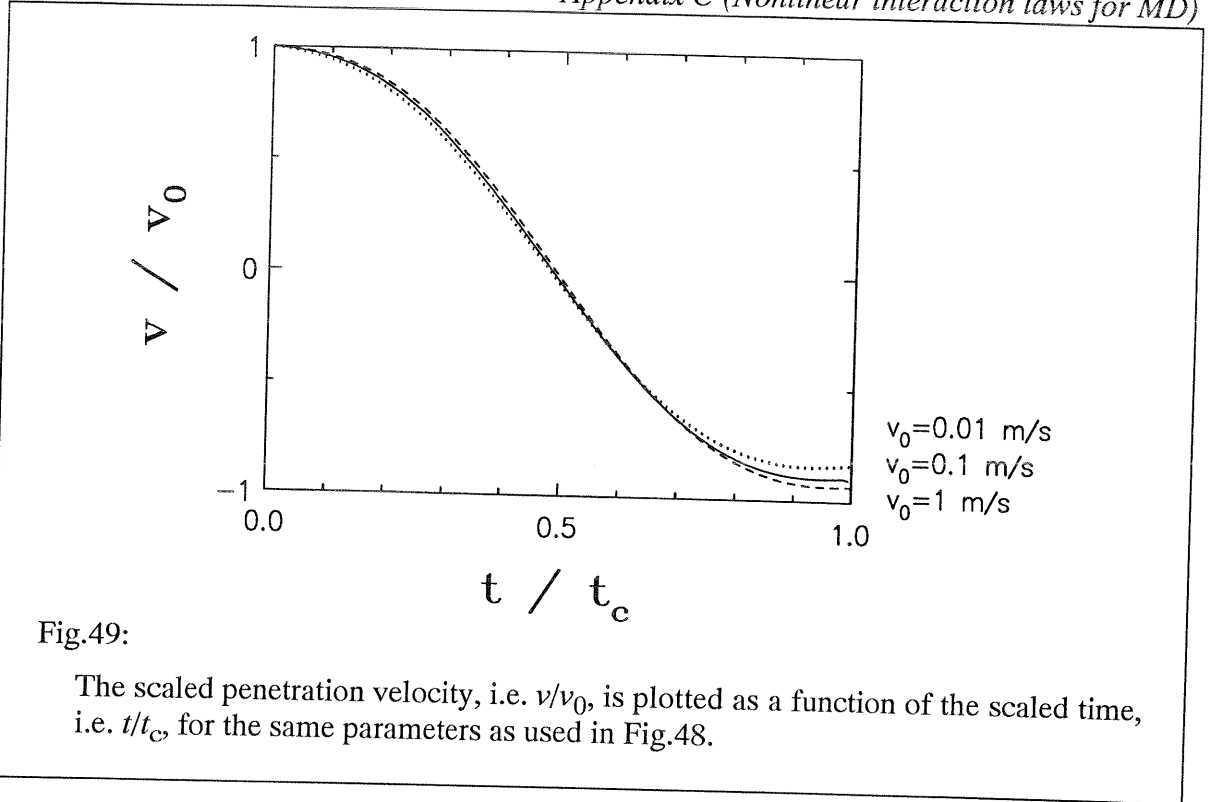

Fig.48:

The penetration depth x is plotted as a function of time for the collision of two spheres for different initial velocities. Here a nonlinear interaction law is used, i.e. $\beta = 1/2$, $\gamma = 0$, and the parameters in Eq.(26) are $\mu = 5\ \mathrm{s}^{-1}$ and $\omega_0 = 10^3\ \mathrm{s}^{-1}$.

Fig.49:

The scaled penetration velocity, i.e. v/v_0, is plotted as a function of the scaled time, i.e. t/t_c, for the same parameters as used in Fig.48.

percent.

Now we approximate the dissipated energy in the weakly dissipative regime through a product of the dissipative force F_{diss} and the distance x_{max}, on which this force acts:

$$E_{diss} \propto F_{diss} x_{max} \propto (\eta d^{1-\gamma} v_0) x_{max}^{1+\gamma}$$

which leads to:

$$E_{diss} \propto \eta \, d^{1-\gamma} \left(\frac{m_{red}}{Ed^{1-\beta}} \right)^{\frac{1+\gamma}{2+\beta}} v_0^{\frac{2+\gamma+\beta/2}{1+\beta/2}} \qquad (C3)$$

For a loss coefficient $1 - \varepsilon \propto 1 - \sqrt{1 - E_{diss}/E_0}$ we obtain:

$$1 - \varepsilon \propto v_0^{\frac{2\gamma - \beta}{2+\beta}} \qquad (C4)$$

For the Hertz-Kuwabara-Kono model ($\beta = \gamma = 1/2$), one finds a *slow* increase of $1-\varepsilon$ with the velocity i.e. $1 - \varepsilon \propto v_0^{1/5}$. Note the behavior in the case $\beta = 1/2$ and $\gamma = 0$ for it was considered in Refs.[50,53] one finds $1 - \varepsilon \propto v_0^{-1/5}$, i.e. beads are more elastic at higher velocities. We suggest that this might be one reason why no steady state for a system of particles on an inclined chute is found [50]. Due to gravity the particles are accelerated; if there is less dissipation at higher velocities ($\beta = 1/2$, $\gamma = 0$), there is no reason for a steady state to build up. On the other hand if the dissipation increases with the velocity ($\beta = 1/2$,

$\gamma = 1/2$) one has two effects which balance each other, i.e. at higher velocities more energy is dissipated. In Table C1 we summarize the findings and give the corresponding references, where the scaling laws were used.

β	γ	ν_1	ν_2	ν_3	Refs.
0	0	1	0	0	[46,45]
0	1/5	1	0	1/5	
1/2	0	4/5	-1/5	-1/5	[50,55,57]
1/2	1/2	4/5	-1/5	1/5	[83]
1/2	1/4	4/5	-1/5	0	[81]

Table C1:

The exponents ν_1, ν_2, and ν_3, which give the v_0 dependence of $x_{max} \propto v_0^{\nu_1}$, $t_c \propto v_0^{\nu_2}$, and $1 - \varepsilon \propto v_0^{\nu_3}$ in the limit of low dissipation (η small). The interaction law is Eq.(27) of the main text.

Note that the penetration depth and the contact time only depend on β, while the behavior of $1 - \varepsilon$ is influenced by changing the exponent γ. Most nonlinear MD simulations [50-55,57] were carried out using $\gamma = 0$; this means that $1 - \varepsilon$ is proportional to $v_0^{-1/5}$, i.e. at higher velocity one has less dissipation.

In Fig.50 we plot the contact time, see Eq.(C2), for two spheres made of the same material, with diameter 0.04 m as a function of the impact velocity; here we use $\beta = 1/2$. We measure the impact velocity in units of feet per second to get a figure, comparable to Fig.169 in Ref.[74]. For a fixed impact velocity the contact time for steel, aluminum and glass is comparatively small, while the contact time increases when using beads made of brass, silver, plexiglass, and lead.

110
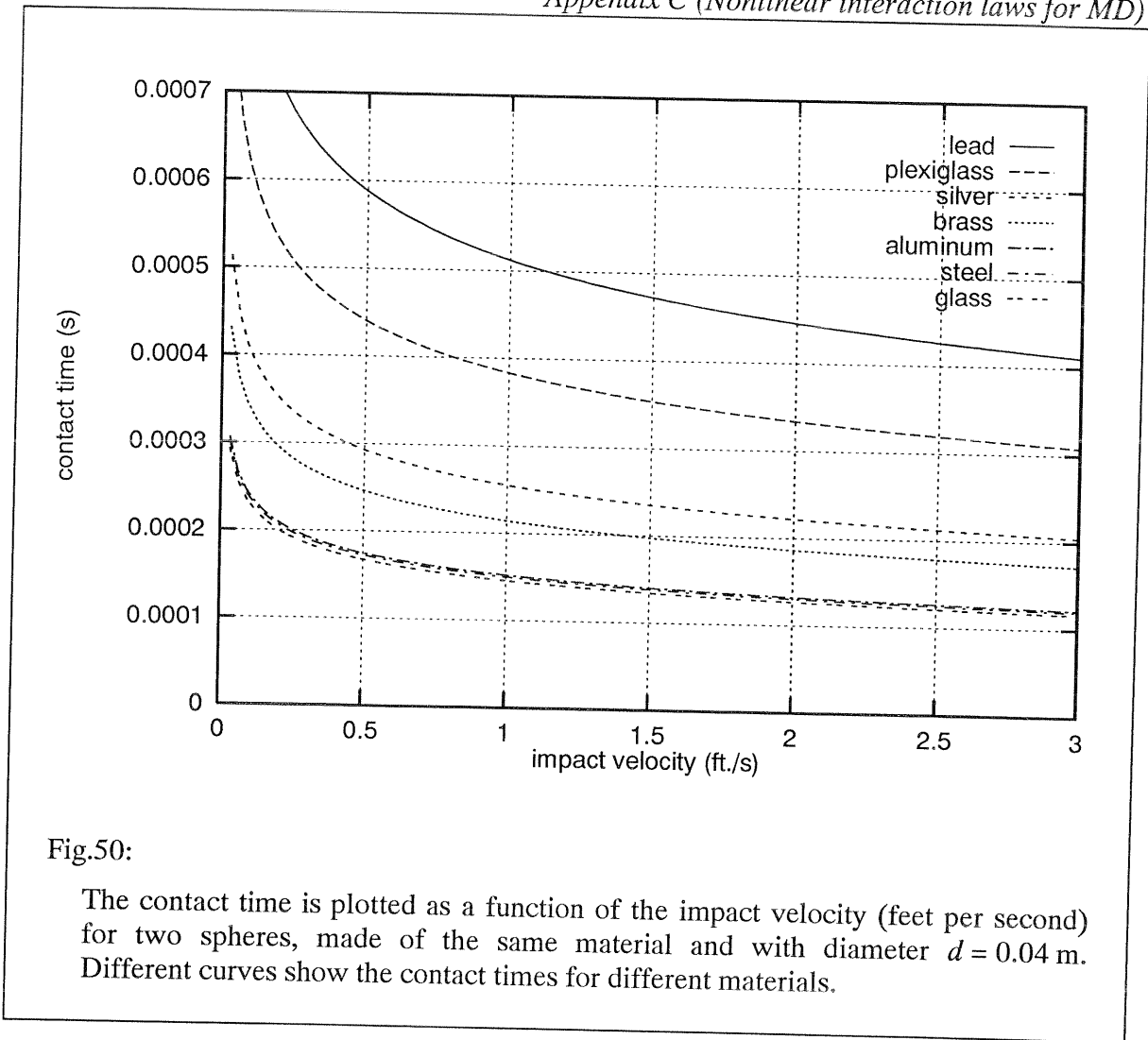
Fig.50:

The contact time is plotted as a function of the impact velocity (feet per second) for two spheres, made of the same material and with diameter $d = 0.04$ m. Different curves show the contact times for different materials.

We give parameters used for MD simulations with nonlinear interaction laws: For $v_0 = 0.66$ ms^{-1} and $\beta = 1/2$, $\gamma = 0$, $K/m_{red} = 6.6\times10^{13}$ s^{-2}m$^{-1/2}$ and $D_n = 4\times10^4$ s^{-1} as well as for $\beta = \gamma = 1/2$, $K/m_{red} = 6.6\times10^{13}$ s^{-2}m$^{-1/2}$ and $D_n = 2.5\times10^6$ s^{-1} we found the same values for $t_c \cong 10^{-5}$ s and $\varepsilon \cong 0.6$.

111

Appendix D (MAPLE V scripts)

D.1. Numerical Root-finding

We present the source script of Maple V commands, which we used to calculate the data for Figs.12 and 32. Comments are written to the right of a '#'-character.

```
                                          # MAPLE V script
                                          # Stefan Luding 1993
                                          # calculates the phase at which
                                          # a particle hits the
                                          # bottom plate
                                          # as a function of the
                                          # amplitude a


readlib(write);
open(xt05);                               # create an output-file
close();
interface(echo=0);


for alpha from 1 by .1 to 10 do           # scan a between 1 and 10
    for xdelta from alpha/4+1.5 by .5 to alpha/4+1.5 do
                                          # a first attemt for the root
                                          # scan the range of phase

        phi1:=arcsin(1/alpha);           # define φ1
        delta:=xdelta*2*Pi;              # step size
        gx2:=x+delta;                    # start-value
        gx1:=x+delta-phi1;               # start-value relative to φ1


    f(x,alpha):=sin(gx2)-1/alpha*(1+sqrt(alpha*alpha-1)*gx1-gx1*gx1/2);
                                          # define Eq.(30) relative to φ1


    F(alpha):=RootOf(f(x,alpha),x);      # find the solution of Eq.(30)
```

```
aOw:=alpha*9.81/2/Pi/20          # calculate A₀ω = αg/(2πf)
phi2:=evalf(F(alpha)+delta);     # calculate φ2

vc0:=cos(phi2)-cos(phi1)+(phi2-phi1)/alpha;
                                 # calculate the scaled
                                 # collision velocity

appendto(xt05);                  # write the results
writeln(alpha,evalf(delta/2/Pi,5),evalf(phi1/2/Pi,5),
        evalf(phi2/2/Pi,5),evalf(sin(phi2),5),evalf(vc0,5),
        evalf((aOw*(cos(phi2)+0.89*vc0),5),
        evalf(0.056*(0.89*aOw*vc0)^2,5));
```

output of: dimensionless acceleration α,

                dummy variable,

                normalized phase of take off p_1,

                normalized phase of next contact p_2,

                dimensionless position of the bottom plate at phase φ_2: $\sin(\varphi_2)$,

                scaled collision velocity $v_c/A_0\omega$,

                kinetic energy $2E_{kin}/(Nm)$ for $N=10$ and $\varepsilon=0.9$,

                ratio of relative energy and kinetic energy $2E_{rel}/(Nm)$ for $N=10$ and $\varepsilon=0.9$.

```
writeto(terminal);               # switch to terminal output




    od;
od;                              # end of loops


close();                         # end of output
quit();                          # end of script
```

D.2. Numerical Solution of Differential Equations

We present the source script of Maple V commands, which we used to calculate the data plotted in Fig.48 and 49. Comments are written to the right of a '#'-character.

```
                                        # MAPLE V script
                                        # Stefan Luding 1993
                                        # for the numerical
                                        # solution of Eq.(27)


del:=diff(x(t),t$2)+d*diff(x(t),t)+k*x(t)^(3/2);
                                        # define the differential equation

x0:=dsolve( { del, x(0)=0, D(x)(0)=v_0 }, x(t), numeric );
                                        # solve the equation numerically

d:=10;                                  # define dissipation
k:=1000000;                             # define elasticity


readlib(write);


v_0:=1;                                 # define initial velocity 1 ms^-1
open(yt00);                             # create output-file 'yt00'
for tt from 0 by 0.0002 to 0.035 do     # loop
     x0(tt) od;                         # write time and position
close();                                # close file 'yt00'


v_0:=0.1;                               # define initial velocity 0.1 ms^-1
open(yt01);                             # create output-file 'yt01'
for tt from 0 by 0.0002 to 0.035 do     # loop
     x0(tt) od;                         # write time and position
close();                                # close file 'yt01'


v_0:=0.01;                              # define initial velocity 0.01 ms^-1
open(yt02);                             # create output-file 'yt02'
for tt from 0 by 0.0002 to 0.035 do     # loop
     x0(tt) od;                         # write time and position
close();                                # close file 'yt02'


quit();                                 # end of script
```

Appendix E (ICW-Model)

In a recent article Bernu and Mazighi [31] investigated the problem of a column of N beads hitting a wall which moves at a constant velocity (in Ref.[31] no gravity was involved). One of the findings of Ref.[31] was that below a critical value of the restitution coefficient ε_c the beads cluster on the wall. Now ε_c was found to be independent of the initial state of agitation of the beads, but to be a function of the number N of beads [31]:

$$\varepsilon_c = \tan^2\left[\frac{\pi}{4}(1 - \frac{1}{N})\right] \tag{55}$$

At the limit $N \gg 1$ this leads to $\varepsilon_c \cong 1 - \pi/N$ or to:

$$X'_c = \pi \tag{56}$$

where $X'_c = N(1-\varepsilon_c)$ is the value above which clusterization of the column of beads occurs. Physically it corresponds to the possibility for a column of beads to cluster on a moving plate independently of the initial velocities inside the column. From our simulations we found that in the fluidized phase the relevant parameters (i. e. height of the center of mass and dissipation time) scale with $X = N(1 - \varepsilon)$ for $N \gg 1$. The behavior of, for example, the height of the cm can be fitted with a parabola in the interval from 0 to 2.8, see Eq.(40). This fit leads to an extrapolated value $X_c \cong 3.1$ for the intercept with the x-axis. Since our simulations are dynamic and energy is steadily fed into the system we cannot expect h_{cm} to vanish. Indeed, for $X > 2.8$ we find deviations from the simple pattern, a fact which indicates a more complex behavior of the column.

References:

[1]   *Disorder and Granular Media*, D. Bideau and A. Hansen eds., Elsevier Sci. Publ., Amsterdam (1993).

[2]   H. M. Jaeger, S. R. Nagel, Science **255**, 1523 (1992).

[3]   H. M. Jaeger, J. B. Knight, C.-h. Liu, S. R. Nagel, MRS Bulletin, Vol. XIX, No.5, 25 (1994).

[4]   A. Rosato, K. J. Strandburg, F. Prinz and R. H. Swendsen Phys.Rev.Lett. **58**, 1038 (1987).

[5]   P. Devillard, J. Physique **51**, 369 (1990).

[6]   R. Jullien, P. Meakin and A. Pavlovitch, Phys. Rev. Lett. **69**, 640 (1992).

[7]   G. Baumann, E. Jobs and D. E. Wolf, in proceedings of the conference *Fractals in Natural Sciences*, eds. M. Matsushita, M. Shlesinger, and T. Vicsek, World Scientific, Singapore (1993).

[8]   P. K. Haff and B. T. Werner, Powder Techn. **48**, 239 (1986).

[9]   J. Duran, J. Rajchenbach, E. Clément, Phys. Rev. Lett. **70**, 2431 (1993).

[10]   C. Laroche, S. Douady and S. Fauve, J. de Physique **50**, 699 (1989).

[11]   J. Walker, Sci. Am. **247**, 167 (1982); F. Dinkelacker, A. Hübler and E. Lüscher, Biol. Cybern. **56**, 51 (1987).

[12]   P. Evesque, J. Rajchenbach, Phys. Rev. Lett. **62**, 44 (1989).

[13]   E. Clément, J. Duran, J. Rajchenbach, Phys. Rev. Lett. **69**, 1189 (1992).

[14]   A. Suzuki, H. Takahashi, and T. Tanaka, Powder Technology **2**, 72 (1968).

[15]   C. Brennen, S. Gosh and Wassgren, in "*Powders and Grains 93*" page 247, ed. C. Thornton, Balkema (Rotterdam, 1993).

[16]   M. Faraday, Phil. Trans. R. Soc. London **52**, 299 (1831).

[17]   S. Savage, J. Fluid. Mech. **194**, 457 (1988).

[18]   S. Douady, S. Fauve, C. Laroche, Europhys. Lett. **8**, 621 (1989).

[19]   E. Clément, J. Rajchenbach, Europhys. Lett. **16**, 149 (1991).

[20]   H. K. Pak and P. P. Behringer, Phys. Rev. Lett. **71**, 1832 (1993).

[21]   F. Melo, P. Umbanhowar, and H. L. Swinney, Phys. Rev. Lett. **72**, 172 (1994).

[22]   C-h. Liu and S. R. Nagel, Phys. Rev. Lett. **68**, 2301 (1992).

[23]   M. Leibig, Phys. Rev. E, **49**, 1647 (1994).

[24]   G. W. Baxter, R. P. Behringer, T. Fagert and G. A. Johnson, Phys. Rev. Lett.**62**, 2825 (1989); G. W. Baxter and R. P. Behringer, Phys. Rev. A **42**, 1017 (1990), Physica D **51**, 465 (1991).

[25]   P. C. Johnson, R. Jackson, J. Fluid. Mech. **176**, 67 (1987).

[26]   J. Duran, T. Mazozi, E. Clément, J. Rajchenbach, Phys. Rev. E **50**, 3092 (1994).

[27]   P. A. Thompson, G. S. Grest, Phys. Rev. Lett. **67**, 1751 (1990).

[28]   P. A. Cundall and O. D. L. Strack, Geotechnique **29**, 47 (1979).

[29]   J. J. Moreau, *in Nonsmooth Mechanics and Applications*, ed. J. J. Moreau and P. D. Panagiotopoulos (Springer-Verlag, Wien, New York, 1988) pp 1-82.

[30]   B. D. Lubachevsky, J. of Comp. Phys. **94**, 255 (1991).

[31]   B. Bernu and R. Mazighi, J. Phys. A **23**, 5745 (1990).

[32]   S. McNamara, W. R. Young, Phys. Fluids A **4**, 496 (1992).

[33]   S. McNamara, W. R. Young, Phys. Fluids A **5**, 34 (1993).

[34]   T. A. J. Duke, G. C. Barker, A. Mehta, Europhys. Lett. **13**, 19 (1990); A. Mehta and G. C. Barker, Phys. Rev. Lett. **67**, 394 (1991); A. Mehta, Physica A **186**, 121 (1992).

[35]   M. P. Allen and D. J. Tildesley, *Computer Simulation of Liquids* (Oxford University Press, Oxford, 1987).

[36]   E. Clément, S. Luding, A. Blumen, J. Rajchenbach and J. Duran, Internat. J. Mod. Phys B, **7**, 1807 (1993).

[37]   S. F. Foerster, M. Y. Louge, H. Chang, and K. Allia, Phys. Fluids **6**, 1108 (1994).

[38]   R. A. Bagnold, Proc. Roy. Soc. London **225**, 49 (1954).

[39]   S. B. Savage, J. Fluid Mech. **92**, 53 (1979).

[40]   P. K. Haff, J. Fluid Mech. **134**, 401 (1983).

[41]   M. Richman and R. Martin, preprint (1993).

[42]   S. B. Savage, in *Disorder and Granular Media*, ed.: D. Bideau, North Holland, Amsterdam (1993).

[43]   I. Goldhirsch, G. Zanetti, Phys. Rev. Lett. **70**, 1619 (1993).

[44]   S. Dippel, Diplomarbeit (1994).

[45]   J. A. C. Gallas, H. J. Herrmann, S. Sokolowski, Phys. Rev. Lett. **69**, 1371 (1992).

[46]   Yi Zhang and C. S. Campbell, J. Fluid Mech. **237**, 541 (1992).

[47]   D. C. Hong, J. A. McLennan, Physica A **187**, 159 (1992).

[48]   Y-h. Taguchi, Phys. Rev. Lett. **69**, 1367 (1992).

[49]   R. Mazighi, B. Bernu, F. Deylon, Phys. Rev. E **50**, 4551 (1994).

[50]   T. Pöschel, J. Phys. II **3**, 27 (1993)..

[51]   T. Pöschel and V. Buchholtz, Phys. Rev. Lett. **71**, 3963 (1993).

[52]   G. H. Ristow, J. Phys. I France **2**, 649 (1992).

[53] G. H. Ristow, Int. J. of Mod. Phys. C **3**,1281 (1993).

[54] F.-X. Riguidel, R. Jullien, A. Hansen and D. Bideau, J. Phys. I France **4**, 261 (1994); G. H. Ristow, F.-X. Riguidel and D. Bideau, J. Phys. I France, preprint (1994).

[55] Y. Lee, H. J. Herrmann, J. Phys. A: Math. Gen., **26**, 373 (1993).

[56] Y. Lee, J. Phys. I France **3**, 2017 (1993).

[57] Y. Lee, J. Phys. A **27**, L257 (1994).

[58] M. H. Sadd, Q. Tai, A. Shukla, Int. Journal of Non-Linear Mechanics, **28**, 251 (1993); C. Y. Zhu, A. Shukla, M. H. Sadd, J. of Appl. Mech. **58**, 341 (1991).

[59] O. R. Walton, Acta Mechanica **63**, 947 (1986).

[60] O. R. Walton, R. L. Braun, J. Rheology **30**, 949 (1986).

[61] M. Jean and J. J. Moreau, in *Proceedings of Contact Mechanics International Symposium*, Lausanne Switzerland, Oct. (1992).

[62] S. Luding, E. Clément, A. Blumen, J. Rajchenbach and J. Duran, Phys Rev E **49**, 1634 (1994).

[63] S. Luding, E. Clément, A. Blumen, J. Rajchenbach and J. Duran, Phys. Rev. E **50**, 4113 (1994).

[64] S. Luding, H. J. Herrmann, A. Blumen, Phys. Rev. E **50**, 3100 (1994).

[65] S. Luding, E. Clément, A. Blumen, J. Rajchenbach and J. Duran, Phys. Rev. E **50**, R1762 (1994).

[66] P. Evesque, E. Szmatula and J.-P. Denis, Europhys. Lett. **12**, 623 (1990); O. Zik and Stavans, Europhys. Lett. **16**, 255 (1991); O. Zik, J. Stavans and Y. Rabin, Europhys. Lett. **17**, 315 (1992).

[67] J. B. Knight, H. M. Jaeger, S. R. Nagel, Phys. Rev. Lett. **70**, 3728 (1993).

[68] S. Celashi, R. L. Zimmermann, Phys. Lett. A **120**, 447 (1987).

[69] P. Pieranski, J. Physique **44**, 573 (1983); P. Pieranski, Phys. Rev. A **37**, 1782 (1988).

[70] A. Mehta and J. M. Luck, Phys. Rev. Lett. **65**, 393 (1990).

[71] J. A. C. Gallas, H. J. Herrmann, S. Sokolowski, Physica A **189**, 437 (1992).

[72] A. Rosato and Y. Lan, in *Powders and Grains 93* page 241, ed. C. Thornton, Balkema (Rotterdam, 1993).

[73] L. D. Landau, E. M. Lifschitz *Band VII Elastizitätstheorie* Berlin (1989).

[74] W. Goldsmith, *IMPACT The theory and physical behaviour of colliding solids*, Edward Arnold (Publishers), London, (1964).

[75] See textbooks on numerical mathematics for details.

[76] H. J. Herrmann, J. Phys. II France **3**, 427 (1993).

[77] S. F. Edwards, R. B. S. Oakeshott, Physica A **157**, 1080 (1989).

[78] C. K. K. Lun, S. B. Savage, D. J. Jeffrey and N. Chepurny, J. Fluid. Mech. **140**, 223

(1983).

[79] J. M. Luck and A. Mehta, Phys. Rev. E **48**, 3988 (1993).

[80] R. L. Brown and J. C. Richard, "*Principle of Powder Mechanics*" (Pergamon Press, Oxford, 1966).

[81] Y-h. Taguchi, J. Phys. II France **2**, 2103 (1992).

[82] Y-h. Taguchi, Int. J. of Mod. Phys. B **7**, 1839 (1993).

[83] G. Kuwabara and K. Kono, Jap. J. of Appl. Phys. **26**, 1230 (1987).

[84] J. Reed, J. Phys. D: Appl. Phys. **18**, 2329 (1985).

[85] J. J. Moreau, private communication.

[86] S. B. Savage, Adv. Appl. Mech., **24**, 289 (1984); C.S. Campbell, Annu. Rev. Fluid Mech. **22**, 57 (1990).

[87] G. M. Homsy, R. Jackson and J. R. Grace, J. Fluid Mech. **236**, 477 (1992).

[88] S. B. Savage and K. Hutter, J. Fluid Mech. **199**, 177 (1989).

[89] J. T. Jenkins and M. W. Richman, Arch. Rat. Mech. **87**, 355 (1985).

[90] H. Caram and D.C. Hong, Phys. Rev. Lett. **67**, 828 (1991).

[91] Y.-h. Taguchi, private communication, (1993). The y-axis of Fig.4 in Ref.[48] has to be scaled.

Acknowledgements:

123

Own publications:

1. Stefan Luding, Diplomarbeit "Modelle für Reaktionen in eingeschränkten Medien", Bayreuth (1990).

2. H.Schnörer, S.Luding, A.Blumen, "Reactions on Fractals: The Case of Immobile Reactants" in: Fractals in the Fundamental and Applied Sciences, J. Henriques ed., Fundacao Calouste Gulbenkian, Lisbon (1990).

3. S.Luding, H.Schnörer, V.Kuzovkov, A.Blumen, "Bimolecular Annihilation Reactions: Immobile Reactants and Multipolar Interactions", J. Stat. Phys. **65**, 1261 (1991).

4. A.Blumen, S.Luding, I.M.Sokolov, "Fluctuation-Dominated Kinetics in the A+B→0 Reaction between Immobile Particles", J. Stat. Phys. **65**, 849 (1991).

5. E. Clément, S. Luding, A. Blumen, J. Rajchenbach, J. Duran, Int J. of Mod. Phys. B **7**, 1807 (1993)

6. S. Luding, E. Clément, A. Blumen, J. Rajchenbach, J. Duran, "Studies of Columns of Beads under External Vibrations", Phys. Rev. E **49**, 1634, (1994).

7. S. Luding, E. Clément, A. Blumen, J. Rajchenbach, J. Duran, "Anomalous energy dissipation in vibrated granular media: the detachment effect", submitted to Phys. Rev. E (1994).

8. S. Luding, H. J. Herrmann, A. Blumen, "Scaling behavior of 2-dimensional arrays of beads under external vibrations", submitted to Phys. Rev. E (1994).

9. S. Luding, E. Clément, A. Blumen, J. Rajchenbach, J. Duran, "The onset of convection in molecular dynamics simulations of grains", submitted to Phys. Rev. E, Rapid Communication (1994).

Lebenslauf

Name:	Stefan Luding
	geboren am 16. August 1964 in Selbitz
Staatsang.:	deutsch
Familienstand:	ledig

Anschrift:	Mühlenweg 1
	79283 Bollschweil
Telefon:	07633 / 500315
Fax:	07633 / 500215

1970	Grundschule in Selbitz
1974	Gymnasium in Naila
1984	Grundwehrdienst
1985	Studium der Physik mit Nebenfach Informatik an der Universität Bayreuth
1989	Diplomarbeit: 'Modelle zur Reaktion in eingeschränkten Medien'
1990	Abschluß des Studiums und Beginn des Promotionsstudiums
	über Reaktionskinetik und Simulation von Vielteilchensystemen
1991	Änderung des Promotionsthemas:
	Untersuchung der Physik granularer Materialien und
	Wechsel des Promotionsstudienorts nach Freiburg i. Br.

Fremdsprachen:	englisch, französisch
DV-Kenntnisse:	UNIX (IRIS,IBM/RS6000 und CRAY-YMP), AIX (RS/6000),
	DOS und MS-Windows für Workgroups (PC), VMS (VAX),
	FORTRAN, C, C++, dBase, Clipper und SQL-Datenbanken,
	TeX, GL-Grafik, PostScript, MAPLE und MATHEMATICA,
	WordPerfect 5.1, Word für Windows 2.0,
	diverse Grafik- und Präsentationsprogramme.
	Planung, Einkauf und Systemadministration
	eines heterogenen TCP/IP-LAN's bestehend aus:
	drei IBM/RS6000-Workstations (32H) unter AIX und
	12 PC's unter DOS bzw. Windows für Workgroups
	und NCSA Telnet.

Nebentätigkeit:	1986-88: Programmierer im RZ der Uni Bayreuth.
	1988: 2 Monate Werksstudent bei SIEMENS München
	(Forschung & Entwicklung - Simulation von Hochfrequenzfiltern).
	1988-90: Entwicklung eines Fakturierungsprogramms in dBFast,
	1990-93: Design einer Hotelverwaltung in Clipper 5.1,
	1991-94: Systemverwaltung in der Arbeitsgruppe in Freiburg.

Sonstiges:	1987-94: Lehrtätigkeit während des Semesters.
	div. Kongressaufenthalte in Deutschland, Frankreich und USA.
	insgesamt ca. 7 Wochen Forschungsaufenthalt in Paris im
	Rahmen einer internationalen Zusammenarbeit.

Hobbies:	Lesen, Radfahren, Tanzen (Standard und American Square Dance).